MULTIPLE INPUT MULTIPLE OUTPUT (MIMO) RADAR DETECTION OF MOVING TARGETS ON THE OCEAN SURFACE

RADAR MIMO POUR LA DÉTECTION DE CIBLES EN MOUVEMENT À LA SURFACE DE L'OCÉAN

A Thesis Submitted to the Division of Graduate Studies of the Royal
Military College of Canada
by

Jonathan Bathurst, BSc, RMC
Lieutenant-Commander

In Partial Fulfillment of the Requirements for the Degree of Master of
Applied Science in Electrical Engineering

April 2017

Acknowledgements

This thesis would not be possible without the guidance and motivational support provided by my thesis supervisors: Dr. Mostafa Hefnawi, Dr. Joey Bray, and Dr. Yahia Antar. Their background and expertise across a large subject area made this research feasible. Special thanks to Dr. Peter Moo and Dr. Jack Ding from Defence Research and Development Canada, Ottawa who provided some much-needed initial guidance and direction to conduct this research. Additional thanks to Michael McLernon and Ying-On Yan from Mathworks who provided technical support and troubleshooting assistance while exploring options for an experimental MIMO radar platform. Lastly, my sincere appreciation to Director Naval Combat Systems 5, whose generous sponsorship made this thesis possible.

Abstract

A navy ship must be able to accurately detect closely spaced surface targets in a cluttered environment for collision avoidance as well as to combat threats such as fast attack craft or submarine periscopes. Detecting surface targets becomes increasingly difficult when there are multiple threats inbound from different bearings or when a higher sea state is present. Current technology used in many navies around the world for surface target detection is an active phased array radar or a navigation radar. MIMO radar differs from current technology by using orthogonal waveforms on transmission which allows it to form a virtual array and conduct beamforming on reception. These differences introduce many advantages, but also some critical design considerations.

This thesis evaluates the performance of a naval radar in a cluttered environment using both a conventional phased array radar and a MIMO radar. A Simulink-based simulation model as well as a prototype MIMO radar system were designed and developed to measure returns from surface targets. Using these models, MIMO beamforming theory is validated and compared with a phased array radar. The effects of Doppler induced by moving targets on a MIMO radar over a longer coherent processing interval is also examined, highlighting the importance of selecting the operating frequency of the radar and the necessary design considerations that must be considered for detecting a target with radial velocity. A MIMO radar can search an entire area in only a few simultaneous orthogonal pulses and can provide the same or better level of accuracy than a phased array radar while providing a greater refresh rate. The experimental and simulation results show that a MIMO radar can augment or replace a phased array radar in detecting surface targets on the ocean.

Résumé

Un navire de la marine doit être en mesure de détecter avec précision des cibles de surface rapprochées dans un environnement encombré pour éviter les collisions et lutter contre les menaces telles que les engins d'attaque rapide ou les périscopes sous-marins. La détection des cibles de surface devient plus difficile quand il y a plusieurs menaces entrantes provenant de différents paliers ou quand la mer est trop agitée. La technologie actuelle utilisée dans de nombreuses marines au monde pour la détection de cibles de surface est le radar à balayage électronique actif ou le radar de navigation à rotation mécanique. Le radar MIMO diffère de la technologie actuelle en utilisant des formes d'ondes orthogonales en transmission qui lui permettent de former un réseau virtuel à formation de faisceaux en réception. Ces différences présentent de nombreux avantages, mais aussi des considérations de conception critiques.

Cette thèse permet d’évaluer les performances d'un radar naval dans un environnement encombré à l'aide à la fois d'un radar conventionnel à balayage électronique et d'un radar MIMO. Un modèle de simulation basé sur le logiciel Simulink ainsi qu’un bon d’essai expérimental ont été conçus et développés pour acquérir des cibles de surface marine. En utilisant ces modèles, la théorie de la formation de faisceau MIMO est validée et comparée à un radar à balayage électronique. La détection d’une cible mobile et l’effet Doppler qui en résulte sont également examinés, soulignant l'importance de sélectionner la fréquence de fonctionnement du radar et les considérations de conception nécessaires pour détecter une cible à vitesse radiale. Un radar MIMO peut rechercher une zone entière en transmettant seulement quelques impulsions orthogonales simultanées et peut fournir un niveau de précision et taux de rafraîchissement meilleur qu'un radar à balayage électronique. Les résultats expérimentaux et de simulation montrent qu'un radar MIMO peut augmenter ou remplacer un radar à balayage électronique pour détecter des cibles de surface sur l'océan.

Contents

List of Figures

List of Tables

List of Acronyms

ADC	Analog to Digital Conversion
ADS	Advanced Design System
CFAR	Constant False Alarm Rate
CPI	Coherent Processing Interval
CRB	Cramer-Rao Bound
DAC	Digital to Analog Conversion
DBF	Digital Beamforming
DC	Direct Current
DFT	Discrete Fourier Transform
DOA	Direction of Arrival
EPM	Electronic Protective Measures
ESPRIT	Estimation of Signal Parameters via Rotational Invariance
FIR	Finite Impulse Response
FPGA	Field-Programmable Gate Array
GLRT	Generalized Likelihood Ratio Test
GPS	Global Positioning System
IFFT	Inverse Fast Fourier Transform
INS	Inertial Navigation System
IP	Internet Protocol
LOS	Line of Sight
LPI	Low Probability of Intercept
MIMO	Multiple Input Multiple Output
MISO	Multiple Input Single Output
MUSIC	Multiple Signal Classification
MVDR	Minimum Variance Distortionless Response
PAR	Phased Array Radar
PARAFAC	Parallel Factor Analysis
PDF	Probability Density Function
PPS	Pulse per Second
PRF	Pulse Repetition Frequency
PRI	Pulse Repetition Interval
PW	Pulse Width

RAM	Random Access Memory
RCS	Radar Cross Section
RPM	Revolutions Per Minute
RF	Radio Frequency
Rx	Receive
SCPI	Standards Commands for Programmable Instruments
SDR	Software Defined Radio
SISO	Single Input Single Output
SNR	Signal to Noise Ratio
STAP	Space Time Adaptive Processing
STC	Sensitivity Time Control
TDM	Time Division Multiplexing
Tx	Transmit
UHD	USRP Hardware Driver
ULA	Uniform Linear Array
USRP	Universal Software Radio Peripheral
VHF	Very High Frequency

1 Introduction

1.1 Background

MIMO concepts were first introduced in communications to alleviate channel fading and have recently received a lot of interest for improving radar. The concept of implementing multiple signals for a radar were first conceived in the 1990s with systems such as RIAS which was a French prototype VHF radar that used orthogonal waveforms to detect targets at long range [1].

A modern naval radar must detect and track multiple surface targets in both littoral and open ocean environments so that it can provide early warning against targets and prioritize weapon systems against the greatest threats. Threats such as submarine periscopes, fast attack craft or wave gliders have a small radar-cross section and become increasingly difficult to detect when there is significant sea clutter. With a small boat swarming attack in littoral waters, every second earlier that a ship can detect and maintain its radar picture provides precious battle space and reaction time to fight.

The first step in detecting a target at an unknown location is searching an area. Rotating or electronically scanning radars perform this function by sweeping an area with a narrow beam and are only searching a defined sector for a short period of time. If the target is in an atmospheric or multipath null during this time, the target can be missed. A MIMO radar is capable of searching an entire area with a wide transmit beam pattern after a few orthogonal pulses and performs its beamforming on reception. However, with a wider transmit beam, there is less directivity for a MIMO radar which results in less energy being reflected off targets similar to a low probability of intercept (LPI) radar. If the search area is large, such as a dedicated 90° sector for a phased array panel on the side of a ship, then a MIMO radar is superior in detection time and picture refresh rate. It also leads to having more cumulative radar returns of a target over time through independent transmit and receive channels, minimizing the effects of atmospheric or multipath nulls [2].

1.2 Problem Statement

Although MIMO radar offers advantages over a traditional radar, it also presents significant drawbacks. Firstly, because the MIMO radar radiates a target with less gain during a transmission, it requires a longer coherent processing interval (CPI) to maintain the same signal to noise ratio (SNR) as a phased array radar [3]. During a CPI of the MIMO radar, a moving target will induce a Doppler return, which, if unaccounted for, can significantly degrade the performance of the MIMO radar performing coherent integration. The characteristics and changes in a target have a more profound effect on the probability of detection in a MIMO radar system than it does for a phased array radar because a MIMO radar requires a longer CPI.

Secondly, because a MIMO radar uses orthogonal waveforms, it leads to increased signal processing complexity and required operations [4]. Additional matched filters, the formation of a virtual array and potential cross-correlation between orthogonal signals all lead to increased processing requirements. For moving targets, Doppler compensation is required for a MIMO radar to maintain the equivalent SNR of a phased array radar because a MIMO radar requires to coherently integrate the returns over its longer CPI.

1.3 Thesis Statement

This thesis explores the limitations and advantages of a MIMO radar and determines that it can be used by a navy ship to detect surface targets. MIMO radar is better than a phased array radar for detecting multiple slow moving surface naval targets in a cluttered sea environment. Simulated and empirical radar return measurements from stationary and slow moving targets from an active phased array and a MIMO radar will be analyzed and compared.

1.4 Methodology

The aim of this thesis is not to determine if a MIMO radar could replace a traditional phased array, but rather investigate how it could complement an existing radar suite onboard a naval ship. Consequently, the simulations and experimental platform are designed for use with a colocated antenna to determine if MIMO radar processing could be used with an existing phased array on a naval ship. Using the existing infrastructure on a ship is critical from a cost and implementation perspective, as significant upper deck refits are rare. Surface targets were chosen as the primary target of interest for two reasons. Firstly, ocean surface targets move at considerably lower speeds, 10-15 m/s, than air targets, 50 m/s and above. As mentioned, MIMO requires a longer CPI to achieve the same SNR from a target as a phased array. Fast moving and high accelerating targets such as missiles or aircraft introduce limitations on integration times [5], which could prevent detection. Secondly, examining surface targets minimizes the variables of the targets and limits the maximum detectable range of the radar to the radar horizon.

The first step required to test the thesis statement is to create a radar simulation model that compares a MIMO radar with a phased array radar under a variety of scenarios. MATLAB and Simulink are used to simulate both radars. Both use traditional radar signal processing techniques to improve detection, such as integration and sensitivity time control (STC). The models also generate antenna patterns, receiver losses, and environmental effects to closely mimic a real radar system. Various simulations are conducted to evaluate the performance of the two developed models and to compare them with theory.

The second phase of this thesis is to design and build a MIMO radar platform that can leverage the radar simulations. Two design options are explored: the first one is based on software defined radios (SDR) and the second one is based on a Performance Network Analyzer (PNA-X). In addition, a uniform linear array is designed and built from microstrip patch antennas for use with the experimental platform.

Finally, the last portion of this thesis conducts experiments in the controlled environment of an anechoic chamber to validate the experimental radar platform and to demonstrate its ability to detect and distinguish multiple targets.

1.5 Thesis Organization

Chapter 2 provides a high-level overview of a MIMO radar. It presents the definition of a MIMO radar system and provides a theoretical comparison between a MIMO radar and a phased array radar. Specifically, it discusses beam patterns, orthogonal waveforms, SNR, and differences in coherent processing intervals (CPI).

Chapter 3 describes the requirements and design of the Simulink-based simulations for the MIMO and phased array radars. Details are provided for environmental and antenna simulation as well as each signal processing method used by the radar systems. Similarities and differences between the two radar systems are highlighted throughout this chapter. Results from various scenarios are presented where comparisons are drawn between the two radar systems. The scenarios are used to validate the design of the simulations against theory and conclusions are drawn on the performance of a MIMO radar system being used to detect ocean surface targets.

Chapter 4 presents the experimental MIMO radar platform as well as the design of a microstrip patch uniform linear array (ULA). Several radar design options were explored and are discussed. Static measurements are taken in the anechoic chamber to validate design and MIMO radar theory.

Chapter 5 concludes the thesis and discusses areas of future research for the use of MIMO radar in detecting slow moving targets.

2 Literature Survey

2.1 Multiple-Input Multiple-Output Radar Definition

There is a broad range of definitions for MIMO radar which leads to a wide variety of methods for construction and implementation [3]. Generally, MIMO radar is implemented through either spatial diversity in antennas or through colocated antennas using orthogonal independently transmitted waveforms [6]. As this thesis is examining the potential use of a MIMO radar for detecting surface targets from a naval ship, only the colocated antenna configuration will be examined. A generic MIMO radar design is illustrated in Figure 2.1 [3] where there are M independent orthogonal transmitters and N receivers. Each receiver would have M matched filters to correspond to the M distinct transmitted waveforms. Having M independent transmitters and N receivers produces MN paths for the return from the k^{th} target which in turn creates a virtual array with a larger effective aperture in comparison to a phased array. The generic received signal for the system illustrated in Figure 2.1 is as follows [3,6]:

$$y_n[n] = \sum_{k=1}^{K} \alpha(\theta_k) \sum_{m=1}^{M} e^{-j\omega_c \tau_{mn}(\theta_k)} s_m[n] + w_n[n] \tag{2.1}$$

where α is the complex amplitude of the k^{th} return signal from a target located at angle θ_k, s_m are the baseband samples of the m^{th} transmitted signal, $\tau_{mn}(\theta_k)$ is the total phase delay between the m^{th} transmitting element, the k^{th} target, and the n^{th} receiver, ω_c is the carrier frequency, $[n]$ is the time index, and w_n is additive white Gaussian noise. The noise vector, $w_n[n]$, is zero-mean complex Gaussian with a covariance matrix $R_w=\sigma^2 I_m$. It is important to note in (2.1) that MIMO radar takes the sum of returns from all targets whereas a phased array radar will only have a return from its directed beam. So long as MIMO can distinguish the received paths independently using orthogonal signals and matched filters, then it is able to achieve a ubiquitous mode where it is able to search an entire area in only a few short pulses instead of having to scan a beam through the same sector. Separating and distinguishing the independent transmit and receive paths is the most critical step in designing a MIMO radar as these signals are used to form the virtual array, will define the two-way antenna pattern, and contains the information necessary to conduct beamforming on reception.

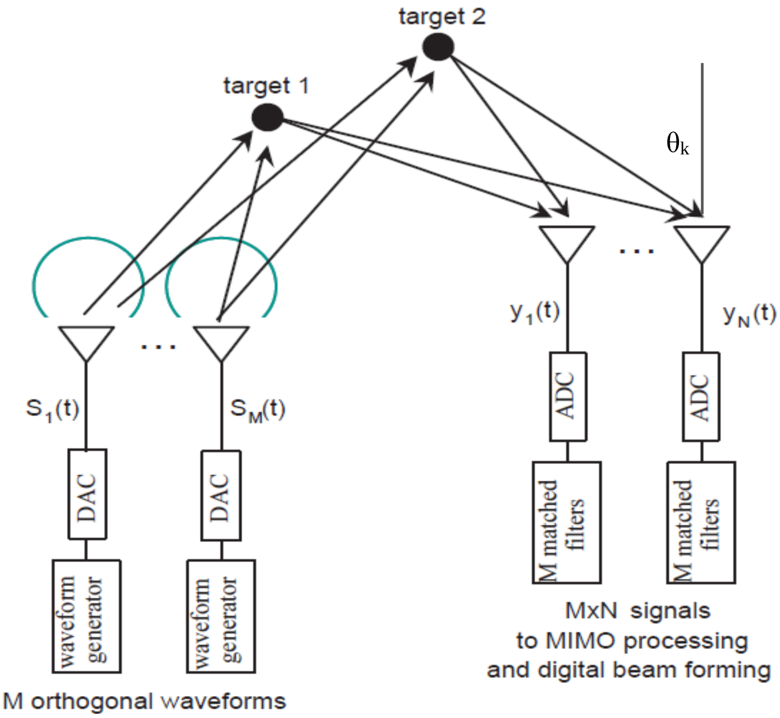

Figure 2.1 Generic MIMO radar with two targets [3]

2.2 Orthogonal Waveforms

Orthogonal signals allow for simultaneous transmission from all elements without the requirement of beamforming on transmission, but rather on reception. If the correlation of two transmitted signals is equal to zero, then they are considered orthogonal, defined by (2.2). In other words, they do not share common energy and are considered independent of one another. Orthogonality prevents constructive interference among the transmitting elements and allows for independent transmit paths.

$$< s(t), p(t) > \; = \int_{-\infty}^{\infty} s(t)p(t)dt = 0 \qquad (2.2)$$

where $s(t)$ and $p(t)$ are two time varying signals. MIMO radar may achieve orthogonality in different ways, such as: diversifying the frequency of each individual transmitting element, transmitting different polarizations, or phase encoding each transmitted signal differently [3]. For slow moving or stationary targets, such as sea surface targets, orthogonality can also be achieved by transmitting the same waveform, but at different time intervals to avoid any interference. Separating the signals in time also eliminates any potential cross correlation of signals through target or environmental interactions [7]. The disadvantage of using time division multiplexing (TDM) is that it will take M times longer, where M is the number of transmitting elements, to survey a scene in comparison to simultaneously transmitted orthogonal waveforms.

The coherence matrix, R, for a M-element uniform linear array is defined as [6]:

$$\boldsymbol{R} = \frac{1}{N}\sum_{n=1}^{N} \boldsymbol{s}[n]\boldsymbol{s}^{H}[n] = \begin{bmatrix} 1 & \beta_{12} & \cdots & \beta_{1M} \\ \beta_{21} & 1 & \cdots & \beta_{2M} \\ \vdots & \vdots & \ddots & \vdots \\ \beta_{M1} & \beta_{M2} & \cdots & 1 \end{bmatrix} \tag{2.3}$$

where $s[n]=[s_1[n], ..., s_M[n]]$ is the transmitted Mx1 baseband signal vector from the M-element ULA, β_{ij} is the complex correlation between signals i and j, and ^{H} is the Hermitian operation. The phases of the diagonal, the coherent component of (2.3), control the two-way MIMO beam pattern on reception. The phase of this component can be manipulated through receive beamforming techniques such as phase-shift beamformers on receive to electronically steer the MIMO radar beam pattern to different directions. For orthogonal transmissions, ($\{\beta_{ij}\}_{i \neq j} = 0$) therefore, the coherence matrix, R, results in an identity matrix: $R = I_M$. For a fully coherent radar system such as an active phased array, there is only one coherent transmitted signal, s, across all elements, which results in R equaling one [6].

For MIMO radar, the orthogonal signals are simultaneously and independently transmitted with a directivity based on the element pattern of the antenna, typically 120° or wider [4]. Transmitting with a wide beamwidth creates a large volume search and results in the entire area of interest being scanned at once which in turn increases the dwell time on a target as well as improving Doppler resolution [6]. Conversely, to search the same volume, a phased array radar is required to scan its main beam by steering it in azimuth and elevation causing it to take longer to search the same sector. The significance of MIMO radar's improvement in volume search time over the phased array radar will depend on the phased array's scan rate and associated beamwidths. An in-depth analysis and summary of common MIMO orthogonal waveforms can be found in [7], which is summarized in Table 2.1 where LFMCW is the time-staggered linear frequency modulation continuous wave waveform, FDMA is frequency division multiple access, DDMA is Doppler division multiple access, and CDMA is code division multiple access.

Table 2.1 Summary of MIMO waveforms [7]

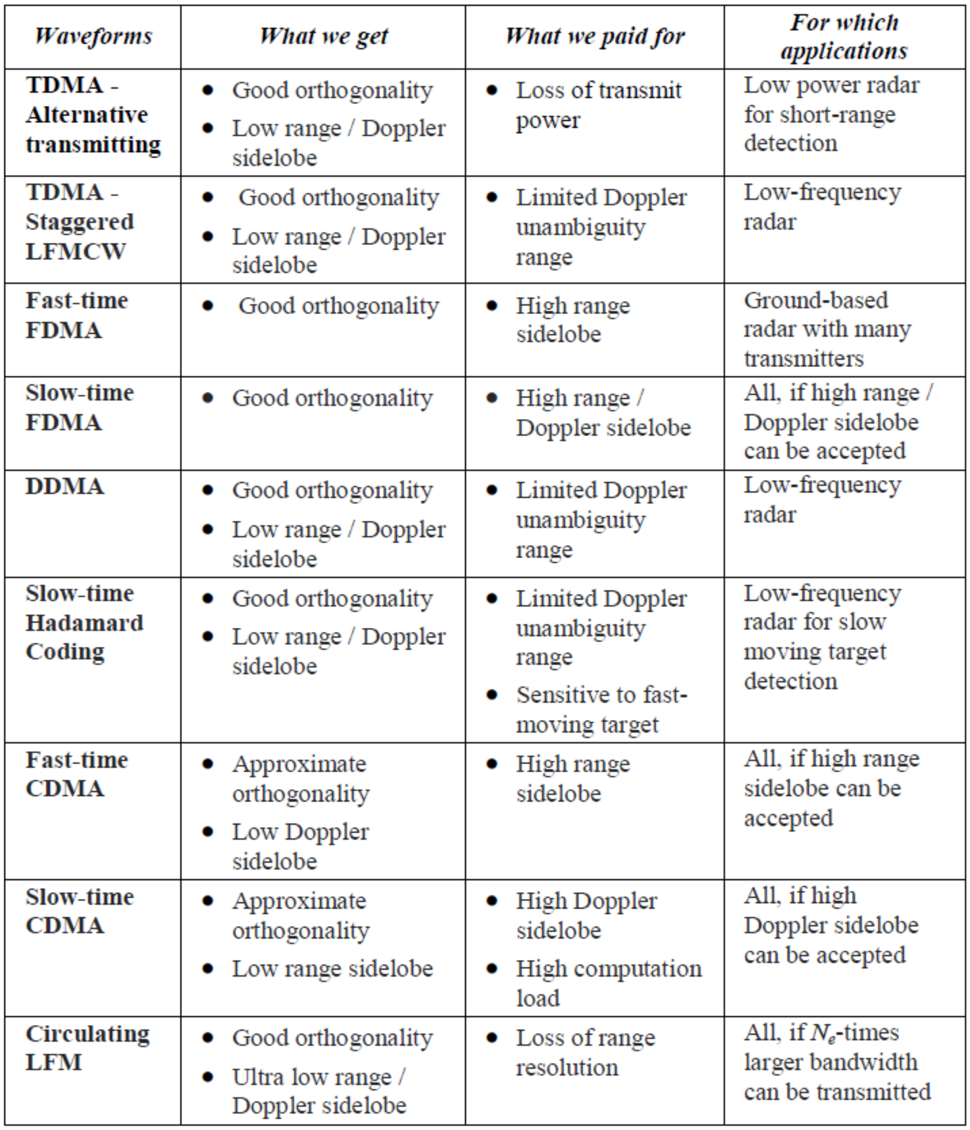

Waveforms	*What we get*	*What we paid for*	*For which applications*
TDMA - Alternative transmitting	• Good orthogonality • Low range / Doppler sidelobe	• Loss of transmit power	Low power radar for short-range detection
TDMA - Staggered LFMCW	• Good orthogonality • Low range / Doppler sidelobe	• Limited Doppler unambiguity range	Low-frequency radar
Fast-time FDMA	• Good orthogonality	• High range sidelobe	Ground-based radar with many transmitters
Slow-time FDMA	• Good orthogonality	• High range / Doppler sidelobe	All, if high range / Doppler sidelobe can be accepted
DDMA	• Good orthogonality • Low range / Doppler sidelobe	• Limited Doppler unambiguity range	Low-frequency radar
Slow-time Hadamard Coding	• Good orthogonality • Low range / Doppler sidelobe	• Limited Doppler unambiguity range • Sensitive to fast-moving target	Low-frequency radar for slow moving target detection
Fast-time CDMA	• Approximate orthogonality • Low Doppler sidelobe	• High range sidelobe	All, if high range sidelobe can be accepted
Slow-time CDMA	• Approximate orthogonality • Low range sidelobe	• High Doppler sidelobe • High computation load	All, if high Doppler sidelobe can be accepted
Circulating LFM	• Good orthogonality • Ultra low range / Doppler sidelobe	• Loss of range resolution	All, if N_e-times larger bandwidth can be transmitted

TDM MIMO was selected as the orthogonal waveform to be implemented in this thesis for its good orthogonality between transmitting elements, the simplicity to form a virtual array, and to reduce the number of matched filters required on reception. Furthermore, using TDM MIMO allows the use of the same waveform across all transmitting elements, allowing for a more direct comparison between the MIMO and phased array radars as there is no risk of cross correlation between the transmitting waveforms. Conversely, the disadvantage of using TDM is that it will take M times longer to form a virtual array, where M is the number of transmitting elements. Two specific waveforms were selected for use with TDM MIMO for this thesis: Zadoff-Chu [8] and Stepped-Frequency waveforms [9]. The Zadoff-Chu waveform was selected for the simulation work covered in Chapter 3 so that pulse compression could be achieved and Stepped-Frequency waveforms are used in Chapter 4 because of the restrictions of the platform selected to construct an experimental MIMO radar.

2.2.1 Zadoff-Chu Waveform

Zadoff-Chu is a periodic phased encoded sequence that is tolerant to Doppler [8] and is used in radar for pulse compression to improve the range resolution of a rectangular pulse. Consider a Zadoff-Chu phased-encoded transmitted signal, $s_m = \exp(j\varphi_m)$, where φ_m is defined as [8]:

$$\phi_{m,even} = \frac{\pi}{P}\, r\,(p-1)^2\,, \qquad P \text{ even} \tag{2.4}$$

$$\phi_{m,odd} = \frac{\pi}{P}\, r\,(p-1)p\,, \qquad P \text{ odd} \tag{2.5}$$

where P is the number of chips, r is the index sequence and is any integer that is a prime number that is divisible into P, and $1 \leq p \leq P$. The phase of the transmitted signal changes with respect to p, and P will define the pulse compression ratio of a rectangular pulse such that the compressed Rayleigh range resolution (equivalent to a 4 dB beam width), δR_c, will be defined as [10]:

$$\delta R_c = \frac{c\tau}{2P} \tag{2.6}$$

where c is the speed of light and τ is the pulse width of the transmitted waveform. (2.6) shows an improvement of P in range resolution over a traditional rectangular pulse. The unambiguous range, R_{unamb}, of a Zadoff-Chu waveform, (2.7), is defined by the pulse repetition interval (PRI) of the radar [10]. When using Zadoff-Chu waveforms with TDM MIMO, the PRI of the radar defines the wait time to alternate between different transmitting elements.

$$\mathrm{R}_{unamb} = \frac{c(PRI)}{2} \tag{2.7}$$

Figure 2.2 illustrates an example of how the phase of a transmitted signal changes for a Zadoff-Chu sequence of length, P=11.

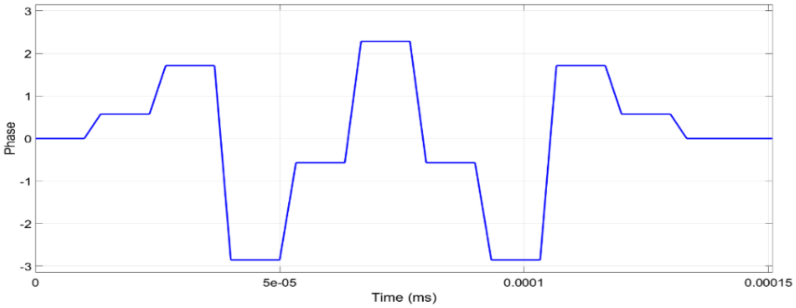

Figure 2.2 Phase of Zadoff-Chu sequence, length P=11

2.2.2 Stepped-Frequency Continuous Wave

The stepped-frequency waveform achieves high range resolution by generating synthetic Doppler frequencies by cycling through a band of transmission frequencies [9]. Radar returns are received and initially processed in the frequency domain before an Inverse Fast-Fourier transform (IFFT) is used for range calculations and beamforming. The Rayleigh range resolution, Δr_{sf}, for a stepped-frequency waveform is defined as [9]:

$$\Delta r_{sf} = \frac{c}{2N\Delta f_s} \tag{2.8}$$

for N frequency steps of Δf_s (Hz). Therefore, the total sweep bandwidth of the stepped-frequency waveform is $B = N\Delta f_s$. As an IFFT is required to determine range, the maximum range that can be measured before ambiguities exist is N times the range resolution, Δr_{sf}. Therefore, the unambiguous range, Δr_{unamb}, of a stepped-frequency waveform is defined as [9]:

$$\Delta r_{unamb} = \frac{c}{2\Delta f_s} \tag{2.9}$$

Figure 2.3 [11] illustrates the expected return of a radar signal in the frequency and time domains of a stepped-frequency continuous wave waveform where the total sweep duration and the duration for a single frequency, T_{tone}, are shown. When using stepped-frequency continuous wave waveforms with a TDM MIMO radar, the sweep duration defines the wait time to alternate between different transmitting elements.

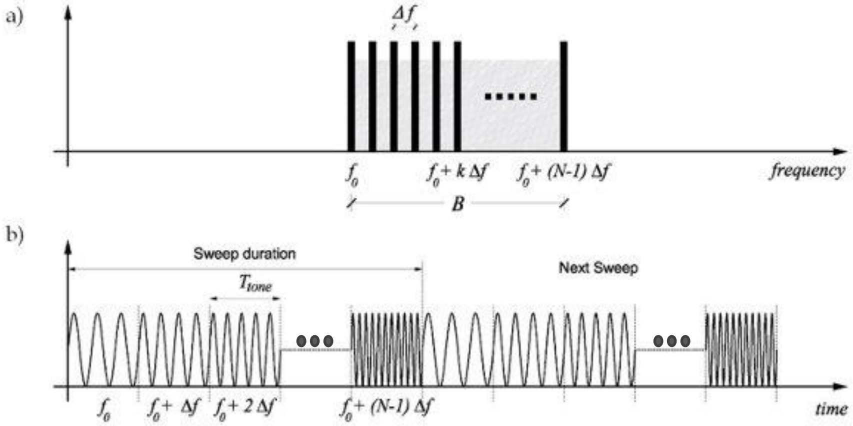

Figure 2.3 Frequency and time response of a Stepped-Frequency waveform [11]

2.3 Antenna Architecture and Virtual Array

A significant advantage of a colocated antenna MIMO radar over a traditional phased array is the creation of a virtual array using the far field approximation. When a MIMO radar transmits *M* independent orthogonal signals, and receives echo returns with *N* receivers with uniform weighting, a total of *MN* channels is processed creating a virtual array of up to *MN* receive elements [6]. The configuration of the virtual array itself is dependent upon the relative spacing of the transmit and receive elements to one another and is defined as the spatial convolution between the transmit and receive elements [4]. For example, the location of the virtual array elements for a uniform linear array with elements along the x-axis is defined as [12]:

$$Virtual\ Array(x) = \sum_{m=0}^{M-1} \sum_{n=0}^{N-1} \delta(x - (x_m + x_n)) \qquad (2.10)$$

where x_m and x_n are the physical locations of the m^{th} transmit element and the n^{th} receive element.

There are two noteworthy improvements that a virtual array provides [3]. Firstly, it extends the array aperture beyond the physical number of elements by leveraging the multiple transmit/receive paths of MIMO to create a virtual array [4]. This does not improve the two-way radiation pattern resolution of the MIMO radar over a phased array, but it does allow for different beamforming techniques to be applied on reception such as space-time adaptive processing (STAP). Each received channel is orthogonal and independent of one another, which allows for each channel to be processed separately whereas a phased array radar receives only a single coherent signal and must process the received data together. Secondly, a virtual array could be used to fill the gaps in a sparse array maintaining the same resolution but with fewer elements. Implementing a sparse array would not only have a cost saving from fewer elements, but it would also have the added benefit of reducing mutual coupling between antennas and eliminating grating lobes.

Figure 2.4 [13] illustrates an example of how a virtual array is formed using (2.10). The physical individual transmit and receive antennas and their associated locations are on the top two rows whereas the virtual array is on the bottom. The spatial distance between the transmit and receive antennas will define the location of the virtual array elements. In this example, there are 3 transmit elements and 5 receive elements resulting in a virtual array of 15 elements. For instance, the first five virtual array elements are formed from the spatial convolution of the transmitter located at position 0 and the 5 receivers. The second and last third of the virtual array elements are formed from the spatial convolution of the 5 receivers with the transmitters located at positions 5 and 10, respectively.

It is also important to highlight that the two-way antenna pattern of a full MIMO virtual array is comparable to that of a phased array with the same number of elements in a uniform linear array [14]. The antenna pattern depends on two factors: the element factor, $E(\theta)$ and the array factor, $A(\theta)$. $E(\theta)$ is dependent on the radiation pattern of the individual antennas that make up the uniform linear array

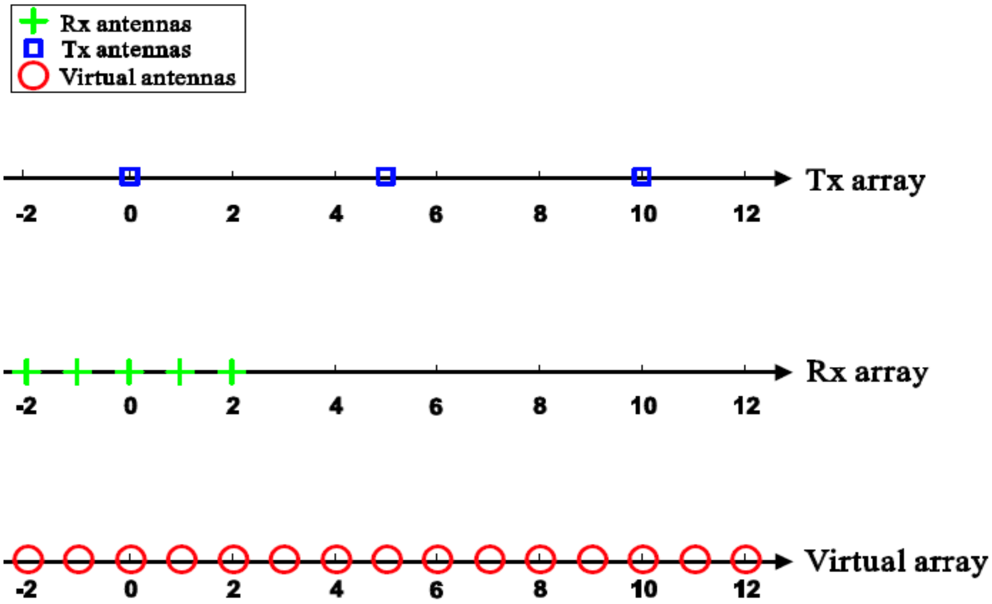

Figure 2.4 An example of a virtual array structure [13]

whereas $A(\theta)$ is a summation of the vector contributions of all elements. A uniform linear array with N elements has a normalized one-way power array factor of:

$$A_N(\theta) = \frac{\sin^2[N\pi\left(\frac{d}{\lambda}\right)\sin\theta]}{N^2\sin^2[\pi\left(\frac{d}{\lambda}\right)\sin\theta]} \tag{2.11}$$

where d is the uniform spacing between the elements, λ is the operating wavelength and θ is the angle away from the broadside of the array. Having the uniform linear array act as a phased array results in the transmit radiation power, $G_{PA,Tx}(\theta)$, and the receive radiation power, $G_{PA,Rx}(\theta)$, being equal [14]:

$$G_{PA,Tx}(\theta) = G_{PA,Rx}(\theta) = E(\theta)A_N(\theta) \tag{2.12}$$

Therefore, the two-way radiation pattern for a phased array is defined as:

$$G_{PA,2-way}(\theta) = G_{PA,Tx}(\theta)G_{PA,Rx}(\theta) = E(\theta)^2 A_N(\theta)^2 \tag{2.13}$$

For a MIMO radar with the same number of N elements, the transmit radiation pattern is only dependant on the element factor, E(θ), of the individual antennas. No constructive interference or beamforming takes place as the transmitted signals are orthogonal to one another. However, on receive the effective array is the spatial convolution of the N element linear array. So, on reception, a MIMO radar will account for an array factor of $A_N(\theta)^2$ in addition to the element factor. Therefore, the two-way radiation pattern for a MIMO radar is the same as a phased array radar and is given by [14]:

$$G_{MIMO,2-way}(\theta) = G_{M,Tx}(\theta) G_{M,Rx}(\theta) = E(\theta)^2 A_N(\theta)^2 \quad (2.14)$$

Figure 2.5 [14] depicts experimental results comparing the same 10-element uniform linear array with a phased array and MIMO radar. Figure 2.5 implies that a MIMO radar will achieve the same level of resolution and gain as a phased array radar after beam forming and integration on reception. Also, note that there is flexibility in the MIMO antenna pattern depending on how many elements are

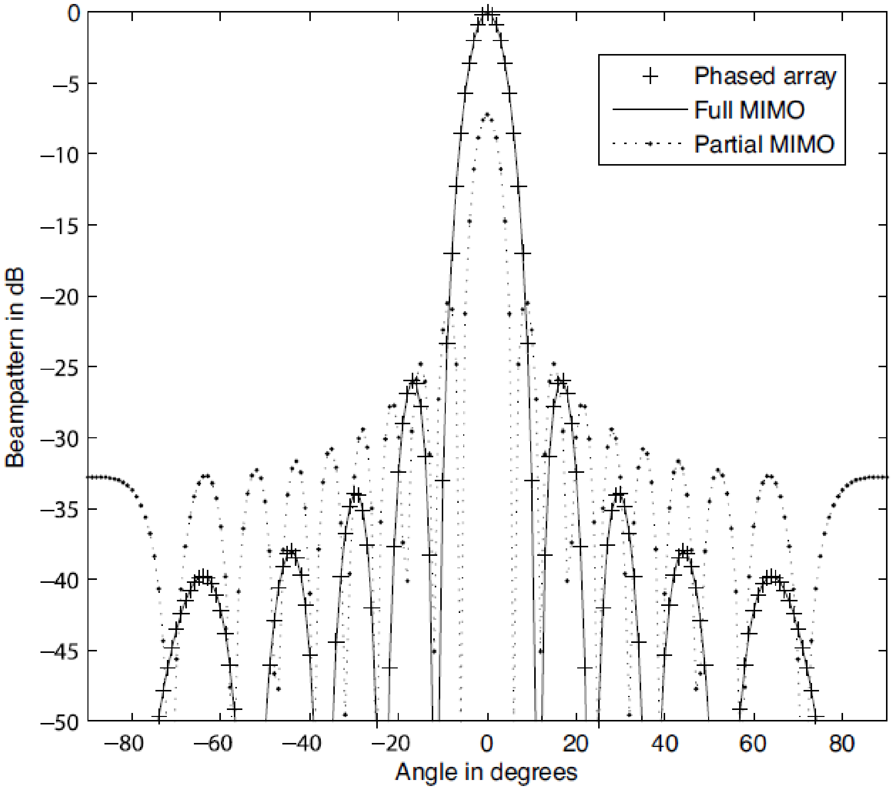

Figure 2.5 Phased array and MIMO radar beam pattern for a 10-element linear array [14]

actively transmitting or receiving. As a colocated MIMO radar performs beamforming on receive, it can manipulate the received data to perform different beam patterns by adjusting which elements to process, effectively changing the spatial convolution of (2.10) and changing the two-way radiation pattern.

2.4 Signal to Noise Ratio

A MIMO radar transmits with a gain based on the element factor, $\mathrm{E}(\theta)$, which is typically a wide beamwidth allowing the radar to search a greater instantaneous area compared to a phased array. The trade-off for MIMO having a greater instantaneous search area is that less energy will return from targets compared to a phased array with a transmission pattern based on both the array and element factor, $E(\theta)A_N(\theta)$. Having less power directed towards the target could have a negative effect on the SNR of the target and the ability for a MIMO radar to detect it.

SNR or clutter-to-noise ratio (CNR) can only be improved by a MIMO radar if sufficient integration can be achieved. The SNR of a MIMO radar is only comparable with that of a phased array radar if the pulses are integrated over a CPI, usually resulting in significantly longer processing time [15]. DRDC provides an analysis of how MIMO radar affects SNR in [3] and is summarized in Table 2.2. In Table 2.2, single input single output (SISO) is considered as the conventional analog beamforming phased array. SISO is used as the basis for comparison of various radar configurations after digital beamforming (DBF) where the N receive signals are summed and after MIMO processing, where M orthogonal transmit signals are matched filtered and combined. P_t is the peak power that is applied to the single output channel while G_t and G_r are the associated transmit and receive antenna gains. θ_A and θ_E are the azimuth and elevation beamwidths and the bandwidth of the receiver, B, is inversely proportional to the pulse width, τ. The dwell time on the target, T^{dwell}, is defined as half-power beam cross-sectional area divided by the scan rate whereas the number of beams, N_o, is given by the total search area divided by the half-power beam cross-sectional area.

Multiple input single output (MISO) refers to a phased array with M orthogonal transmit channels that share the same frequency band with a single receiver. Due to subdividing the transmission into M channels, the peak power, P_t, is also lowered by a factor of M. The MIMO architecture used in the analysis was M orthogonal transmit and N receive colocated antennas. The three MIMO variations

Table 2.2 Signal-to-noise ratio comparisons for phased array and colocated antenna MIMO radar [3]

Architecture	Tx power	Tx gain	Rx gain	beamwidths	# of beams	dwell time	SNR single pulse	SNR after DBF	SNR after DBF + MIMO	integrated SNR
SISO	P_t	G_t	G_r	θ_A, θ_E	N_0	T_0^{dwell}	SNR_0	SNR_0	SNR_0	SNR_0^{int}
SIMO	P_t	G_t	$\frac{G_r}{N}$	θ_A, θ_E	N_0	T_0^{dwell}	SNR_0	SNR_0	SNR_0	SNR_0^{int}
Spoiled tx beam SIMO	P_t	$\frac{G_t}{M}$	$\frac{G_r}{N}$	$a\theta_A, e\theta_E$	$\frac{N_0}{M}$	MT_0^{dwell}	$\frac{SNR_0}{MN}$	$\frac{SNR_0}{M}$	$\frac{SNR_0}{M}$	SNR_0^{int}
MISO same freq. band	$\frac{P_t}{M}$	$\frac{G_t}{M}$	G_r	$a\theta_A, e\theta_E$	N_0	T_0^{dwell}	$\frac{SNR_0}{M^2}$	$\frac{SNR_0}{M^2}$	$\frac{SNR_0}{M}$	$\frac{SNR_0^{int}}{M}$
MIMO same freq. band	$\frac{P_t}{M}$	$\frac{G_t}{M}$	$\frac{G_r}{N}$	$a\theta_A, e\theta_E$	$\frac{N_0}{M}$	MT_0^{dwell}	$\frac{SNR_0}{M^2N}$	$\frac{SNR_0}{M^2}$	$\frac{SNR_0}{M}$	SNR_0^{int}
MIMO adjacent freq. bands, one receiver $B \simeq MB_s$	$\frac{P_t}{M}$	$\frac{G_t}{M}$	$\frac{G_r}{N}$	$a\theta_A, e\theta_E$	$\frac{N_0}{M}$	MT_0^{dwell}	$\frac{SNR_0}{M^3N}$	$\frac{SNR_0}{M^3}$	$\frac{SNR_0}{M^2}$	$\frac{SNR_0^{int}}{M}$
MIMO adjacent freq. bands, M analog receivers $B \simeq B_s$	$\frac{P_t}{M}$	$\frac{G_t}{M}$	$\frac{G_r}{N}$	$a\theta_A, e\theta_E$	$\frac{N_0}{M}$	MT_0^{dwell}	$\frac{SNR_0}{M^2N}$	$\frac{SNR_0}{M^2}$	$\frac{SNR_0}{M}$	SNR_0^{int}

were transmission at the same frequency with orthogonal signals achieved through phase coding, adjacent frequency band for achieving orthogonality with a single receiver per channel, and lastly adjacent frequency bands but with M receivers per channel.

As seen in Table 2.2, after integrating radar returns M times over a time, MT^{dwell}, MIMO has the same integrated SNR as a conventional phased array radar. It is important to note that the final SNR is not from a single pulse, but from integration. The coherently integrated SNR is defined as [3]:

$$SNR_0^{int} = \frac{P_{avg} G_t G_r \sigma \lambda^2}{(4\pi)^3 R^4 L k_B T F} T^{dwell} \tag{2.15}$$

where σ is the target's radar cross section (RCS), λ is the wavelength, L represents losses, k_B is Boltzmann's constant, F is the noise figure, T is system temperature and P_{avg} is the average transmitted power. The analysis completed in Table 2.2 was done using free space propagation and without considering multipath effects. Accounting for these effects would improve the SNR for the MIMO radar architectures compared to a phased array.

2.5 Doppler and Coherent Processing Interval

As a MIMO radar requires a CPI of MT^{dwell} to maintain the same SNR as a phased array radar, targets moving with a high radial velocity causing a Doppler shift in the radar return could be in different range cells or radar returns could destructively interfere in the integration process for a given CPI. Therefore, a target with a high velocity could impede a MIMO radar's ability to detect the target. The focus of this thesis is on slow moving or stationary surface targets, so encountering this phenomenon is less likely, but a discussion is still warranted as detecting and compensating for moving targets is a weakness of MIMO radar and remains a significant research area.

Coherent integration attempts to minimize the effect of the environmental noise and amplify weak signals by averaging complex returns over a specific interval. As background white Gaussian noise is zero mean, by averaging the radar returns over an interval, the average voltage of the noise returns will approach zero while the returns from targets will add up constructively to increase the voltage of the return signal. If the target return signals are summed coherently over M samples, the SNR will increase by a factor of M [10]. Figure 2.6 [10] illustrates an example of L range bins, where the fourth range bin is coherently integrated over a CPI of *M* returns.

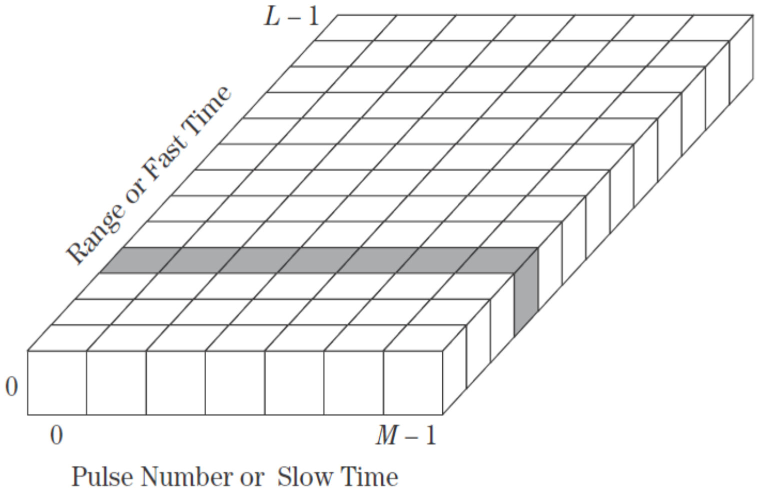

Figure 2.6 Coherent integration of M returns on the fourth range cell [9]

The coherent integration improvement factor of *M* on SNR is under ideal conditions for a stationary target and is not practical. A moving target will induce a Doppler shift on the return signal by [16]:

$$f_d = \frac{2v_r}{\lambda_o} \tag{2.16}$$

where f_d is the shift in the received frequency, v_r is the radial velocity of the target, and λ_o is the operating wavelength of the transmitted radar pulse. A shift in the received frequency will induce a change in the received phase. As coherent integration accounts for both magnitude and phase of the return signal, a changing phase over an integration period could induce negative effects. The output from a coherent integrator of *M* pulses is defined as:

$$y = \sum_{m=1}^{M} Ae^{j(2\pi f_d mT+\varphi)} \tag{2.17}$$

where φ is the constant return phase of the signal from the target for a given travel distance, T is the PRI of the radar, and A is the amplitude of the return. Without compensating for f_d, the Doppler component of (2.17) will degrade the coherent integrator. The significance of the degradation will depend on the total phase change caused by the Doppler speed of the target for a given number of integrations over a CPI. Therefore, the relationship between $2\pi f_d MT$ will determine the total phase change caused by the moving target. Consider a target approaching a radar at a constant speed where the radar performs $M=20$ integrations over a constant PRI, T. Figure 2.7 illustrates the normalized response of the coherent integrator from (2.17) for two complete 2π cycles of Doppler shift. The total Doppler phase change, $2\pi f_d MT$, will determine the efficiency of the coherent integrator. As 20 integrations are used in this example, Figure 2.7 will repeat itself for every 20 cycles of 2π. Note that if A is assumed to be constant, then (2.17) is recognized as the M-point DFT of a window function of duration MT. As such, y is expected to be a sinc function, which it is.

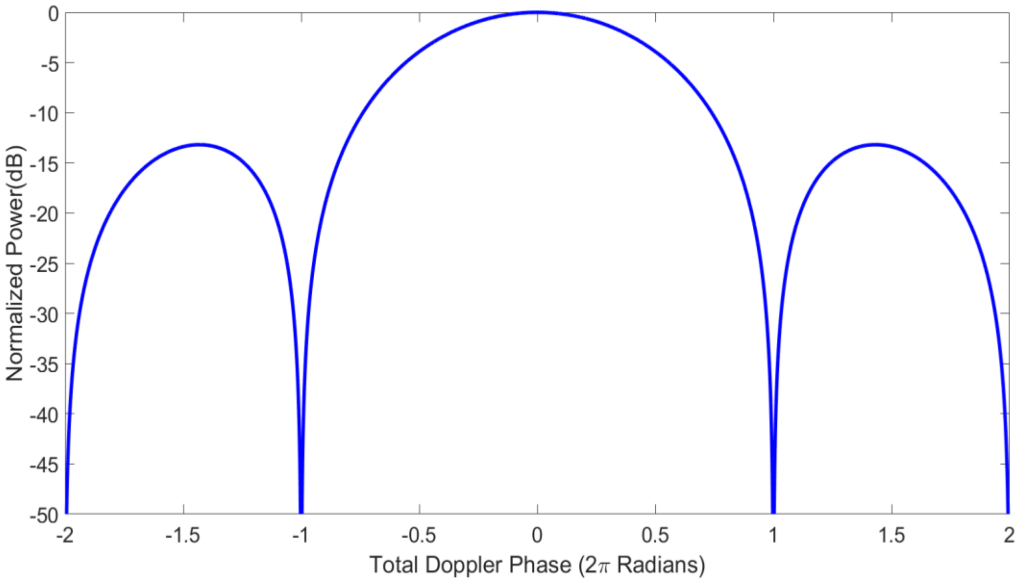

Figure 2.7 Coherent integration efficiency for a moving target

The 4 dB loss efficiency point in Figure 2.7 is approximately 0.5, which is equivalent to a total Doppler phase change of π over a given CPI. Stipulating that the total Doppler shift of the received signal over a CPI must be less than π, the following relationship can be stated:

$$2\pi f_d MT < \pi \tag{2.18}$$

The relationship of (2.18) is the limiting factor for the number of integrations that can take place for a given CPI for a radar that does not correct for Doppler. Rearranging (2.18) with (2.16), the following equation must be satisfied for a coherent integrator without Doppler correction:

$$M < \frac{PRF\ \lambda_o}{4v_r} \tag{2.19}$$

where *PRF = 1/T*. Consider two ships approaching each other directly at their maximum speed of 30 knots, or a relative radial speed between them of approximately 30 m/s. One ship is using an L-band MIMO radar with an operating frequency of 1.5 GHz and a PRF of 15 kHz while the other ship is using an X-band MIMO radar with an operating frequency of 9 GHz with the same PRF. If both ships are trying to detect each other using coherent integration, applying (2.19), the S-band radar will be able to integrate *M=25* pulses while the X-band radar will only able to integrate *M=4*. Again, this assumes that no Doppler filtering or compensation is being applied to the radars. This analysis demonstrates that a lower operating frequency MIMO radar will coherently integrate at a greater efficiency and is better suited for detecting moving surface targets.

As mentioned, compensating for Doppler and moving targets is an active research area for MIMO radar. DRDC [5,17] provides an in depth analysis with experimental results on comparing the probability of detection of a moving target for MIMO radar and a conventional beam steering radar. They conclude that slower moving targets are detected further in range from orthogonal waveforms while higher radial velocity targets are detected further in range using sector search directed beams such as a phased array. They also determined that for a larger number of orthogonal MIMO elements, although this provides greater flexibility for the MIMO radar in beamforming, it drastically degrades the probability of detecting high-velocity targets. Some methods to compensate for velocity and acceleration for MIMO radar include time domain approaches [12], various methods using the Fourier transform [18,19], and frequency domain approaches [20].

2.6 Target Detection and Estimation

MIMO radar allows the use of adaptive localization and detection techniques directly which is an advantage over a phased array radar [21]. These techniques use algorithms based on statistics mostly from Gaussian distributions to improve resolution and interference rejection capability, but at a cost of a higher computational load due to the independent orthogonal signals and the beam forming that is completed on reception [4].

There are a wide variety of algorithms for MIMO radar target detection and estimation. The main parameters that are estimated are direction of arrival and target location and velocity. The most common estimation method used for direction of arrival for MIMO is the Estimation of Signal Parameters via Rotational Invariance techniques (ESPRIT) [22]. Other forms of estimation include Multiple Signal Classification (MUSIC) [23], parallel factor analysis (PARAFAC) [24] and Capon [25]. For target detection and clutter rejection, the generalized likelihood ratio test (GLRT) [6] is often used while Cramer-Rao bound (CRB) [21] is used to evaluate the accuracy of the MIMO estimators to localize targets. Ref [3] also presents an excellent literature review for various papers discussing target detection and estimation techniques. Target detection and estimation in MIMO radar remains an active area of research.

Phase-shift narrowband beamforming and a cell-averaging constant false alarm rate (CFAR) detection are well-stablished processing techniques for radar target localization and detection. These techniques are used in this thesis with a MIMO radar for their ease of implementation and to allow for equal comparison to a phased array radar.

2.6.1 Cell-Averaging CFAR Detector

A radar detector such as cell-averaging CFAR determines whether or not a target is present. An echo return from a radar will either contain returns from a target plus some interfering noise or just interference such as receiver noise or sea clutter [10]. Interference can cause a radar to miss detecting a real target or can sometimes lead to the creation of false targets. The probability of either of these occurring depends on the SNR, which is the ratio of the return signal strength and the variance of the noise level. Therefore, the SNR will define the probability of a target being above a specific threshold, or probability of detection, P_D, as well as the probability of the noise creating a false alarm above that same threshold, P_{FA}.

Selecting the proper detection threshold is done through random process modeling and statistical analysis. Using a MIMO radar and simplifying (2.1) so that the sum of the return signal from a target is expressed as *z* and the sum of the white Gaussian noise component is expressed as *w*, then a single target detector must decide between two hypotheses:

$$\begin{aligned} H_0 &: \ y = w \\ H_1 &: \ y = z + w \end{aligned} \tag{2.20}$$

where H_0 is background white Gaussian noise, the null hypothesis, and H_1 is a target return plus noise. The received radar signals are considered Gaussian random processes; therefore, two probability density functions (PDFs) can be defined as $p_y(y|H_0)$ and $p_y(y|H_1)$. For any radar measurement, *y*, the GLRT decision rule can be applied [26]:

$$\frac{p_y(y|H_1)}{p_y(y|H_0)} \gtrless_{H_o}^{H_1} T_\Lambda \tag{2.21}$$

where T_Λ is a detection threshold defined for a given P_{FA}. Figure 2.8 [10] illustrates an example of both PDFs from (2.20) depicting the areas associated with different probabilities. The distance separating the means of the two PDFs is related to the SNR. Increasing the SNR will further separate the two PDFs, lowering the overlap between them, thus increasing P_D and lowering P_{FA}. Another method to increase the SNR is to lower the variance of the noise as this will also reduce the amount of overlap between the two PDFs.

It can be shown that (2.21) can be reduced to form a square law detector [10]:

$$|y|^2 \gtrless_{H_o}^{H_1} T \tag{2.22}$$

and that since the magnitude of the noise follows a Rayleigh distribution, the detection threshold, *T*, must satisfy the following equation:

$$T = -\,\sigma_n^2 \ln(P_{FA}) \tag{2.23}$$

where σ_n^2 is the variance of the noise. Generally, a cell-averaging CFAR detector will use (2.21) to set the threshold for individual resolution cells of the radar. It will do this by measuring the returns of neighbouring cells to determine σ_n^2 and apply it to (2.21) with a user-defined P_{FA}. Guard cells are commonly used around the cell under test so that if a target is present it does not artificially increase σ_n^2.

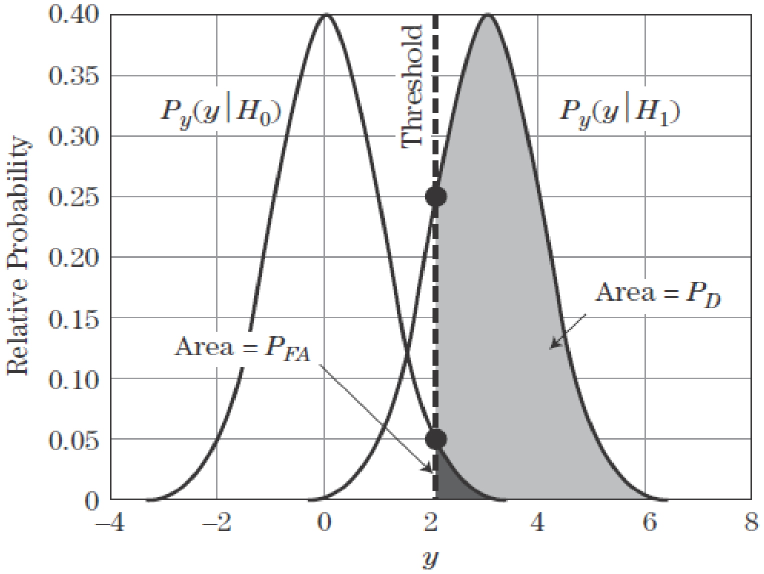

Figure 2.8 Gaussian probability density functions of noise and a target [9]

2.6.2 Phase-Shift Beamforming

A phase-shift beamformer is inefficient computationally in determining the bearing of a target when compared to a high-resolution technique such as MUSIC or ESPRIT [22,23]. For instance, ESPRIT can determine the angle of arrival of targets and scan an entire search area by translating the received signals to form matching pairs and then rank them by finding the eigenvalues to determine the angle of arrival. Conversely, since a MIMO radar performs beamforming on receive, a phase-shift beamformer must apply steering weights to the received signal for each element in the virtual array and electrically scan the area of interest. The larger the scan area, the greater number of computations required for a phase-shift beamformer. Having said that, even though there are more computations, because a MIMO radar completes beamforming on receive, these calculations can be performed in parallel instead of sequentially, thus minimizing the required time to scan an area. Parallel processing of angles is not possible in a phased array radar as beamforming is performed on transmission.

To electrically steer a beam, the pattern of the virtual array must be scanned to an angle θ_o by applying incremental offsets in phase to each element so that the phase differs as follows [16]:

$$\theta(n)_{Off} = 2\pi \frac{nd}{\lambda} \sin\theta_o \qquad (2.24)$$

where d is the separation between the elements, λ is the wavelength of the transmitted signal, and n ranges from 1 to N with N equalling the number of elements in the array. A phased array radar will apply the offsets from (2.24) to individual elements on transmission and then again on reception while a MIMO radar will apply the offsets to the elements of a virtual array on reception only. A MIMO radar completes beamforming after coherent integration, therefore, $\theta(n)_{Off}$ can be applied to (2.17) so that the output of the individual virtual receive elements for a phase-shift beamformer equals:

$$y(n) = \sum_{m=1}^{M} Ae^{j(2\pi f_d mT + \varphi + \theta(n)_{Off})} \qquad (2.25)$$

The one-way normalized power array factor for a uniform linear array from (2.11) becomes [16]:

$$A_N(\theta) = \frac{\sin^2[N\pi\left(\frac{d}{\lambda}\right)(\sin\theta - \sin\theta_o)]}{N^2\sin^2[\pi\left(\frac{d}{\lambda}\right)(\sin\theta - \sin\theta_o)]} \qquad (2.26)$$

3 Software Simulations and Results

This chapter presents the design and results obtained from the software simulated phased array and MIMO radar systems. Section 3.1 outlines the radar requirements for the radar simulations. Section 3.2 describes the MATLAB and Simulink toolboxes required for the simulations and provides an overview of common aspects required in both radar systems, such as the targets and the environment. Section 3.3 presents the design of the simulated phased array radar whereas Section 3.4 describes the simulation of the MIMO radar. Section 3.5 provides results of the simulated systems and compares the performance of the two radar systems at detecting ocean surface targets. Finally, Section 3.6 summarizes this chapter and the conclusions drawn throughout it.

3.1 Simulation Requirements

The main objective of simulating the MIMO and phased array radars is to provide a direct comparison between them over a variety of scenarios. The simulations of the two radar systems must allow for fair comparison between them. Although some of the processing techniques or transmission methods will need to differ between the two radar systems to account for the different radar types, the simulations must be able to provide the same scenarios and environments.

The scenario will include at least five targets, both stationary and moving, each with variable RCS depending on the aspect angle of the target. The propagation path of the radar signals must account for two-way direct path loss as well as basic weather effects such as temperature, atmospheric pressure, and moisture. The simulations must also include sea clutter based on a specified sea state.

Different antenna types, such as dipoles and horns and their associated radiation patterns must be included. Individual antenna paths must be provided so that MIMO channels can be formed. Furthermore, a maximum of six antennas will be used to create the ULA. A limit of six antennas was selected based on the experimental setup. Such a number can also provide a radiation pattern with a reasonable main beam while limiting the simulation run time.

The radar simulations are required to be flexible in that radar settings such as power, frequency, pulse width (PW), waveform type, antenna spacing, etc. can be changed easily. The simulations must be able to simulate operational frequencies between L and X band. Transmitting waveforms should be selectable and will include a rectangular waveform as well as a waveform using pulse compression. Amplifiers must be provided in the simulation and will include noise figures and loss factors.

There are many signal processing techniques that can be used in a radar system. The radar simulations must provide: beamforming, sensitivity time control (STC), coherent integration, and a constant false-alarm rate (CFAR) detector. Although a MIMO radar system can also include space time adaptive processing (STAP) techniques such as MUSIC [23] or ESPRIT [22], these techniques are not considered to allow for fair comparison between the two radars. The MIMO radar will use TDM waveforms to achieve orthogonality between RF channels and be capable of selecting which transmit/receive paths to process. Lastly, the processed radar returns must be saved in a format that allows them to be plotted for analysis. The specific radar settings that will be used for comparing the radar simulations are covered in Section 3.5.

3.2 Simulink Implementation

Beyond the base software program, MATLAB and Simulink provide products called toolboxes that deliver functions or blocks that are streamlined to make working in a particular research area faster and easier. The toolboxes required from MATLAB to run the simulations are the Phased Array System toolbox and the DSP System toolbox. The Phased Array toolbox provides MATLAB functions and Simulink block codes commonly used in radar and antennas, whereas the DSP System toolbox provides convenient signal processing functions. Other Simulink toolboxes used include the Antenna toolbox that provided additional antenna patterns, and the Instrument Control toolbox for the hardware integration that is discussed in Chapter 4. Details regarding the toolboxes can be found in [29].

The phased array and MIMO radar simulations use a common framework and differ only when required. Figure 3.1 depicts a high-level schematic of the Simulink-based radar simulations. The transmitter block simulates the transmitting waveform and amplifies the signal prior to transmission through free-space. The Tx and Rx arrays are ULAs consisting of six antenna elements each. The LOS Channel simulates the environment and two-way free space propagation loss for the radar signals from the Tx and Rx arrays to the targets. Sea clutter can also be simulated as part of the environment and thus it interfaces with the LOS channel block. The receivers amplify the received radar signal before matched filtering and beamforming. The signal processing block uses functions to improve the SNR of targets such as STC and coherent integration.

The radar systems were simulated using Simulink and MATLAB R2016b. A MATLAB function controls and manipulates all the settings for the simulated radars with the use of MATLAB's *assignin* function to create a base workspace called *ParamRadar*. Simulink performs the simulation through a model using the variables from the *ParamRadar* workspace and outputs the processed radar data back to MATLAB in the form of workspaces for subsequent analysis. The dashed-line components in Figure 3.1 are common features between the simulated phased array and MIMO radar systems. The components of Figure 3.1 and the differences required to implement them for the two systems will be discussed in the next several subsections.

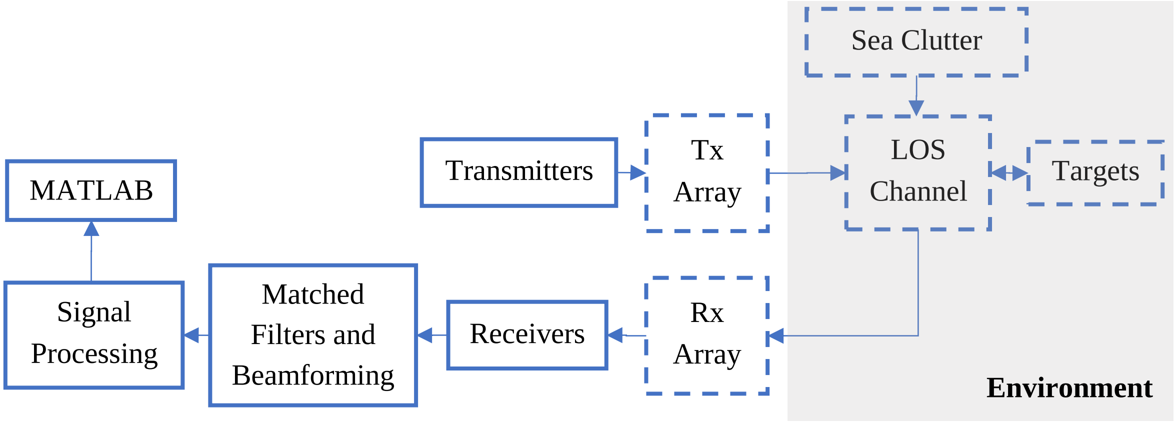

Figure 3.1 Generic schematic of a Simulink-based radar simulation

3.2.1 LOS Channel - Environment Simulation

The environment is simulated through MATLAB's Line-of-Sight (LOS) Channel block from the Phased Array toolbox. The block performs one-way propagation loss calculations from the transmitting antennas to multiple targets and then from the targets back to the receiving antennas. The LOS Channel blocks use a free-space propagation loss of $4\pi R^2$, where R is the range separating the antennas and the targets and models propagation time, Doppler shift as well as weather loss [29]. The LOS channel blocks are provided Cartesian location and velocity information of all targets and antennas every PRI so that the LOS channel block can perform its calculations. Target simulation and velocity updates are covered in Section 3.2.2.

As the phased array radar beamforms its signals using a single directed beam, only two LOS channel blocks are required to simulate the two-way LOS channel propagation delays, as depicted in Figure 3.2. The targets and sea clutter blocks are assigned Swerling model [10] RCS values whereas the Tx and Rx arrays simulate the antenna gains and beam patterns of the transmit and receive arrays, respectively. For a monostatic radar, the Tx and Rx arrays are placed at the same location with the same M elements.

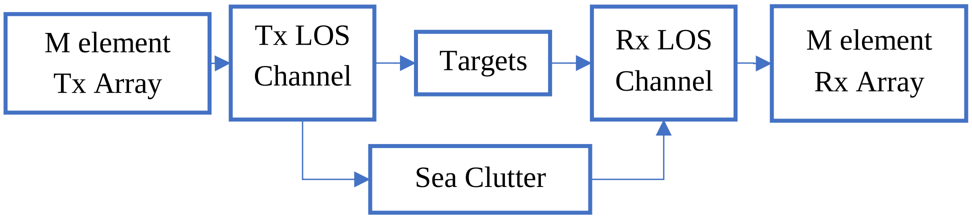

Figure 3.2 Phased array simulated environment

The MIMO radar simulation uses TDM to achieve orthogonality between transmitting waveforms. Because the MIMO radar is transmitting one element at a time, but receiving on all elements simultaneously, the channel path and propagation effects to each target and then back to each receiving antenna must be individually mapped. Therefore, additional LOS channel blocks are required to simulate the MIMO radar environment, which is depicted in Figure 3.3. Only one Tx LOS channel block is required for the simulations because the block is updated with a new transmitting element location every PRI, effectively creating a switch.

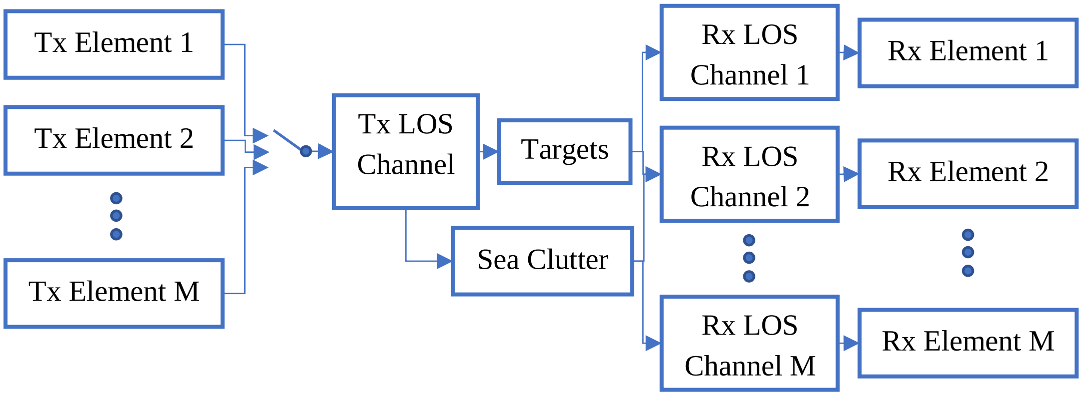

Figure 3.3 MIMO radar simulated environment

3.2.2 Target Simulation

Targets are simulated by defining their respective RCS, σ, at a location in Cartesian coordinates relative to the radar with an associated velocity vector. During the simulation, target locations and their respective aspect angles to the radar are updated based on their velocity vector at a refresh rate equal to the radar's PRF using Simulink's Platform block from the Phased Array toolbox. The Doppler shift induced on the return radar echo for moving targets is automatically calculated based on the relative radial velocity of the target to the radar. Speed, position, and aspect angles of targets are deterministic; however, the RCS of a target is not. RCS is defined as a measure of the reflective strength of a target and is the ratio of the power scattered to the incident power on a target from a specified angle [10]. Mathematically, RCS is defined as follows:

$$\sigma = \lim_{R\to\infty} 4\pi R^2 \frac{|E^{scat}|^2}{|E^{inc}|^2} \tag{3.1}$$

where E^{scat} is the scattered electric field and E^{inc} is the incident electric field at the target. RCS can be considered an effective area of a hypothetical isotropic radiator at the target's location that would produce the same echo return at the radar [30]. The RCS of a target is not static and will fluctuate depending on a variety of factors such as aspect angle, operating frequency, polarization, and target material. To model and account for these fluctuations, two different methods are used in the simulation.

A common and widely-accepted method to model RCS fluctuations are the four Swerling models [10]. Simulink's Target block from the Phased Array toolbox can simulate all four of the models and only requires an input of the target's average RCS. The Swerling models follow either an exponential or fourth degree chi-square PDF with the main differences between the four models being the degrees of freedom used in the PDF, how quickly the RCS of a target fluctuates, and if the target movement causes decorrelation. Table 3.1 [10] summarizes the four Swerling cases and when to use them. For simplicity, as the primary target of interest is a boat on the ocean, a Swerling I model was selected for the simulations in which a target's RCS fluctuates on a scan-to-scan basis following an exponential chi-square PDF [31].

Table 3.1 Swerling Models [9]

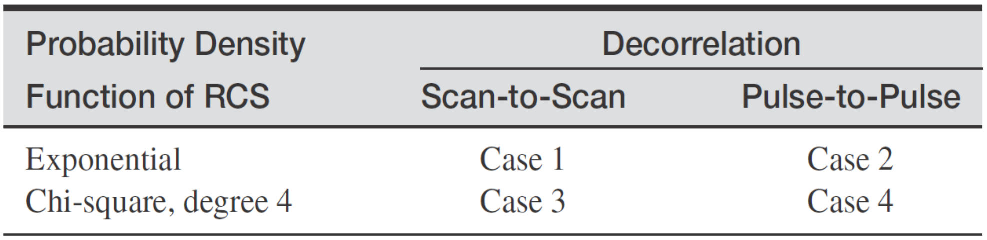

Probability Density Function of RCS	Decorrelation	
	Scan-to-Scan	Pulse-to-Pulse
Exponential	Case 1	Case 2
Chi-square, degree 4	Case 3	Case 4

The second method implemented to simulate a target uses Simulink's Backscatter Target block from the Phased Array toolbox. The Backscatter Target block allows the import of three dimensional RCS backscattering measurements for specific targets. The relative aspect angle in elevation and azimuth of the target to the radar is required to simulate the response using this method. These angles are fed into the block based on the target's position and velocity vector. Furthermore, similar to the Target block, the Backscatter Target block can apply Swerling models to the backscattering matrix. This method of target simulation was not used in the simulation analysis of the two radar systems, but was included for future consideration of performance measurements against specific targets.

3.2.3 Sea Clutter Simulation

As the primary target for detection is a boat on the ocean, there is a requirement for the simulation to include sea clutter models. The Naval Research Laboratory, Washingston, DC published an excellent report on various empirical sea clutter models in [32]. The report examines and compares the models with a recommended approach of their own through a series of MATLAB coded functions. The models predict the normalized radar cross section (NRCS), σ^o, for a given sea state based on the operating frequency, graze angle and polarization with some models also requiring wind direction. The relationship between the NRCS and the radar clutter cross section, σ_c, is defined as follows [16]:

$$\sigma^o = \frac{\sigma_c}{A_f} \tag{3.2}$$

where A_f is the effective area for a given beamwidth B, viewing the ocean surface at a range R, with a grazing angle φ, defined as [16]:

$$A_f = \frac{\pi(BR)^2}{4\sin\varphi} \tag{3.3}$$

The phased array radar simulation has a radiating beamwidth defined by (2.12) whereas the MIMO radar's radiating beamwidth is defined by the element pattern of the antenna, $E(\theta)$, where θ is the angle away from the broadside of the array. To simulate sea clutter, the proposed method from [32] was used to calculate σ^o for all simulated ranges and angles. The results of the calculations for σ^o were then normally distributed to create a matrix of sea clutter RCS values for every range bin at all scan angles. The sea clutter RCS positions are then uniformly distributed in height based on the sea state of the simulation. Sea state wave heights are defined and outlined in Table 3.2 [33].

The simulations consider sea clutter as targets with an associated RCS using Simulink's Target block, which performs the same calculations as a normal target with a Swerling model described in the previous sub-section. Implementing sea clutter greatly increases the simulation time due to the number of radar returns and the associated transmit/receive paths that are required to be computed in the LOS Channel blocks.

Table 3.2 World Meteorological Organization’s codes for sea state [33]

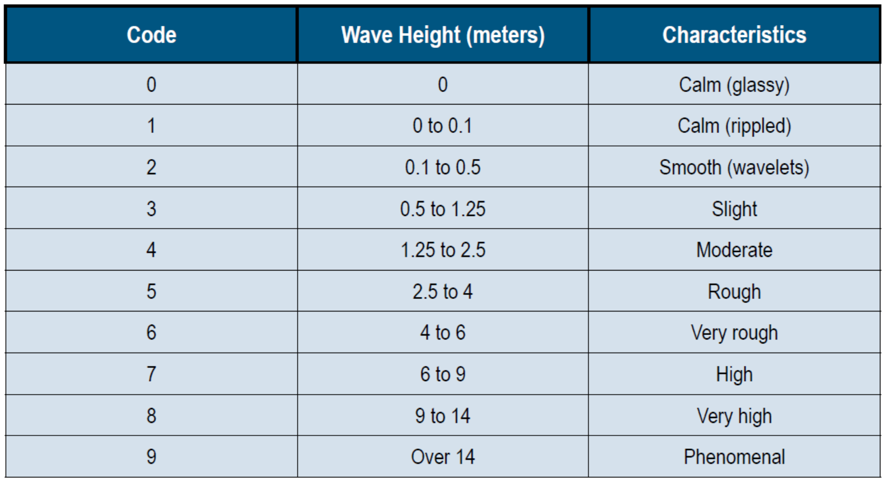

Code	Wave Height (meters)	Characteristics
0	0	Calm (glassy)
1	0 to 0.1	Calm (rippled)
2	0.1 to 0.5	Smooth (wavelets)
3	0.5 to 1.25	Slight
4	1.25 to 2.5	Moderate
5	2.5 to 4	Rough
6	4 to 6	Very rough
7	6 to 9	High
8	9 to 14	Very high
9	Over 14	Phenomenal

3.2.4 Antenna and Array Simulation

Antennas and arrays are simulated using Simulink’s Narrowband Tx and Rx Array blocks from the Phased Array toolbox. The Simulink blocks use MATLAB expressions from the *ParamRadar* workspace to define the parameters of the ULA or the antennas being simulated. The MATLAB function used to create a ULA is *phased.ULA* while the functions listed in Table 3.3 [29] outline the available antennas for simulation using the Phased Array toolbox. Other antenna types, such as microstrip or feedhorns, can be simulated using the Antenna toolbox; however, if the antenna pattern is known, it can be imported to MATLAB and simulated using the *phased.CustomAntennaElement* function from the Phased Array toolbox.

Table 3.3 Antennas available for Simulation using MATLAB’s Phased Array toolbox

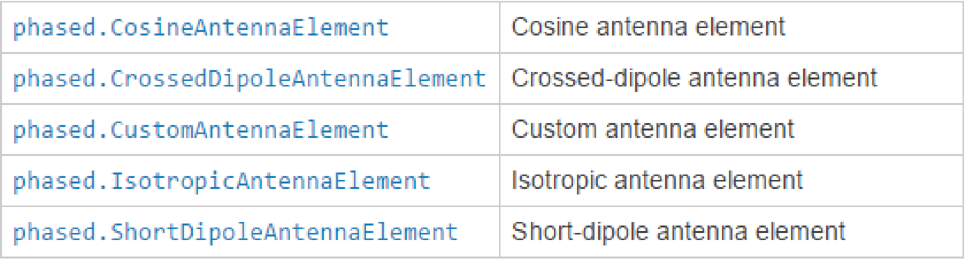

`phased.CosineAntennaElement`	Cosine antenna element
`phased.CrossedDipoleAntennaElement`	Crossed-dipole antenna element
`phased.CustomAntennaElement`	Custom antenna element
`phased.IsotropicAntennaElement`	Isotropic antenna element
`phased.ShortDipoleAntennaElement`	Short-dipole antenna element

When simulating antenna elements, MATLAB will provide a full three-dimensional radiation pattern that accounts for antenna polarization and frequency. An example of a radiation pattern for a short z-oriented dipole antenna is found in Figures 3.4 and 3.5 using MATLAB’s *pattern* function.

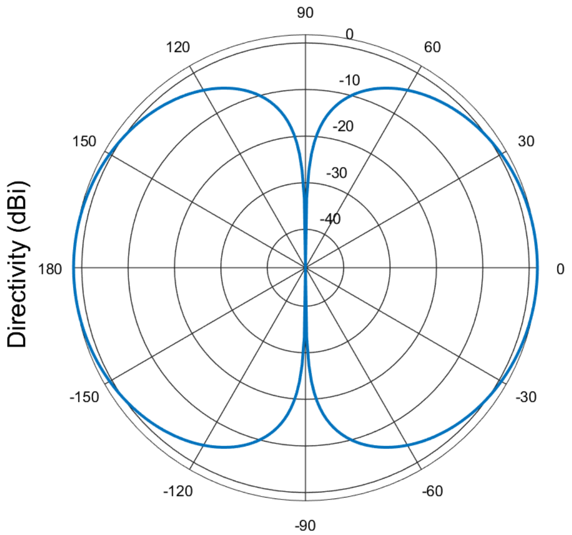

Figure 3.4 E-Plane cut of a simulated short dipole antenna

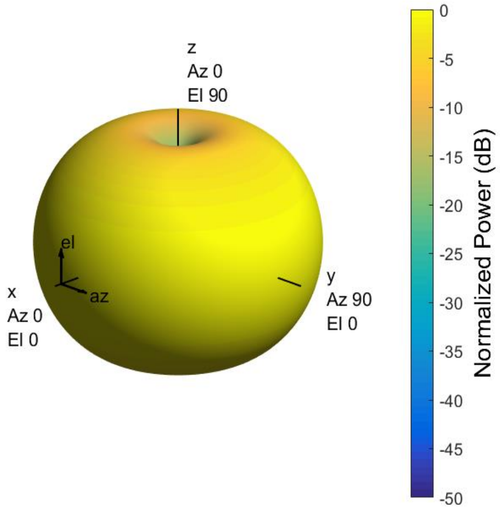

Figure 3.5 Radiation pattern for a simulated short dipole antenna

The difference between the phased array and MIMO radar simulations with respect to antenna placement is that the phased array will simulate a ULA using *phased.ULA* whereas the MIMO radar will simulate individual elements. The ULA is formed from a uniform distribution of one of the antennas selected from Table 3.3 whereas MIMO will map individual elements to specific locations and then use (2.10) to form a virtual array for subsequent processing. Figure 3.6 serves as an example of applying (2.12) to form a simulated one-way radiation pattern of a ULA with six short z-oriented dipole antennas uniformly separated by half of a wavelength. A monostatic configuration of six transmitting and receiving elements with half of a wavelength separation in the y-axis between each element is used for all simulations. The antennas and arrays are simulated under ideal conditions which do not account for mutual coupling between elements.

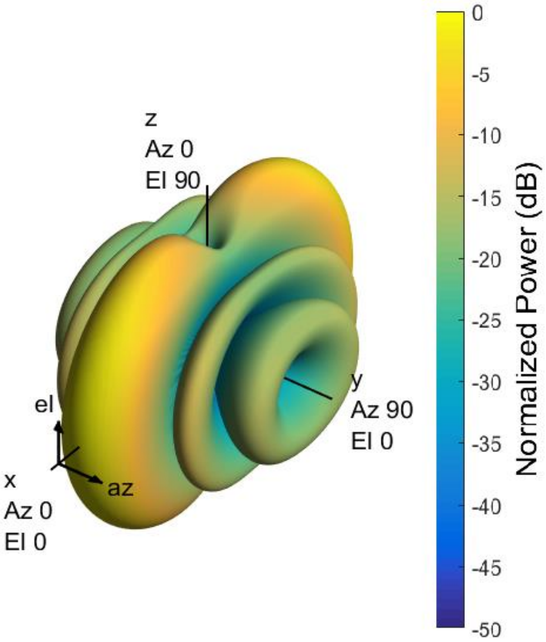

Figure 3.6 Radiation pattern for a simulated six element ULA

3.3 Phased Array Radar Simulation

This section will provide details regarding the phased array radar simulation only. The transmitter and receiver components will be reviewed, followed by a discussion on the application of signal processing techniques used to improve the SNR for target detection and estimation.

3.3.1 Phased Array Transmitter

The phased array radar transmitter has two main components: a waveform generator and an amplifier. The purpose of the waveform generator is to create one of MATLAB's various pulse waveforms listed in Table 3.4 as a baseband signal. The shape of the waveform is defined by the pulse width and the type of waveform selected, which in turn will define the amplitude and phase information of the transmitting signal. As the transmitting signal is being simulated digitally, the output of the waveform generator is discrete and the number of samples taken over the PW of the transmitting signal is defined by the sampling frequency of the model. The phased array radar simulation runs in intervals of PRI, so the output of waveform generator will consist of an entire pulse train for the radar. The waveform of the transmitting signal of duration PW, will form the first portion of the output of the waveform block, which will then be followed by a series of zeros to simulate the listening time of the receiver to account for a full PRI. All of the waveforms from Table 3.4 were simulated in a phased array simulation; however, as previously mentioned, a phase-coded Zadoff-Chu pulse compression pulse was selected as the primary waveform for further analysis.

Table 3.4 Available pulse waveforms for simulation

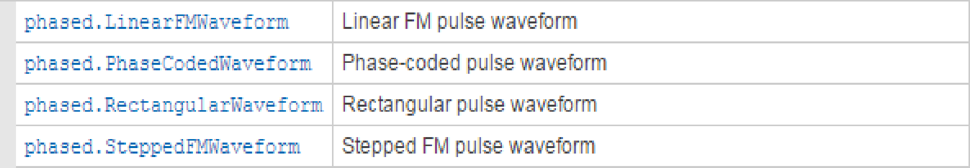

`phased.LinearFMWaveform`	Linear FM pulse waveform
`phased.PhaseCodedWaveform`	Phase-coded pulse waveform
`phased.RectangularWaveform`	Rectangular pulse waveform
`phased.SteppedFMWaveform`	Stepped FM pulse waveform

Figure 3.7 is a high-level Simulink representation of the phased array radar's transmitter and its connection to the ULA consisting of *P* samples in time (or range) for *T* simulated targets. The phase-coded waveform generator sends its baseband signal to Simulink's transmitter block, which amplifies the baseband signal based on its peak power and associated transmitter gain. The transmitter outputs two signals: the amplified baseband signal and a transmitter status signal that is sent to the receiver for coherence and synchronization. The power of the transmitted signal is split evenly among the number of elements of the ULA in the Narrowband Tx Array block. Finally, the Narrowband Tx Array will apply phase steering weights

following (2.24) to the individual signals at each element prior to transmission to electrically steer the beam to a desired azimuth angle. Conversion from baseband to the operating frequency in the transmitter does not occur in Simulink as it would for a real radar. Simulink uses the operating frequency to calculate signal path loss, account for antenna gains, as well as any environmental or Doppler effects in the LOS Channel environmental blocks and then applies these effects to the baseband signal prior to reception. All processing is performed at baseband.

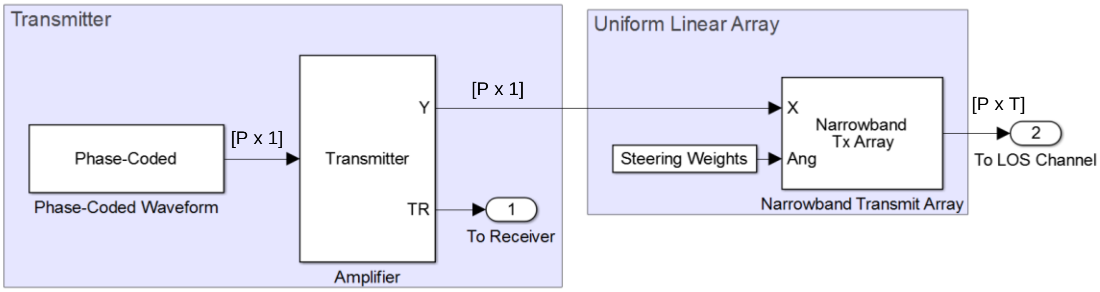

Figure 3.7 Transmitter for phased array radar simulation

3.3.2 Phased Array Receiver

The receiver's main function is to receive the incoming signal and then amplify it for subsequent processing. Amplification is required to account for the travel loss of the signal to and from the target. A high-level overview of the receiver is provided in Figure 3.8 consisting of P samples in time (or range) for T simulated targets and a 6-element ULA. The return echoes from the targets are received at the ULA from a LOS channel block and the Narrowband Rx applies the gain from the element pattern from (2.12) based on the relative angle of the target to the array. The received signal from each antenna in the ULA is then amplified by the receiver preamp block with a user-specified gain. The receiver preamp will also simulate receiver noise based on a user-defined loss factor, reference temperature and noise figure from (2.15).

STC is used after the receiver preamp to attenuate received signals in closer proximity of the radar. Because the return echo loss is proportional to the inverse of R^4, there is significantly less propagation loss for return echoes from targets or clutter that are close to the radar. If STC is not implemented, returns from noise such as sea clutter will increase the number of false targets in close proximity to the radar [16]. The STC implemented follows the R^4 attenuation curve depicted in Figure 3.9.

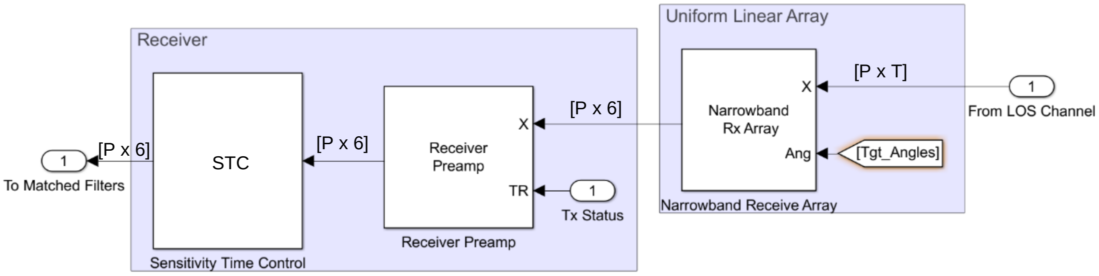

Figure 3.8 Receiver for phased array radar simulation

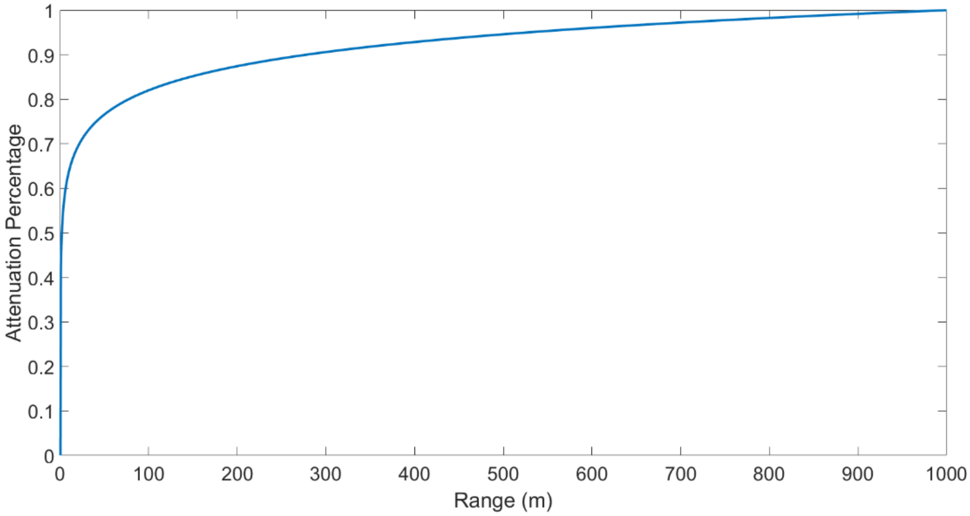

Figure 3.9 STC attenuation of received radar signal

3.3.3 Phased Array Signal Processing

Signal processing of the radar return echo is required to detect and estimate the location of a target. A high-level overview of the processing used in the phased array radar is depicted in Figure 3.10 consisting of *P* samples in time received from a 6-element ULA. The phase shift beamformer, coherent pulse integrator and CFAR

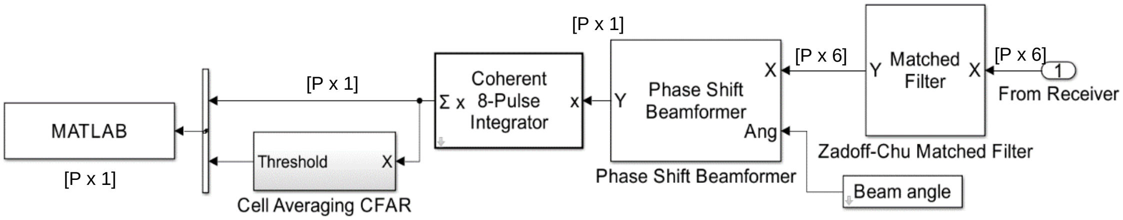

Figure 3.10 Phased array signal processing scheme

detector apply the theory outlined in Chapter 2. The matched filter is a Finite Impulse Response (FIR) operation that performs a cross correlation of the received signal with the time reversed samples of the transmitted signal to maximize the SNR. Specifically, the output of the matched filter, $y[p]$, shall equal [10]:

$$y[p] = s[p]x[P + 1 - p] \tag{3.4}$$

where $s[p]$ is the sampled received signal consisting of $x[p]$, the ideal return signal, and any receiver noise for p=1 to P where P is the total number of samples. Although windowing was not applied for analysis, the matched filter Simulink block can apply windowing functions such as Hamming or Chebyshev [29]. In general, windowing is a method to improve the dynamic range of the radar by applying a different shape to the matched filter instead of a rectangle. Changing the window type will lower the side lobes of the sinc response of the matched filter thus increasing the ability to detect signals with lower amplitudes. This, however, comes at a cost of resolution because the width of the main lobe is increased.

As slow moving surface targets are being examined in this thesis and the number of coherent integrations will be restricted following (2.19), Doppler processing was not included in the simulation. If desired, Doppler processing could be implemented with the coherent integrator in Figure 3.10. For instance, a DFT could be taken for each range cell and could be used as a replacement for the coherent integrator by setting a threshold for a response in the frequency domain. A target return with zero Doppler will appear as a DC signal while any target with a constant velocity over the CPI will create a sinc response at its associated f_d. The DFT is superior to the coherent integrator in that it is not restricted by (2.19). The spacing, or resolution of the DFT, Δf_{RES}, is defined as follows:

$$\Delta f_{RES} = \frac{PRF}{N} \tag{3.5}$$

where PRF is constant over the CPI and N is the number of integrations, or samples, used in the DFT. This means that if a DFT is used for Doppler processing, then a designer must balance between Δf_{RES}, blind speeds, CPI and the maximum unambiguous range of the radar.

Lastly, a matrix of the detection threshold values from the cell averaging CFAR detector and the output of the coherent integrator are sent to MATLAB as workspaces for plotting and analysis. Section 3.5 provides an in-depth analysis and comparison of both simulated radar systems for a variety of scenarios.

3.4 MIMO Radar Simulation

This section will provide high-level design details of the MIMO radar simulation and will focus on the differences between it and the phased array radar simulation. The transmitter and receiver components will be reviewed, followed by a discussion on the formation of the virtual array and the signal processing techniques.

3.4.1 MIMO Radar Transmitter

Figure 3.11 depicts a high-level overview of the MIMO radar transmitters and their interfaces to the radiating antenna elements consisting of P samples in time for T simulated targets. Many additional connections exist in the actual simulation, but they are not shown for clarity. Given that TDM with a Zadoff-Chu phase-encoded waveform is being used to achieve orthogonality, a transmit selector is used to switch to the active transmitter every PRI. The individual transmitter blocks each contain a waveform generator and an amplifier similar to the phased array radar simulation. Each transmitter is individually fed to a Narrowband Tx Array block that is simulating a single radiating antenna element. The combination of all Narrowband Tx Array blocks form the same ULA configuration as the phased array simulation. The output from the antennas accounts for the element factor, $E(\theta)$, just like the phased array simulation, and are sent through a series of LOS channel blocks for simulating transmission through the environment. Of note, if a specific antenna element is not transmitting, the Tx Selector ensures that the output from the associated transmitter is set to zero. Lastly, *Ang* 1 through 6 of Figure 3.11 provides the relative azimuth and elevation angles of the T targets to each radiating element so that Simulink can account for the antenna gain from the element pattern for each transmission path.

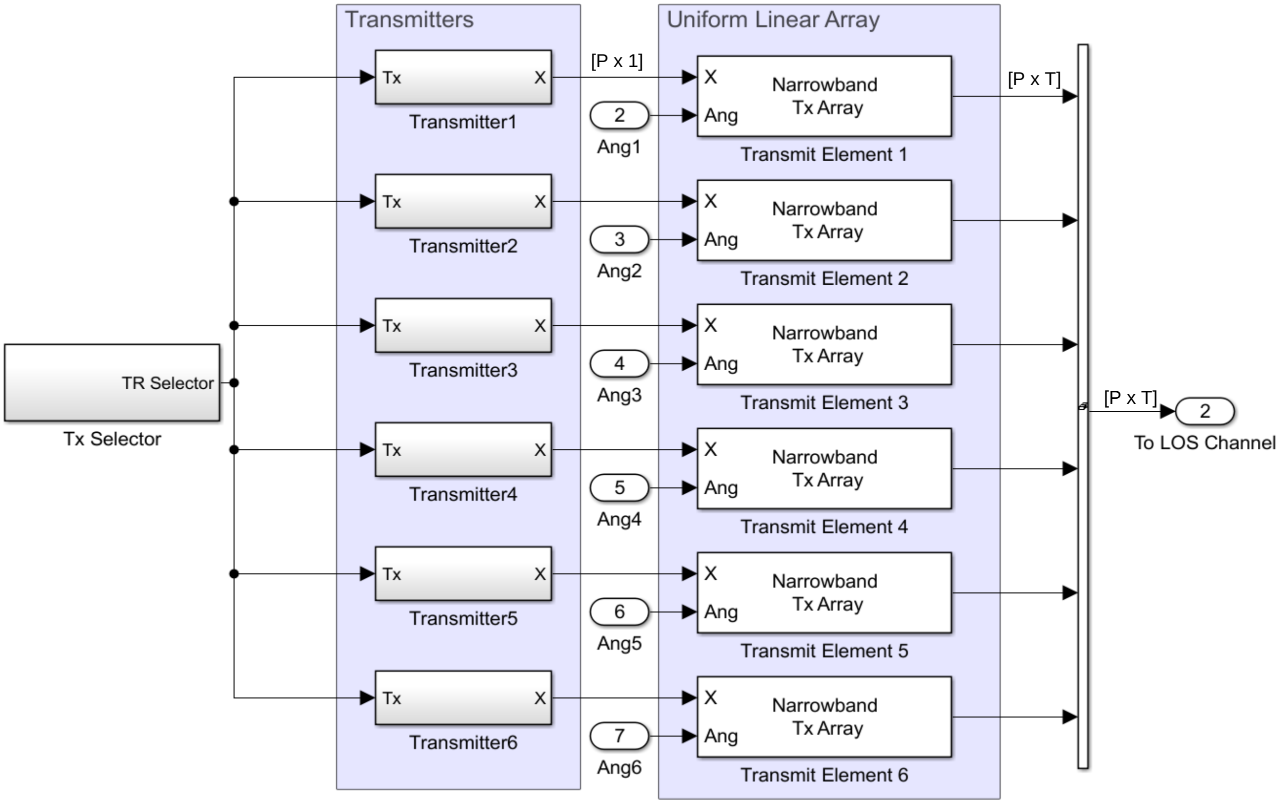

Figure 3.11 High-level design for a 6-element MIMO radar transmitter

3.4.2 MIMO Radar Receiver and the Virtual Array

Figure 3.12 depicts a high-level overview of the simulated MIMO receiver consisting of *P* samples in time for *T* simulated targets. Similar to the transmitting side of the MIMO radar simulation, individual Narrowband Rx Array blocks are used to act as individual antennas to form an array. Each receive antenna is fed from a series of LOS Channel blocks simulating the return path from each target. Every antenna is connected to a dedicated receiver that will amplify the signal followed by the same STC processing used in the phased array radar simulation to attenuate the signal based on range.

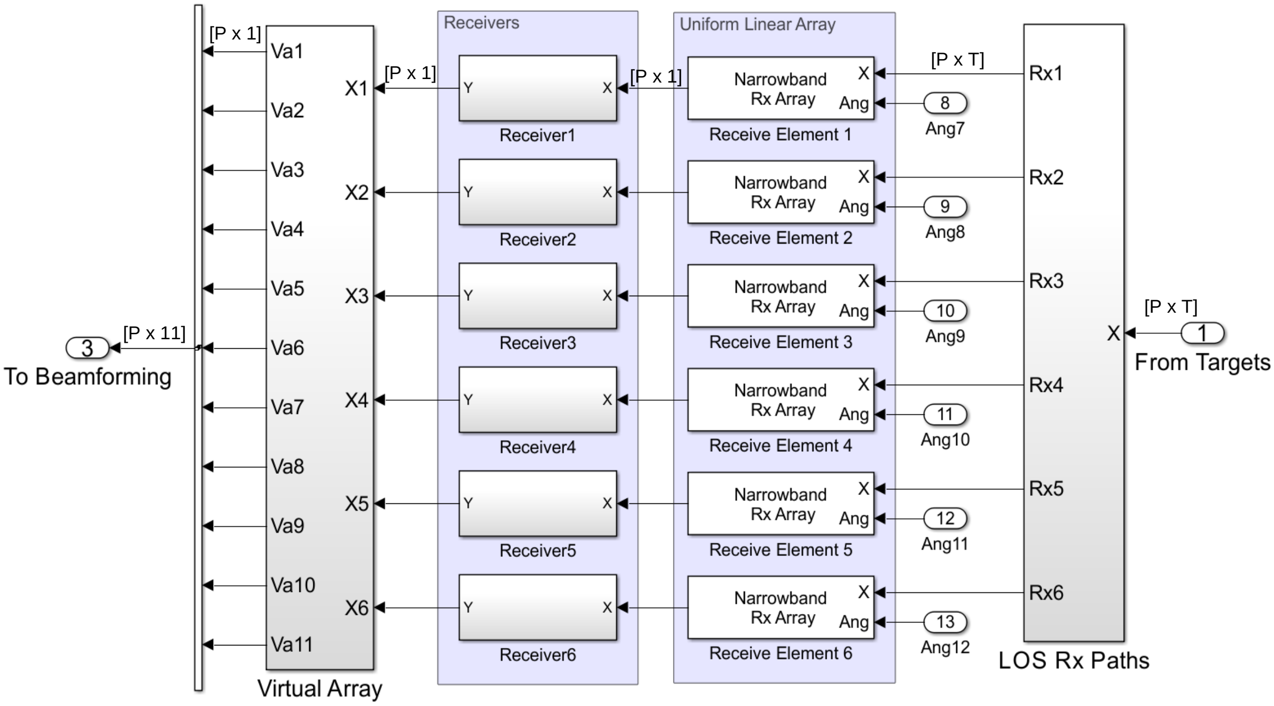

Figure 3.12 High-level design for a 6-element MIMO radar receiver

After the receiver has amplified the signals, they are sent to the virtual array block to associate a received signal from a real antenna to a virtual element. The virtual array of the MIMO radar is formed in several steps. Firstly, as TDM is being used to create orthogonality between transmitting waveforms, there is no cross correlation between transmissions and the same waveform is being transmitted across all transmitters at different times. Therefore, only a single matched filter is required for each virtual element for TDM. If simultaneously M transmitted orthogonal waveforms were used, M matched filters would be required.

As there is no risk of cross correlation between transmitting waveforms by using TDM, the received signals from individual elements can be mapped directly to a virtual element following (2.10). Since six elements are being used in the MIMO radar simulation, the minimum CPI to create a virtual array when using TDM is 6 x (PRI). Using a 6-element ULA in a monostatic scheme and using the spatial convolution from (2.10), the received signals will be mapped to virtual elements following the logic rules found in Table 3.6. The result is an 11-element virtual array that will have an identical two-way pattern as the phased array radar's 6-element array. The virtual array buffers the returns for six PRI intervals and then performs a summation of the returns in slow time across each virtual element to form the virtual array. Lastly, the MIMO radar is able to select which transmitters and receivers are to be used during a simulation. Changing the number of transmitters will adjust the minimum CPI to form the virtual array and change the array weights found in Table 3.6 effectively changing the beam pattern. MIMO beam pattern analysis for different configurations is provided in Chapter 4.

Table 3.5 Virtual Array logic for MIMO radar simulation

Transmitting Element	**Receiving Elements**										
Tx 1	Rx 1	Rx 2	Rx 3	Rx 4	Rx 5	Rx 6					
Tx 2		Rx 1	Rx 2	Rx 3	Rx 4	Rx 5	Rx 6				
Tx 3			Rx 1	Rx 2	Rx 3	Rx 4	Rx 5	Rx 6			
Tx 4				Rx 1	Rx 2	Rx 3	Rx 4	Rx 5	Rx 6		
Tx 5					Rx 1	Rx 2	Rx 3	Rx 4	Rx 5	Rx 6	
Tx 6						Rx 1	Rx 2	Rx 3	Rx 4	Rx 5	Rx 6
Virtual Array Weights	**1**	**2**	**3**	**4**	**5**	**6**	**5**	**4**	**3**	**2**	**1**

3.4.3 MIMO Signal Processing

The MIMO radar signal processor uses the same processing techniques used in the phased array radar, but with some notable differences. The high-level architecture of the signal processing techniques used in the MIMO radar is depicted in Figure 3.13 consisting of *P* samples in time and *S* scan angles using 11 virtual elements. Although this thesis did not explore high-resolution beamforming techniques such as MUSIC or ESPRIT, a Root MUSIC DOA Simulink block [29] is included in Figure 3.13 to demonstrate where it could be implemented in the simulation. Instead of using a 6-element ULA as a reference like the phased array radar, the phase shift beamformer block in the MIMO simulation uses the virtual array with appropriate element weights as a reference to perform beamforming. The virtual array can take on any user-defined form using up to six transmit and six receive elements. Most importantly, as MIMO radar has enough data to scan an entire area once the virtual array is formed, steering or scanning at different angles can be done in parallel with a phase shift beamformer Simulink block. However, for the flexibility of changing search areas, the MIMO radar simulation uses an Unbuffer block to process the radar returns at one scan angle at a time. After coherent integration and using a cell-averaging CFAR detector, the processed MIMO radar returns are sent to MATLAB as workspaces for plotting and analysis.

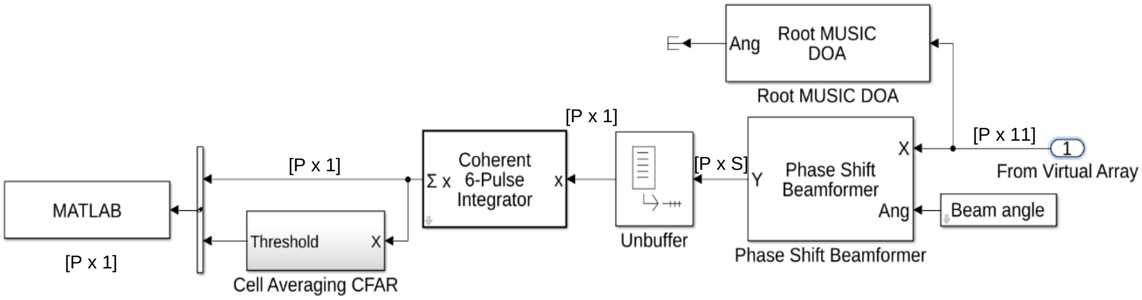

Figure 3.13 Basic MIMO signal processing scheme

3.5 Simulation Results

This section will review and compare multiple scenarios using both the MIMO and phased array radar simulations in an effort to determine which radar system is better suited for target detection. References such as [2,4,19,29] provide some excellent theoretical comparisons between the two radar systems; however, no references were found where full end-to-end radar systems were simulated in scenario-based settings focused on an application. The simulations in this section will focus on the detection of stationary or slow moving boats on the ocean in a variety of scenarios so comparisons between the two radar systems can be made. There are many factors that can be compared between the two radar systems such as: range resolution of the transmitting waveform, angular resolution of the radar beam, the radar's CPI, scan rate, minimum SNR detection, and Doppler effects on detection. These factors will be discussed and compared over a series of scenarios.

3.5.1 Simulated Radar Settings

To maintain consistency across scenarios, it is important to keep as many radar parameters as possible constant. Although some of the parameters could be adjusted to improve the detection capabilities of the radar, this is beyond the scope of this thesis, as adjusting various radar settings introduces too many metrics to measure. The radar settings for the simulations are outlined in Table 3.6 and were selected based on a naval ship using a radar to detect surface targets. Any deviations from the radar settings in Table 3.6 for a specific scenario will be highlighted prior to any discussion. The base of the ULA of the radar is the center of reference for all experiments. The ULA is placed at a height of 5 m so it will have the following Cartesian coordinates during simulations of [0, 0, 5]. The radar platform can move during the simulation based on a velocity vector, but remains stationary for all simulations. The assumption being made is that an onboard Inertial Navigation System (INS) combined with a Global Positioning System (GPS) like what is found onboard a modernized HALIFAX class frigate would be used by the radar system to calibrate roll, pitch, and yaw movements as well as any accelerations measured along those axes. Simulated targets will be placed or move with a velocity relative to the position of the ULA. All targets are placed on the surface of the ocean at a height based on the sea state or at zero if sea clutter is not being simulated.

Table 3.6 Simulation Radar Settings

Radar Setting	Value
Radar Type	Coherent 2D Pulsed
Operating Frequency	1.5 GHz
Total peak transmitting power	100 W
Antenna Configuration	6-element ULA – $\lambda/2$ spacing
Antenna type	Microstrip patch (See Section 4.3)
Simulation Sample Rate	120 MHz
Sector Search (Az only)	$\pm 40^o$ (80^o total)
Receiver Gain	20 dB
Max Unambiguous Range	10 km
PRI	66.7 µs
PRF	15 kHz
Uncompressed PW	166 ns
MIMO Orthogonality type	TDM
Waveform	Zadoff-Chu
Pulse compression ratio	4
Compressed range resolution	6.25 m
Receiver noise figure	3 dB
Loss factor	3 dB
Environmental Temperature	15^oC
Atmospheric pressure	1 atm
Water Vapour Density	7.5 g / m^3
CFAR – P_{FA}	0.001
CFAR - P_D	0.95

3.5.2 Single Stationary Target

For the first experiment, a single stationary Swerling I target with σ = 0.8 m^2 is placed at a range of 500 m at 0^o azimuth without sea clutter. The aim of this test is to verify the MIMO and phased array two-way radiation patterns with the theoretical pattern. If the MIMO radar uses all six transmitters and receivers to form its corresponding virtual array, then the two-way radiation patterns of the two radars should be the same [15]. Using (2.10), the virtual array weights of the MIMO radar with half wavelength spacing will be [1 2 3 4 5 6 5 4 3 2 1].

While the processed radiation patterns will match, the amount of energy physically reflecting off the target will not unless the MIMO radar integrates additional returns. As discussed in Chapter 2, the MIMO radar requires additional returns over a CPI to match the equivalent SNR of a phased array. The factor by which a MIMO radar must increase its CPI over a phased array is based on the number of transmitting elements, which is six for the simulations. Therefore, the MIMO radar simulation requires to coherently integrate six times the integration factor of the phased array radar simulation. For simplicity, the phased array radar only processes a single return from each scan angle, therefore the MIMO radar requires to perform six coherent integrations to match the SNR of the phased array. However, this increase to the CPI assumes simultaneous orthogonal transmissions from the MIMO radar. As the MIMO radar simulation is using TDM to achieve orthogonality, the CPI interval requires to be increased again by a factor of the number of transmitters. Therefore, the MIMO radar simulation performs integrations over a total time of 36(PRI), or 2.4 ms, whereas the phased array radar only requires a single PRI of 66.7 µs. Further discussion on CPI and its effects is found in Section 3.5.4 for a scenario of multiple moving targets.

Using the integration settings just described, the radar returns from a single stationary target for the two radars are equivalent. This is expected as the signal processing used for both radar systems is identical. The radar return of the phased array radar is plotted in Figure 3.14. Returns are only plotted out to 2 km where the target return can be easily observed. The sidelobes of the return are observed as well as the response from the Zadoff-Chu matched filter.

Comparing the integrated return after the output of the phase-shift beamformer of both radar systems at a range of 500 m will provide a comparison of the two radiation patterns. As the MIMO radar is performing 36 coherent integrations to a single return of the phased array, the normalized power output

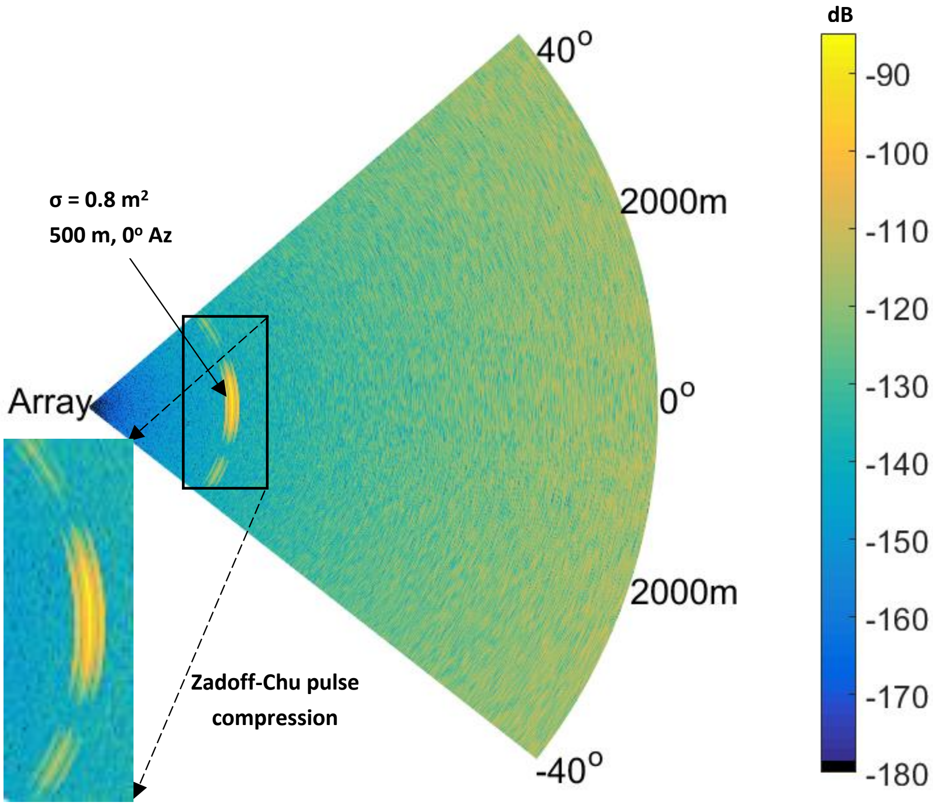

Figure 3.14 Radar plot of the phased array radar simulation with a single stationary target

should be equivalent. Furthermore, as the target and radar platform are stationary, there are no Doppler effects that will negatively impact the MIMO radar's coherent integration. The normalized radar returns of the target at 500 m of both radar systems as well as a reference to the theoretical two-way pattern is provided in Figure 3.15. As it can be seen, the returns from both radar systems follow the theoretical curve and are comparable to one another.

The second experiment conducted with a single target was to verify the beam steering capability of the two radar systems and to verify the two-way radiation pattern response for a target off boresight. The same target was moved to a range of 515 m at a relative bearing of 13.5° azimuth to the radar. All other radar settings, including integration numbers, remained unchanged. Once again, comparable results were achieved between the two radar simulations that agree with the two-way theoretical beam pattern. Figure 3.16 demonstrates the angular radar return from the target while Figure 3.17 shows the radar plot of the return signals of the MIMO radar simulation out to a range of 2 km. The target is again easily detected above the noise. The theoretical curves are the two-way antenna patterns derived from (2.13) or (2.14) and use (2.26) when beam steering.

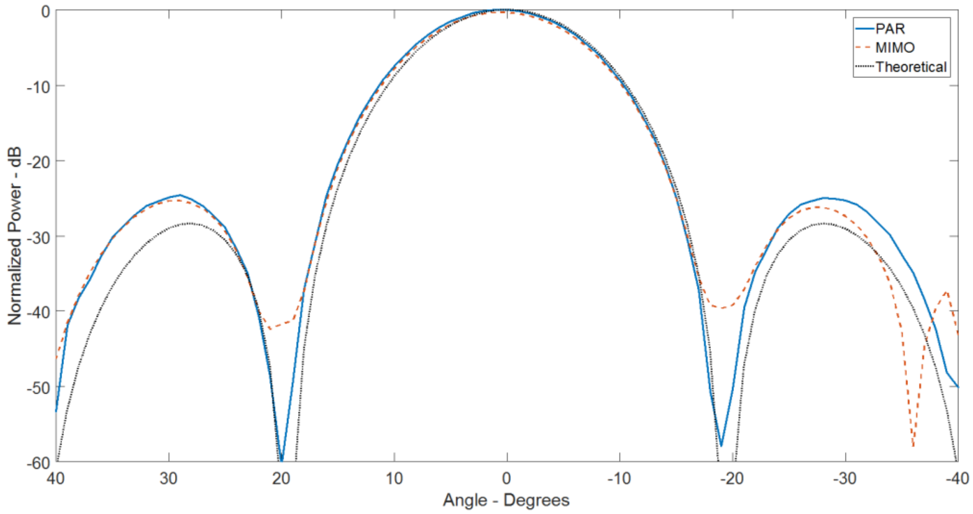

Figure 3.15 Phased array and MIMO radar azimuth comparison of a stationary target

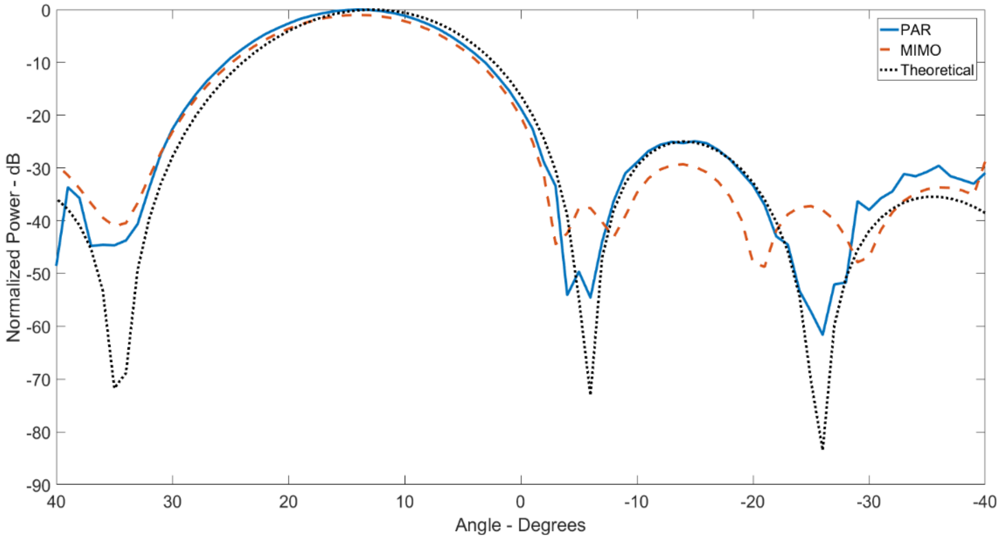

Figure 3.16 Phased array and MIMO radar azimuth comparison of a target at 13.5°

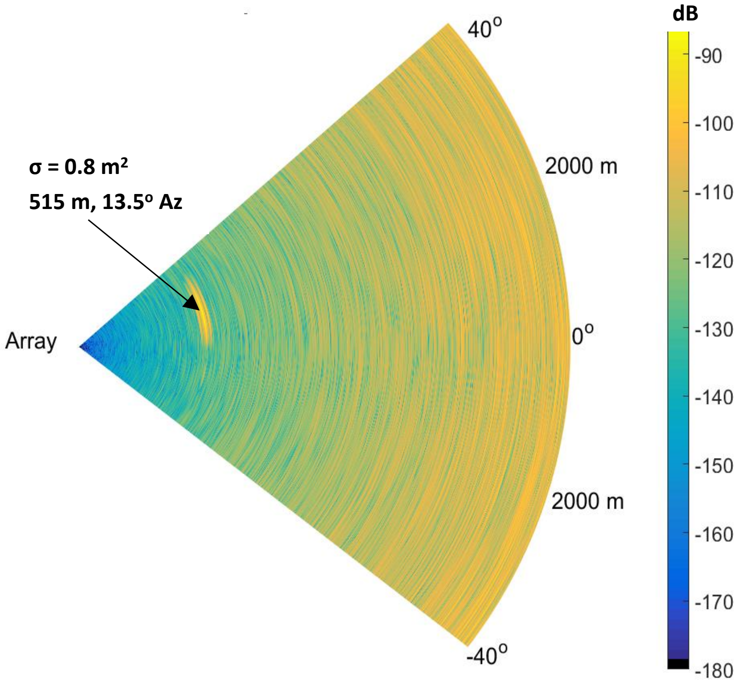

Figure 3.17 Radar plot of the MIMO radar simulation with a target at 13.5°

3.5.3 Single Moving Target

It was just demonstrated that a MIMO and phased array radar will have the equivalent two-way beam pattern and return power from a target using a monostatic antenna scheme. This statement is true so long as the MIMO radar increases its CPI and uses all available virtual elements. Although the scenario presented in the previous section is useful to verify theory, it is not practical in an operational setting where a ship and the targets it is trying to detect are moving. This subsection will explore the effect that Doppler will have on the MIMO's radar SNR and its ability to detect a target.

One of the major disadvantages of MIMO is that it requires a longer CPI than a phased array radar to achieve the same SNR for a radar plot. As described in Chapter 2, a moving target with radial speed will create a Doppler shift on the radar return echo. If the Doppler shift is left uncompensated, then there will be a loss in signal gain during the coherent integration process. There are several ways to measure and compensate for Doppler such as a series of DFTs [34], but this adds significantly more processing and filters, especially in the case where simultaneous orthogonal waveforms are being used where DFT processing would be required for each orthogonal matched filter [4].

The aim of the experiments conducted in this sub-section is to highlight the significance of the Doppler loss of a moving target to determine if MIMO radar can be used to detect approaching ships travelling at 30 knots, or approximately 15 m/s, without the use of Doppler processing. In the example from the previous sub-section, the MIMO radar conducted 36 coherent integrations to match the SNR of one return from the phased array. For uncompensated Doppler shifted radar returns, more than 36 integrations will be required for the MIMO radar to maintain the same SNR as the phased array radar. The amount of signal loss from Doppler during the CPI of the MIMO radar follows Figure 2.7. Using the coherent integration restriction of (2.19) for a 4 dB loss on coherent integration over a CPI with M = 36, the maximum relative radial speed of a moving target with the radar settings outlined in Table 3.6 will be $v_r = 20.8$ m/s. Therefore, assuming again that the MIMO radar platform has an INS compensating for its own movement, the MIMO radar in this scenario will detect a target travelling at 20.8 m/s at 4 dB less power than a phased array. It is important to highlight that for the same number of integrations, but with an X-band radar operating at 9.5 GHz, the maximum radial velocity of a target with a 4 dB integration loss is 3.3 m/s. Therefore, a MIMO radar system not compensating for Doppler should operate in the L-band.

A 4 dB loss in power is acceptable for a high SNR environment, but may not be realistic in noisy or cluttered environments. If additional integrations are required to detect a target, then there are several options or restrictions that must be applied. Either it is accepted that targets travelling at specific speeds will not be able to be detected in specific environments or some form of Doppler compensating techniques will be required to be introduced into the radar's processing. An analysis of Doppler effects in different SNR environments is outside the scope of this thesis. To illustrate the effect of Doppler on the returns of both radar systems, a non-fluctuating target with $\sigma = 0.8\ \text{m}^2$ was placed at a range of 1 km at 0° azimuth at different speeds. A Swerling model is not used as a target model in this experiment to minimize the variables that will affect the radar return.

To demonstrate the negative effect of Doppler on a MIMO radar, the target was given an approaching speed of 41.6 m/s. A radial speed of 41.6 m/s with the radar specifications of Table 3.6 will place the coherent integration of 36 returns of the MIMO radar into a null of Figure 2.7. In other words, the coherent integrator will destroy the received radar signal. The three-dimensional radar picture of the phased array with a CFAR threshold is shown in Figure 3.18 while the same radar picture for the MIMO radar is shown in Figure 3.19. As it can be observed from these two figures, the phased array radar can detect the target against the CFAR threshold while the MIMO radar cannot. A comparison plot in azimuth at a range of 1 km is provided in Figure 3.20 demonstrating the differences in the returns of the two radar systems. As expected, there is no visible radar return from the target for the MIMO radar.

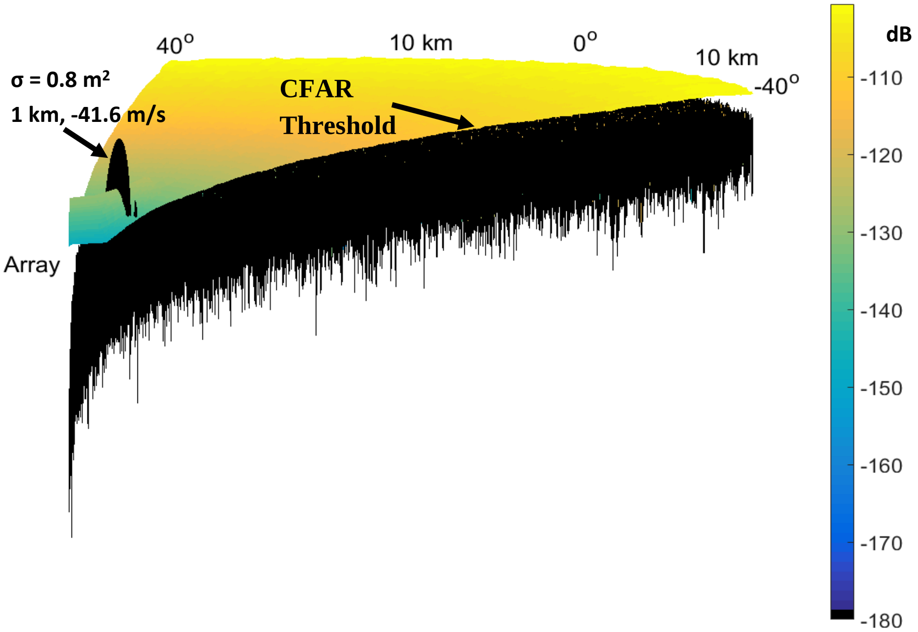

Figure 3.18 Phased array radar response for a target travelling at -41.6 m/s

Figure 3.20 shows that a MIMO radar is more susceptible to Doppler than a phased array radar. The results shown are for the specific scenario with the radar settings outlined in Table 3.6 and will vary if parameters such as PRI or the radar's operating frequency are changed. Both extremes have been demonstrated so far: a comparison of the two radar systems with an example without Doppler and an example where Doppler destroys the return of the target preventing the MIMO radar from detecting it. The next experiment will demonstrate how Doppler impacts the MIMO radar for various approaching velocities with a comparison to the phased array radar.

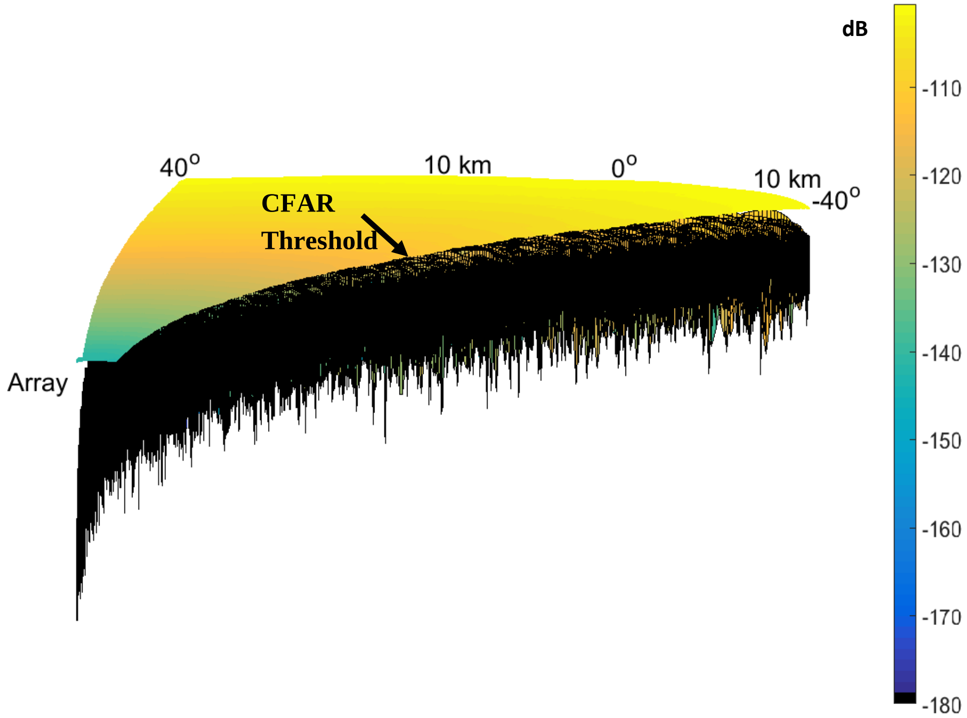

Figure 3.19 MIMO radar response for a target travelling at -41.6 m/s

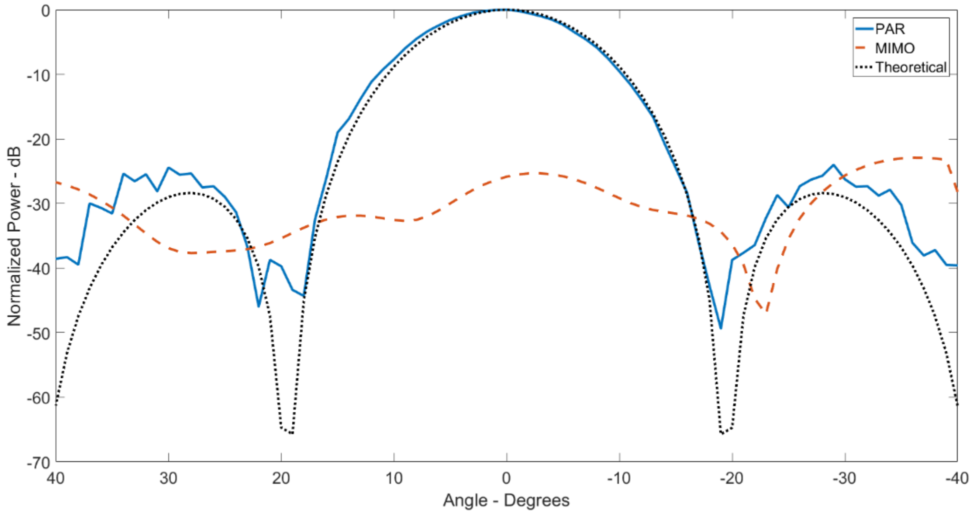

Figure 3.20 Phased array and MIMO radar azimuth comparison of a target at 1 km approaching at 41.6 m/s

Before presenting the results, a few signal processing points must be discussed. Firstly, the Doppler loss from Figure 2.7 and the restriction from (2.19) cannot be universally applied to MIMO, especially while using TDM waveforms. This is because the virtual array elements do not maintain a consistent sampling interval. For instance, referring to Table 3.6, the center virtual element of the MIMO radar simulation has a weight of six, meaning that every transmitting element will provide an update to this virtual element every PRI. Conversely, the second virtual element has a weight of two and is only updated during the transmissions of the first and second transmission and then is not updated again until the next cycle of transmissions. Therefore, while coherent integration might be negatively affected for one virtual element, there could be enough return signal present in other virtual elements to still provide a detectable radar return. Secondly, a moving target with a constant Doppler shift being sampled at a set interval will apply a linear phase shift across the received data. If the Doppler shift is not compensated for, the linear phase shift will be interpreted by the radar as a stationary target, but at another angle related to the phase shift [34]. In other words, Doppler can induce an angle of arrival error while TDM is being used by a MIMO radar.

The aim is to determine how significant of a signal loss Doppler will cause and if any angle errors are produced in an effort to ascertain if the MIMO radar can still detect a moving target without using Doppler processing. The targets of interest being used for the next experiment remains boats on the surface of the ocean travelling at a maximum radial speed of 15 m/s. The same non-fluctuating target with $\sigma = 0.8$ m^2 is placed at a range of 1 km at 0^o relative azimuth. The search window is narrowed from ± 40^0 in 1^o increments to ± 20^0 in 0.5^o increments. The only variable for the experiment is the speed of the approaching target. The return from a single pulse from the phased array radar is used as reference for signal loss and angle of arrival comparison.

The radial speed of the target was varied between 0 to 65 m/s in 1 m/s increments. The mean return from a single pulse from the phased array radar simulation over these velocities was -112.5 dB. The mean return from the phased array was used as the reference to normalize the MIMO returns in Figure 3.21. Figure 3.21 depicts the MIMO radar simulation results with the theoretical integration loss originally presented in Figure 2.7. Using (2.16) with the radar parameters outlined in Table 3.6, the Doppler frequency, f_d, was calculated for the radial velocities between 0 to 65 m/s, which was then translated into the total Doppler shift over M=36 integrations, using $2\pi f_d MT$, where T is the PRI.

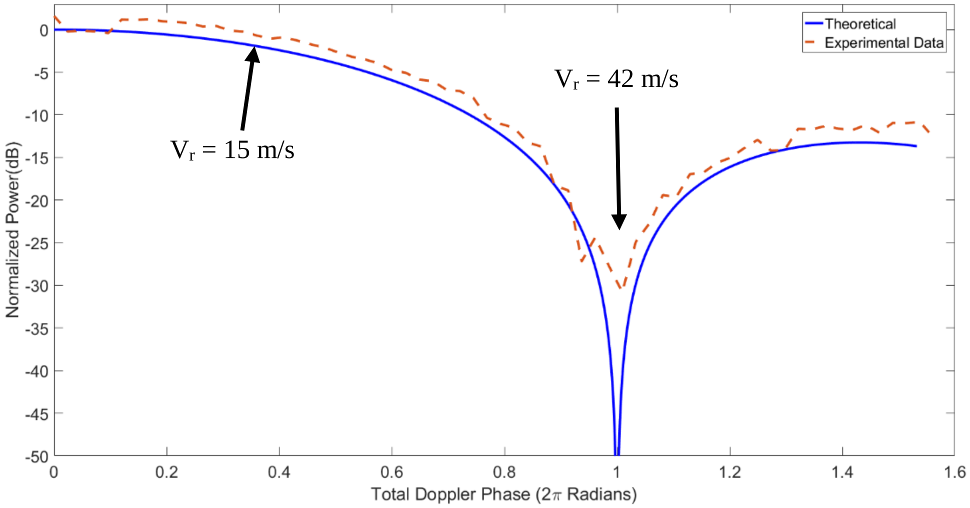

Figure 3.21 Simulated results for MIMO radar coherent integration loss

As it can be observed, without Doppler processing, a TDM MIMO radar follows the theoretical integration loss curve closely. There is a small DC offset present, which is likely due to the virtual elements not maintaining a consistent sample rate across the CPI. More importantly, the required speed of interest of 15 m/s has less than a 2 dB coherent integration loss. This result implies that so long as a 2 dB loss is acceptable to still be able to detect a target of interest, then a MIMO radar can be used as a substitute for a phased array radar to detect surface targets. Of course, this 2 dB loss is specific for the radar settings used in this scenario. The general restriction originally introduced as (2.19) should be applied when considering a MIMO radar for surface detection without Doppler processing to maintain integration losses to less than 4 dB:

$$M < \frac{PRF\ \lambda_o}{4v_r} \tag{3.6}$$

where M is the number of coherent integrations.

Although signal loss is one factor to consider, the other possible source of error that Doppler can introduce using TDM is angle of arrival. Figure 3.22 shows the error in angle received for the 66 simulated velocities, plotted against the total

Doppler phase shift during the CPI of the MIMO radar. The angular sample resolution was set to 0.5° increments.

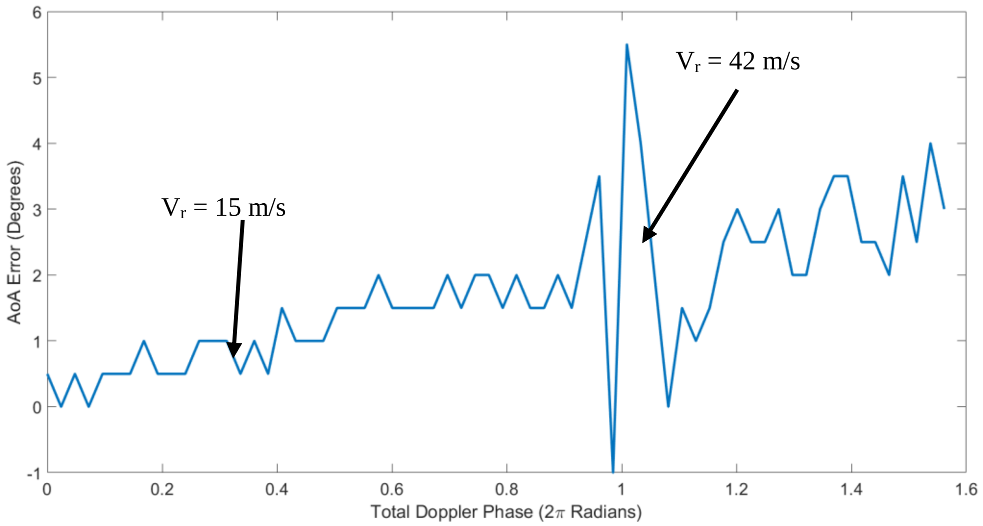

Figure 3.22 Angle of arrival (AoA) error produced by Doppler in a TDM MIMO radar

The angle of arrival error slowly increases with the total Doppler phase shift for the CPI of the MIMO radar. The error in angle remains at less than 1.5° for targets travelling less than 15 m/s. These Doppler angle errors are one of the significant drawbacks of TDM MIMO radar as it could be easily exploited by a jammer introducing Doppler information to the radar to create false targets. Electronic protective measures (EPM) would need to be investigated if TDM MIMO radar was to be used on a military platform, which is outside the scope of this thesis. To further illustrate the effects of Doppler from the last two figures, Figure 3.23 is provided which compares the MIMO and phased array radar returns and demonstrates the angle offset and signal loss of the MIMO radar against a target approaching at a velocity of 60 m/s.

In conclusion, with the radar settings used, a MIMO radar can detect surface targets travelling at less than 15 m/s without Doppler processing at a small cost in signal loss and angle error. If less than 3 dB of signal loss and 1.5° of angle error is not acceptable for the requirements of the radar, then some form of Doppler processing must be introduced or the required CPI of the MIMO radar must be lowered. The CPI could be lowered by using simultaneously transmitted orthogonal waveforms instead of TDM. This will however introduce additional processing in the form of more matched filters for the orthogonal waveforms and introduces the risk of cross-correlation between transmitting signals [4].

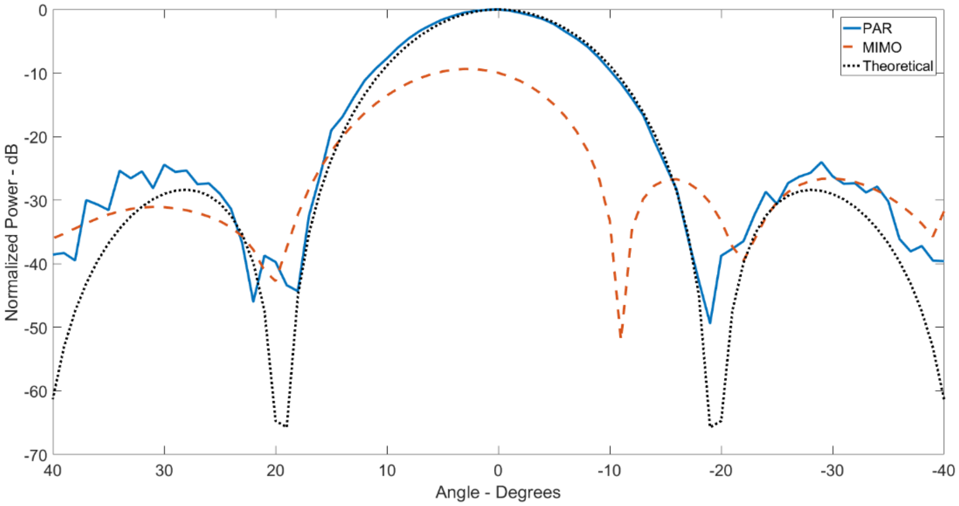

Figure 3.23 MIMO and phased array radar azimuth response for a target approaching at 60 m/s

With the inherent angle error from Doppler targets, a TDM MIMO radar should not be used as a tracking radar for military weapon systems unless Doppler processing is used with some form of EPM. Even though a MIMO radar is not recommended for high-resolution tracking, it is useful for detection. Although MIMO radar in the scenario described requires 36 additional returns to match the SNR of a phased array radar, the MIMO radar can scan the entire search area of interest at once. Furthermore, once a buffer of data is stored in the MIMO radar, it can refresh the entire radar picture after every pulse. This results in a much greater refresh rate of the radar picture compared to a phased array radar which needs to electronically scan or a navigation radar that requires to rotate. An analysis of the scan rate of a conventional radar versus the CPI of the MIMO radar is discussed in the next sub-section.

3.5.4 Multiple Moving Targets

A greater refresh rate of the radar picture results in more radar energy on target, which is advantageous for mitigating atmospheric nulls or multipath destruction. Although the MIMO radar requires a greater CPI to maintain the same SNR as a phased array radar, the MIMO radar can scan the entire search area and is only restricted by the element pattern of its transmitting and receiving antennas. The refresh rate of the MIMO radar will only be greater than that of a phased array radar for area searches where the scan rate of the phased array radar exceeds that of the CPI of the MIMO radar.

A total of 36 integrations was used in the previous examples for the MIMO radar to maintain the same SNR as the phased array radar, or a total time of 36(PRI) = 2.4 ms. The phased array scanned its beam electronically at a rate of 1^{o} for every PRI, or 66.7µs. Therefore, the phased array radar scans a 36^{o} search area during the CPI of the MIMO radar, meaning that if the search area is less than 36^{o} in azimuth, the phased array radar will provide a radar picture faster than the MIMO radar. However, the limiting value of 36^{0} of azimuth does not account that the MIMO radar is able to buffer its data and recall it to provide an update of the entire search area even faster. The MIMO radar does not require 36 new radar returns each CPI as newer radar returns can be used to update the radar picture by dropping the oldest data points from the previous CPI each time. In the case of simultaneously transmitted orthogonal waveforms, the MIMO radar can update the radar picture every pulse. For TDM MIMO radar, the refresh rate of the radar picture is dependent on the number of transmitters, which is six for the designed simulation. Therefore, the search area where the phased array radar is faster than the MIMO radar shrinks from 36^{o} to 6^{0} in azimuth, or approximately 400 µs. For comparison, a navigational radar rotating at 60 rpm will take 16.8 ms to update 6^{o} of azimuth.

It is important to highlight the increase in computational load that the MIMO radar will require during a CPI when compared to the phased array radar. Although it was just shown analytically that the MIMO radar will be able to update the radar picture faster if the search area is greater than 6^{o} of azimuth, there are significantly more calculations for the MIMO radar to perform to do this. Even though there are many other processing techniques that can be applied to a MIMO radar such as STAP techniques, only the processing implemented for the two simulations will be compared. Except for the formation of the virtual array in the MIMO radar, both radars systems use the same processing techniques to create a radar picture. Therefore, an analytical ratio equation can be used to define the increase in computational load of the MIMO radar compared to the phased array over a given CPI:

$$MIMO_{Comp} = \frac{Total\ Az_{Scan}}{PAR\ Az_{CPI}}\ PAR_{Comp} + Virtual_{Comp} \qquad (3.7)$$

where $MIMO_{Comp}$ is the total number of computations required for the MIMO radar during a refresh interval, $Total\ Az_{Scan}$ is the entire search area of interest in azimuth, $PAR\ Az_{CPI}$ is the total azimuth that the phase array radar scans during the refresh rate of the MIMO radar, PAR_{Comp} is the total number of computations required for the phased array radar during a refresh interval of the MIMO radar, and $Virtual_{Comp}$ is the total number of operations required to form a virtual array during a refresh interval. For the given scenario, the CPI of the MIMO radar is defined as 36(PRI) and its radar picture refresh rate is 6(PRI) and the $Total\ Az_{Scan}$ = 80°. Therefore, with the phased array scan rate set at 1° in azimuth for every PRI, $PAR\ Az_{CPI}$ = 6° and (3.7) becomes:

$$MIMO_{Comp} = 13.3\ PAR_{Comp} + Virtual_{Comp} \tag{3.8}$$

Consequently, the MIMO radar is performing at least 13.3 times more calculations over the same period in comparison to the phased array radar for the given scenario, but with the added benefit of providing a full radar picture. From a design perspective, this means that a MIMO radar will require additional processing capacity to handle the computational load increase. The number of virtual array computations is proportional to the number of virtual elements outlined in Table 3.5.

To illustrate the response of the MIMO radar over a large search area, five Swerling I targets were simulated with the characteristics outlined in Table 3.7. The resultant radar pictures from the MIMO radar are shown in Figure 3.24 and Figure 3.25. Both figures are only plotted out to a range of 2 km and after only a total of 36 radar returns. Figure 3.24 depicts the two-dimensional radar return whereas Figure 3.25 shows the three-dimensional return and how the targets are detected against a cell-averaging CFAR detector. Each radar picture is updated every sixth pulse, or 400 µs and demonstrates the ability of a MIMO radar to detect multiple targets in a large search area faster than a phased array radar.

Table 3.7 Simulated target parameters

RCS (m^2)	Range (m)	Azimuth	Velocity vector (m/s)
0.8	1200	1.4°	[-15 0 0]
1.9	1472	13.8°	[-6 5 0]
1.4	1856	-18.5°	[5 -1 0]
0.7	776	15°	[12 5 0]
0.6	270	-21.8°	[-10 5 0]

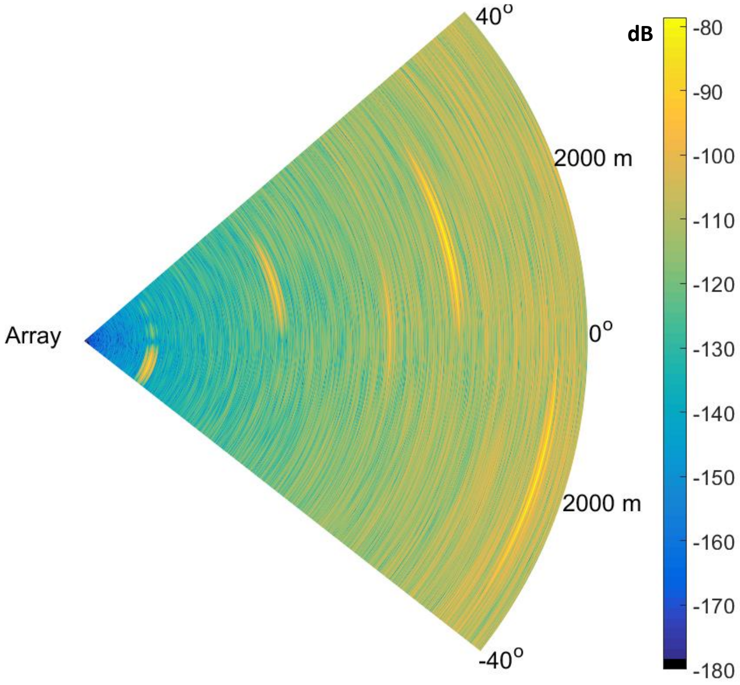

Figure 3.24 MIMO radar response for simulated targets

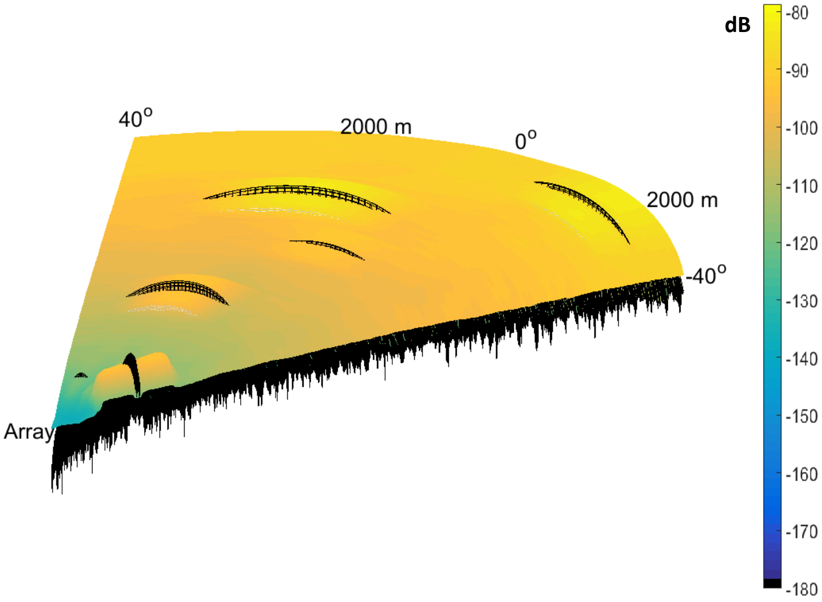

Figure 3.25 MIMO radar response against a cell-averaging CFAR detector for five targets

3.5.5 Moving Target with Sea Clutter

Sea clutter is one of the primary sources of interference in detecting surface contacts on the ocean [16]. While this thesis is not performing an in-depth analysis of ways of improving sea clutter suppression using a MIMO radar, it is important to explore the performance of the MIMO radar for at least one scenario and compare it with the response from the phased array radar. The amount of reflection from sea clutter is largely dependant on the sea state, which defines the wave height and the incident angle with the surface of the ocean. Therefore, in general, the sea clutter will be greatest closest to the radar platform.

Using the sea clutter algorithm described in Section 3.2.3, an environment with sea state 4 was created for simulation. As a RCS value is provided to sea clutter for every sampled area, the simulation was limited to a maximum range of 750 m and a scan area of ±5°. Even after limiting the area, the sea clutter simulator still provided nearly 3000 sea clutter RCS values to simulate. A Swerling I target with a RCS of $\sigma = 0.8$ m^2 was placed at a range of 500 m at boresight with an approaching speed of 15 m/s.

Figure 3.26 and 3.27 show the three-dimensional radar response of the MIMO and phased array radars, respectively. The peak response in both figures represents the location of the target at 500 m. The difference in the peak response between the two radar systems is approximately 2 dB, which corresponds to the coherent integration loss from Doppler for the MIMO radar. The noise floor varies with range, but is equivalent for both radar systems and sits around -90 dB at 500 m. The peak return from the target is approximately -70 dB for the MIMO simulation and -68 dB for the phased array radar, resulting in a SNR of 20 dB and 22 dB, respectively. The variance in the noise level caused by sea clutter is significantly less when STC is being used as part of the signal processor. To illustrate this, Figure 3.28 depicts the MIMO radar simulated response of the same scenario, but without the presence of sea clutter. Lastly, the noise level at a range of 500 m without sea clutter is approximately -112 dB, meaning that sea state 4 clutter lowered the SNR of the target at 500 m by 22 dB.

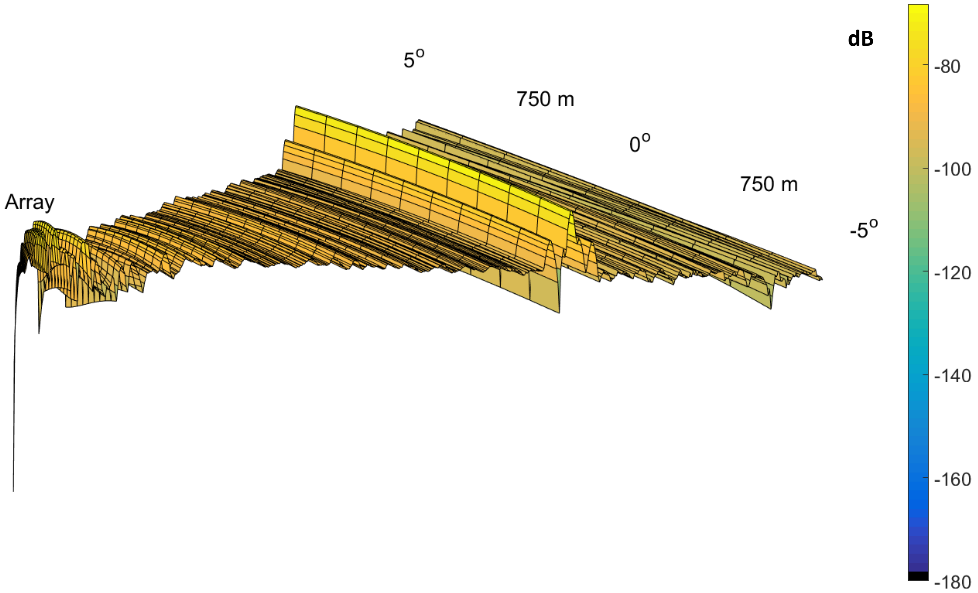

Figure 3.26 Simulated MIMO radar response of a target at 500 m with sea state 4 clutter

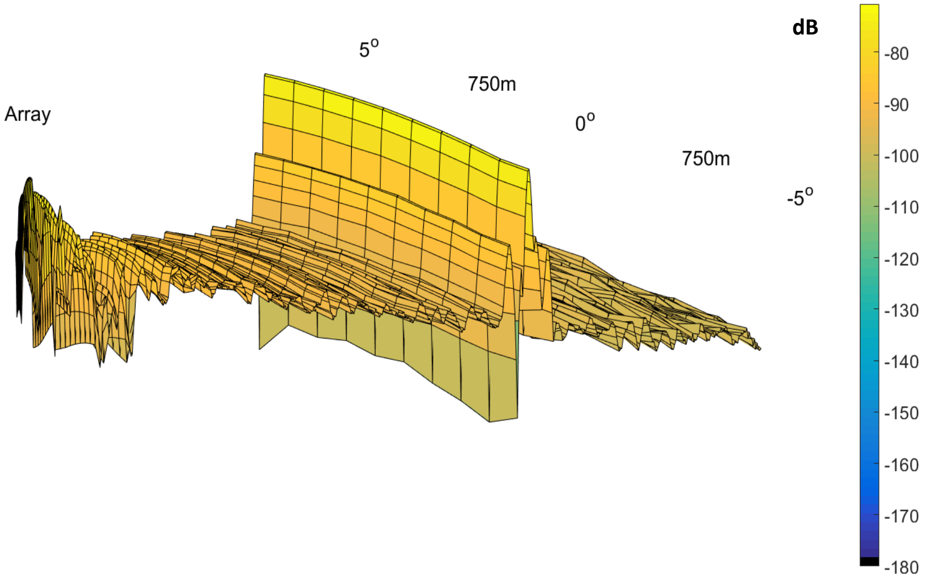

Figure 3.27 Simulated PAR radar response of a target at 500 m with sea state 4 clutter

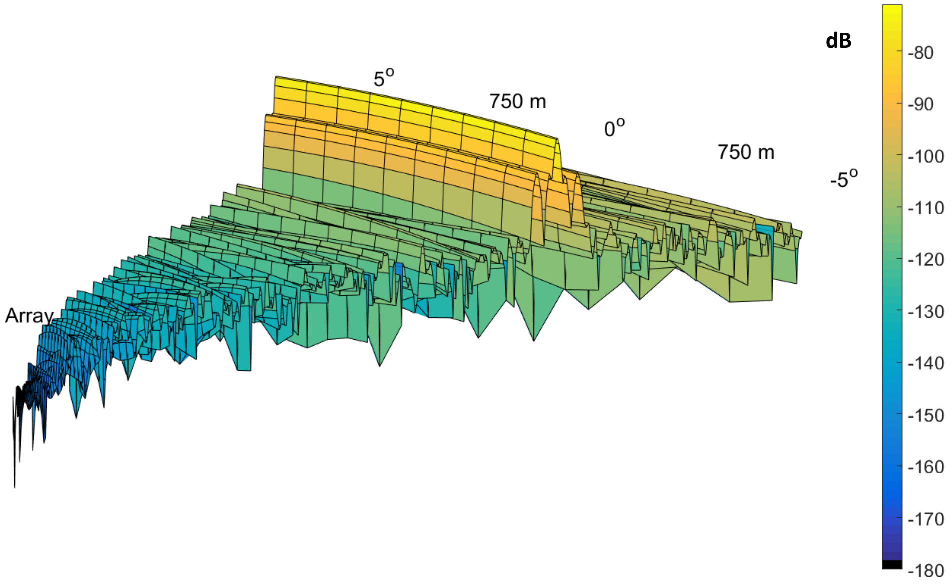

Figure 3.28 Simulated MIMO radar response of a target at 500 m without sea clutter

In conclusion, the MIMO and phased array radar systems are both able to detect the same target with similar results in the presence of sea clutter. Although the scenario presented herein is limited to a single target and a dictated sea state, it does demonstrate that a MIMO radar is able to detect a target with values of SNR that are similar to those of a phased array radar. Future work should include the examination of the benefits of STAP techniques that are available to MIMO to ascertain their benefits of detecting targets in various sea states. Work such as [35] and [36] have already performed GLRT tests and ROC curves with Monte Carlo simulations with different forms of clutter distributions to show that a MIMO radar will perform better than conventional radars. Lastly, sea clutter is not Gaussian interference, so any future work will require an understanding of the distributions of the RCS and sea clutter statistics.

3.6 Summary

This chapter presented the design of the phased array and MIMO radar simulations using MATLAB 2016b and Simulink. The common processing techniques were covered and the differences between the two radar systems were highlighted. Several scenarios were used to investigate the differences and similarities between the two radar systems and to determine if MATLAB and Simulink could be used as a processing tool for an experimental radar platform.

It was shown that the two-way beam patterns of the two radars are equivalent and that the SNR of the two systems are the same so long as the MIMO radar integrates enough returns over a CPI. Although the SNR was maintained between the two radar systems for a stationary target, integrating returns over a CPI with moving targets had a negative impact on the MIMO radar. It was shown that depending on the relationship of the target’s speed, the radar’s PRF, and the CPI of the MIMO radar, that MIMO could still detect moving targets without Doppler processing with small errors in angle of arrival and some loss in efficiency in coherent integration. It was also demonstrated that a MIMO radar can scan a large area much faster than a conventional rotating navigation or electronically scanned phased array radar, but at a cost of extra processing. Lastly, it was shown that the MIMO radar can detect a target and use conventional radar processing techniques to suppress sea clutter and detect a target.

MATLAB and Simulink proved to be useful resources for radar signal processing and simulation. The simulations and the scenarios were used as the backbone to design an experimental MIMO radar platform.

4 Experimental MIMO Radar Design and Results

This chapter presents the design of the hardware used to create an experimental MIMO radar. Section 4.1 summarizes the requirements for the experimental radar platform. Section 4.2 discusses the initial use of SDRs and the design challenges that prevented them from being used to implement a functional radar. Section 4.3 provides the requirements and steps taken to create a wideband microstrip patch antenna, which was used to form an 8-element ULA for experimental use with the MIMO radar. Antenna design details and simulations from the Advanced Design System (ADS) and antenna measurements from the anechoic chamber are discussed. Section 4.4 describes the implementation of an experimental TDM MIMO radar with a network analyzer and its control through MATLAB and Simulink whereas Section 4.5 provides experimental results for various scenarios. Lastly, Section 4.6 summarizes the radar designs and provides conclusions from the empirical results.

4.1 Experimental Radar Requirements

The experimental radar needed to be portable and capable of being used in a laboratory environment. An initial requirement was for the platform to be capable of switching between a phased array and MIMO radar configuration to allow for direct empirical comparison between the two radar systems. Although an initial design was prepared for a phased array radar for use with the SDRs, it was quickly determined there were significant design challenges in achieving a coherent phased array radar. Therefore, the requirement for an experimental phased array radar was removed for various reasons that will be covered throughout this chapter. Fabricating a functioning experimental MIMO radar system to demonstrate resolution and detection capabilities similar to what was shown in the simulation results became the primary requirement.

The experimental MIMO radar has to be consistent with the one simulated in the previous chapter. Therefore, the experimental radar must be capable of interfacing or providing data to MATLAB or Simulink for post-processing.

Furthermore, TDM must be used to achieve orthogonality between coherent waveforms operating somewhere between L and X band. An initial requirement that was later removed due to complications with the SDRs was that the transmitting waveform could be adjusted and selected. While desirable for future work, the aim of the research was still achieved with the solution implemented with the network analyzer which restricts the transmitting waveform to stepped frequency continuous wave.

A specific frequency or frequency range would be set based on the equipment used and a ULA built with half wavelength spacing from supplies available within RMC's radar lab. As the purpose of the radar system is to be used in a laboratory setting, the radar system must be able to achieve a range resolution of less than 1m with at least four separate transmit and receive channels. The power output of the radar system had to be sufficiently strong to detect various types of radar targets within the anechoic chamber out to a maximum range of at least 6 m with less than 16 coherent integrations. In-line power amplifiers could be used if required to amplify the transmitting waveform. The MIMO radar system must be capable of processing all transmit and receive channels independently from one another to form a virtual array. The virtual array two-way pattern must be adjustable where specific transmit and receive channels are either turned off or not processed to allow for different two-way antenna patterns.

All receive signal processing techniques used in the MIMO radar simulation must be able to be implemented with the experimental radar platform. At a minimum, the MIMO radar system must be capable of forming a virtual array, conduct beamforming, perform STC, use coherent integration, and detect a target against a cell-averaging CFAR detector.

4.2 Software Defined Radio Option

The SDR was an attractive, portable, flexible, and relatively inexpensive option that advertised specifications that should have met the requirements to create a MIMO radar. Several months were spent working with a single Universal Software Radio Peripheral (USRP) X310 to determine if it was a feasible option with which to build a MIMO radar. The USRP X310 is a low power RF transmit and receive device from Ettus Research, National Instruments that allows the use of custom waveforms over a 1.14 to 6.06 GHz frequency band with twin CBX-120 daughterboards [37]. Each of the two CBX-120 boards allow for 120 MHz of bandwidth on two simultaneous transmit and receive RF channels. The USRP X310 is programmable through software programs such as GNU Radio [38], Labview [39] or MATLAB Simulink using the USRP Hardware Driver (UHD) that is written in C/C++ code. The X310 also contains a Xilinx Kintex-7 FPGA (XC7K410T) that is programmable and can be used for signal processing purposes. Lastly, the X310 has an internal 10 MHz reference clock as well as a pulse per second (PPS) reference for timestamp synchronization with other SDRs or the ability to use an outside reference such as a GPS clock for synchronization. The full specification sheet for the USRP X310 can be found at [37]. Figure 4.1 depicts a high-level schematic of the internal interfaces for the USRP X310.

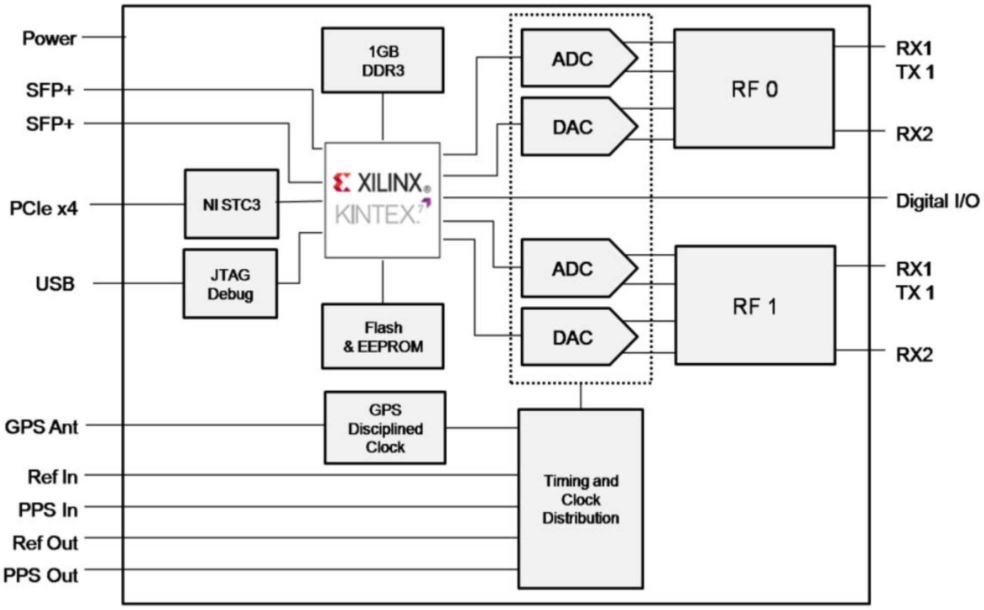

Figure 4.1 Schematic of USRP X310 [29]

For preliminary testing, a single X310 was connected to a high-performance Linux computer via SFP+ 10 Gigabit Ethernet. The Linux computer ran a 64-bit operating system with an Intel Xeon CPU E5-2660 operating at 2.60 GHz and 128 GB of RAM. MATLAB and Simulink were used as the primary interface to program the SDR to maintain consistency with the simulations outlined in Chapter 3. The goal of the preliminary testing with a single X310 was to prove that it was capable of transmitting and receiving desired waveforms over a single channel and to verify the interface with MATLAB and Simulink before attempting to synchronize multiple SDRs.

Using the Communications System toolbox, Simulink can adjust settings for various USRP SDRs with the SDRu Receiver and Transmitter blocks. The Simulink model used to communicate with the X310 for preliminary testing is shown in Figure 4.2 whereas Figure 4.3 demonstrates the available settings for the X310 transmitter from the SDRu transmitter block. A phase-coded waveform block from the Phased Array toolbox is connected to the input of the SDR transmitter whereas the SDR receiver output is saved to a workspace for post-processing in a different Simulink model. The post-processing model used similar processing techniques described for the simulations of Chapter 3. The Kintex-7 FPGA was not used for processing.

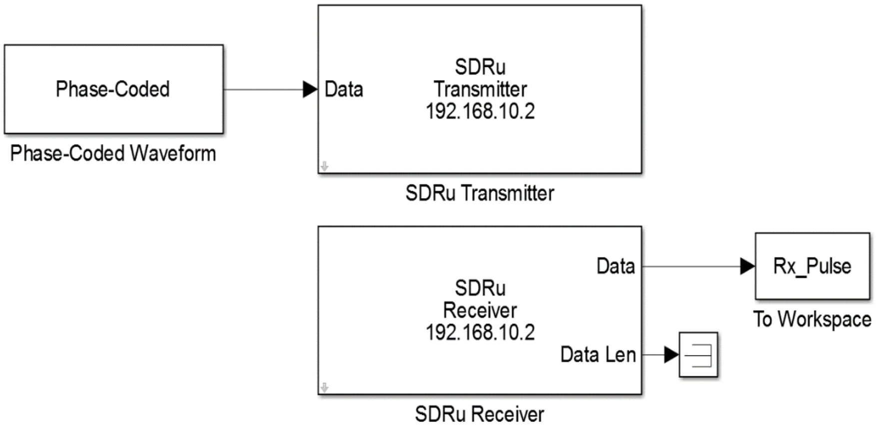

Figure 4.2 Simulink model for communication with a single USRP X310

Testing was conducted through a loopback test by connecting the transmitted signal from channel 1 through a splitter to receivers 1 and 2 with two identical 2-foot SMA cables, as shown in Figure 4.4. A loopback test was used to eliminate any antenna or environmental considerations from testing and to ensure that the RF channels were identical for both receivers. Experimentation was performed over two distinct phases. The first phase used the receiver from channel 1 only to verify waveform reception and the interface with Simulink whereas the second experiment used both received channels to test internal coherence between the two channels of the CBX-120 daughterboards.

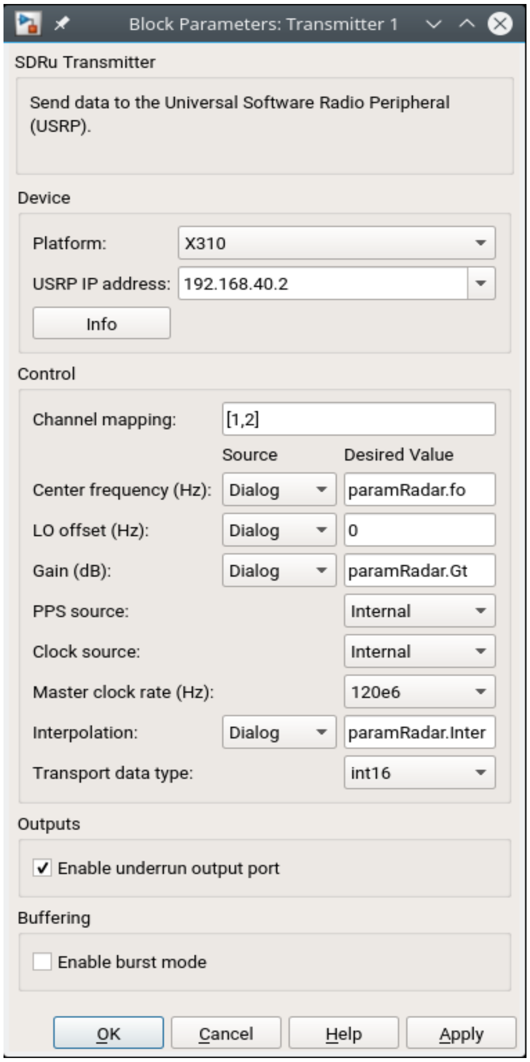

SDRu Transmitter

Send data to the Universal Software Radio Peripheral (USRP).

Device

Platform: X310

USRP IP address: 192.168.40.2

Control

Channel mapping: [1,2]

	Source	Desired Value
Center frequency (Hz):	Dialog	paramRadar.fo
LO offset (Hz):	Dialog	0
Gain (dB):	Dialog	paramRadar.Gt
PPS source:		Internal
Clock source:		Internal
Master clock rate (Hz):		120e6
Interpolation:	Dialog	paramRadar.Inter
Transport data type:		int16

Outputs

☑ Enable underrun output port

Buffering

☐ Enable burst mode

Figure 4.3 USRP X310 transmitter settings from Simulink

During the single channel loopback tests, several issues and design limitations were uncovered. Firstly, the sample rate of the SDR is defined by the Master Clock rate divided by the interpolation or decimation rate set from SDRu transmitter or receiver blocks, respectively. The Simulink model sample rate, or more specifically the sample rate of the waveform being transmitted, must be identical to the sample rate of the SDR. If the sample rates do not match, then the actual transmitted waveform will be stretched or compressed based on the ratio of the two sample rates during the DAC process within the SDR. Thus, the sample rate

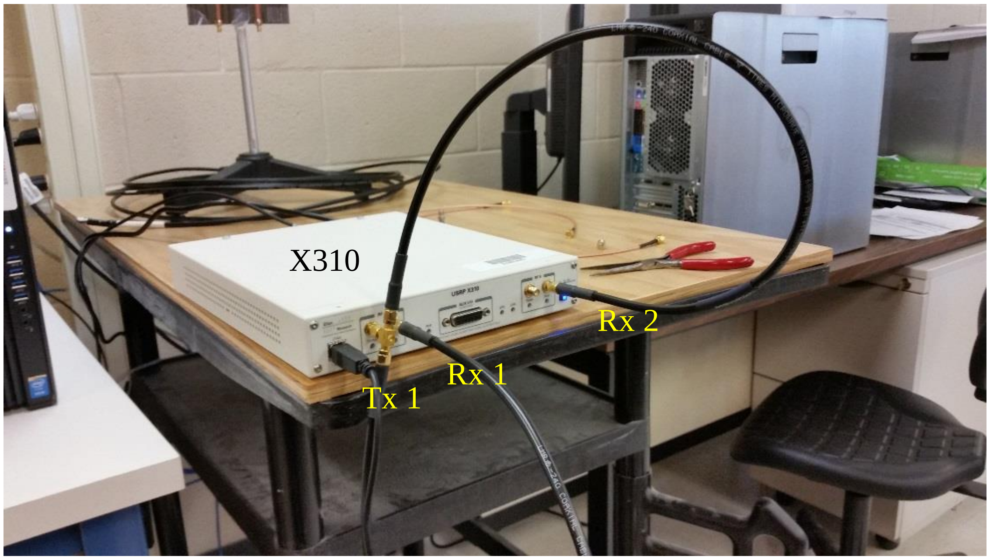

Figure 4.4 Loopback test for the USRP X310

of the SDR restricts the resolution of the waveforms that can be simulated in Simulink and will define the radar's range resolution. For example, if the master clock of the SDR is set to 120 MHz with an interpolation of 1 for transmission and a decimation rate of 1 for reception, then the sample rate for the DAC and ADC processes within the SDR will be performed at 120 MHz. This sample rate translates into the maximum useable bandwidth for a rectangular pulsed waveform. If the transmitted waveform is sampled at 120 MHz in the Simulink model, then the sampled resolution of the waveform in time equates to 8.33 ns. Using (2.6) with M=1 for a rectangular pulse and equating the pulse width to 8.33 ns, the maximum range resolution that can be achieved for the radar is 1.25 m. As space is limited in the lab, a radar range resolution of 1.25 m is not ideal and does not quite meet requirements, but it is useable to perform detection assessments against multiple targets.

However, a range resolution of 1.25 m could not be achieved with a single channel because the 10 Gb Ethernet connection and the Linux computer could not maintain the necessary throughput without experiencing data overruns or underruns on transmit and receive. Underruns and overruns are ADC/DAC timing errors that will distort any received or transmitted signals. When performing range resolution testing, the Simulink model in Figure 4.2 was run in rapid acceleration mode with the data transport type to the SDR set to Int16, or 16 bit integers. The best interpolation and decimation rates that could be achieved with a master clock of 120 MHz without experiencing significant data errors was 10 for a single channel on transmit only. When attempting to use transmit and receive functions on a single channel, the interpolation and decimation rates were required to be above 20 to avoid errors. The equivalent bandwidth for the radar with an interpolation rate of 10 and a master clock of 120 MHz equates to 12 MHz resulting in a radar range resolution of 12.5 m. While a 12.5 m resolution would be excellent for an operational radar, it is not useable in the lab setting. Figure 4.5 demonstrates the underruns received over many sample intervals on a single channel alternating between transmitting only and then simultaneously transmitting and receiving. As it can be observed, underruns continuously occurred when attempting to transmit and receive on only 1 of the 2 available channels on the USRP X310 at a sample rate of 12 MSa/s. Furthermore, even when only transmitting, there are still consistent intervals of underruns occurring.

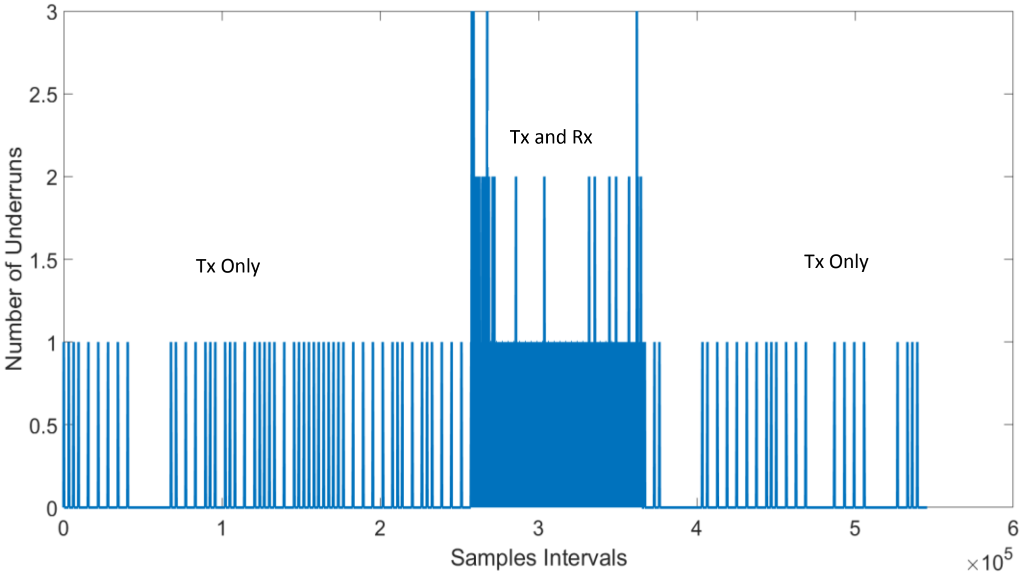

Figure 4.5 SDR Underruns for a single channel with a sample rate of 12 MSps

To minimize the required instantaneous bandwidth and the sample rate of the SDR while satisfying the required range resolution, stepped-frequency continuous wave waveforms were explored. As discussed in Chapter 2, (2.8) defines the range resolution of a radar using a stepped-frequency continuous wave and the effective bandwidth of the system is dependent on the number of frequency steps and step size. Using this type of waveform solved the data rate issue, but at the cost of restricting the radar to a single waveform type. Several experiments were conducted to test this waveform in both a single and dual channel configuration.

Several issues were uncovered when attempting to use the stepped-frequency waveform. Firstly, it was discovered that the oscillators within the X310 took approximately 25 milliseconds to tune to a different frequency. This phenomenon resulted in additional signal processing being implemented for the radar to ignore the first several returns at a new frequency. It also unnecessarily increased the CPI of the radar. Furthermore, inconsistent phase errors occurred when the sampling rate of the SDR was not an integer multiple of the operating frequency. The RF channel was a 2 foot SMA cable in a loopback configuration so it was expected to receive the same phase for each return at a given frequency. Figure 4.6 depicts the I and Q amplitude returns of a loopback test for several frequencies. The waveform used in this test was a rectangular pulse. Figure 4.6 shows the 25 ms settling time for the oscillators when tuning to a new frequency and demonstrates

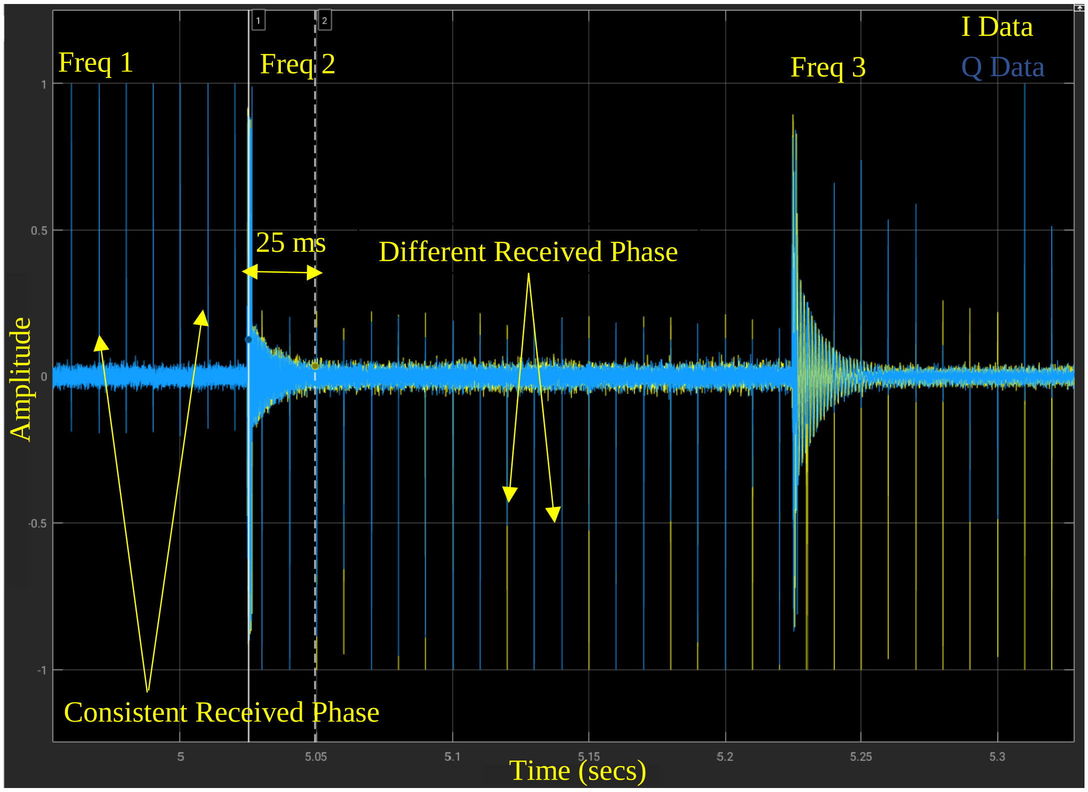

Figure 4.6 USRP X310 single channel loopback test

the phase inconsistency when the sampling rate and operating frequency are not integer multiples of one another.

The last experiment tested the phase coherence internally within the X310 between the two CBX-120 daughterboards. The experiments used sampling rates of integer multiples of the operating frequency to avoid the issues highlighted in the previous paragraph. The first test used a loopback test with a 2-foot SMA cable on only one channel and alternated back and forth between two frequencies. The goal of this test was to determine if phase remained coherent for the same frequency after the oscillators were retuned. A rectangular pulsed waveform was used for testing. A frequency transmitted for 30 intervals before alternating to the other frequency. As the RF channel is a cable, it was expected that the received phase for every second grouping of 30 pulses should be the same. The results of the test are shown in Figure 4.7 where it can be observed that the I and Q data does not remain consistent. Inconsistent phase information for I and Q data for the same frequency over an unchanging RF channel means that there is no phase coherence. Without phase coherence, the SDR could not be used for a MIMO radar.

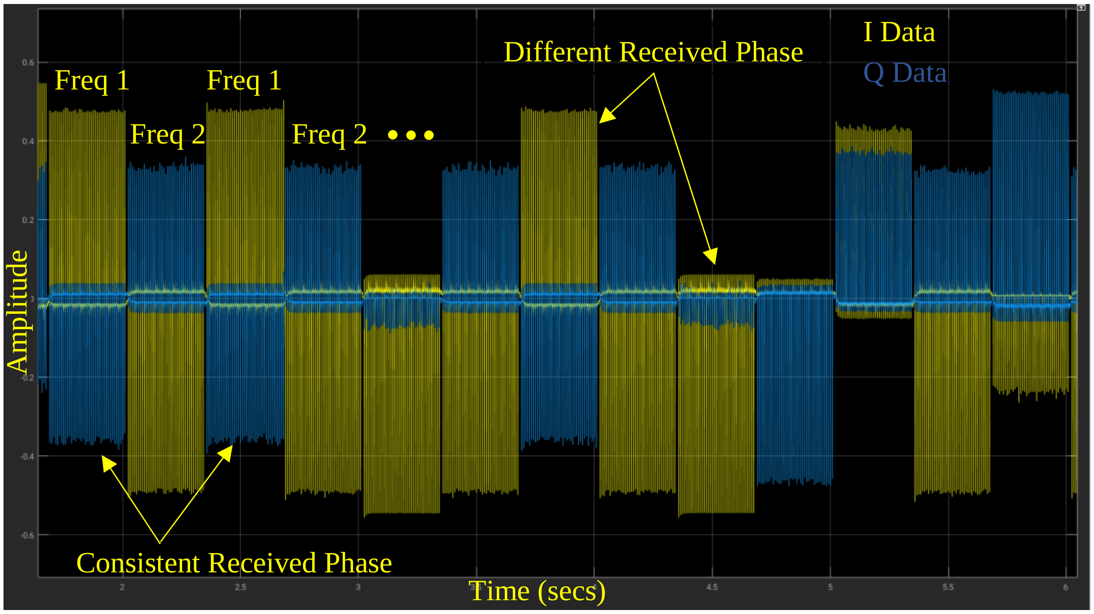

Figure 4.7 Alternating frequency phase coherence experiment

In a final attempt to mitigate this phase offset, one of the RF channels from the SDR could be configured to a permanent loopback configuration to serve as a reference and to record the phase offsets to eliminate them in post-processing. For this solution to work, the phase offsets would have to be equal across all SDR channels. To test this theory, a loopback test was performed by transmitting a rectangular pulse waveform on channel 1 and receiving the returns on channels 1 and 2 through a splitter and a pair of 2-foot SMA cables. In other words, this experiment tested the phase coherence between the two CBX-120 daughterboards within the same USRP X310 using its internal clock as a reference. The experiment alternated back and forth between two frequencies on a 30-pulse interval and used the I and Q data from the two received channels to compare their phases to one another. Figure 4.8 is a high-level schematic of the experiment showing the basic processing scheme used to compare the phase of the two receiver channels. Figure 4.9 shows the output of the phase comparison between the two channels for one of the many experiments conducted. The phase offset changed between the two receivers whenever the X310 was tuned to a new operating frequency. This observation was made over multiple experiments and the offsets were not repeatable. This implies that the two CBX-120 daughterboards within the X310 do not tune to the same phase when changing frequencies, meaning that phase coherence between the different channels is impossible.

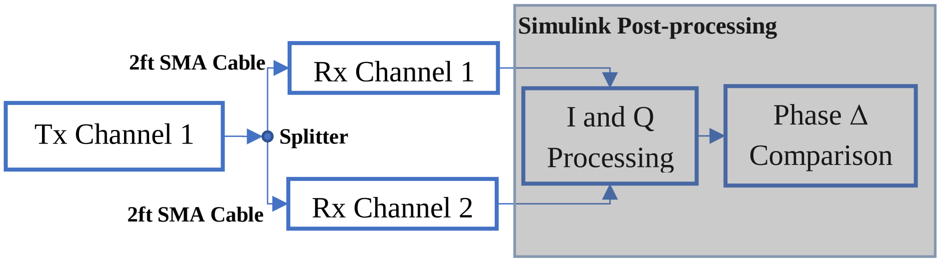

Figure 4.8 Cross-channel phase coherence experiment setup

Based on these observations, the SDR was abandoned in favour of a network analyzer to build an experimental MIMO radar, which will be discussed in Section 4.4. The data rate limitations and the inability to achieve phase coherence with the X310 were the limiting factors. After communicating with Ettus Research, they suggested to work with their SBX or UBX daughterboards, instead of the CBX board, to achieve phase coherence. Although this thesis moved away from working with SDRs, other organizations have had success in resolving the issues observed. Ref [40] used a single transmission channel of a SDR to examine various waveforms; however, radar targets were not being detected, so resolution and coherence between channels was not a consideration. Ohio State University performed a single target

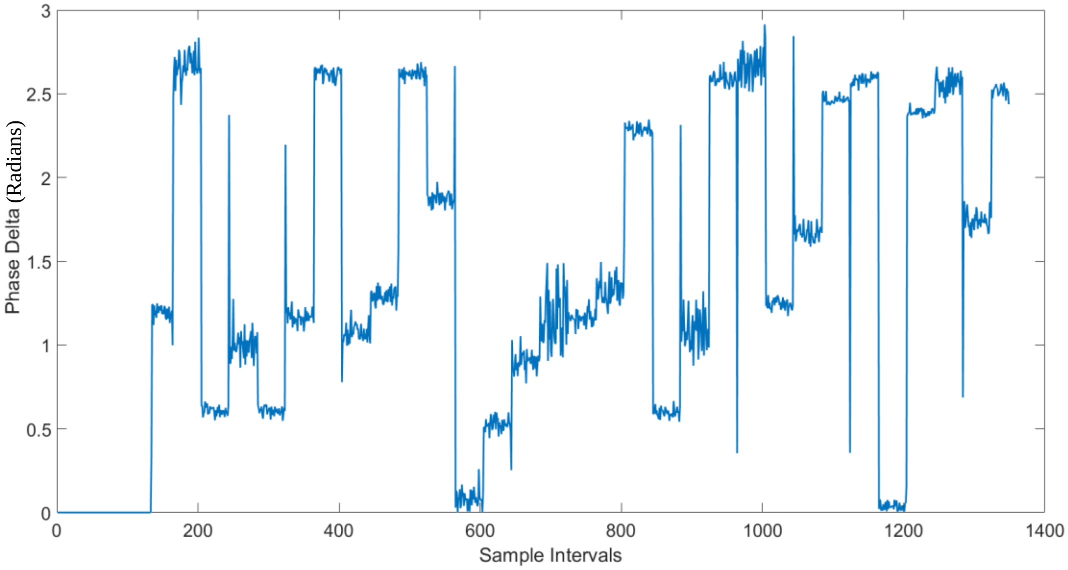

Figure 4.9 Received phase offset between channels Rx 1 and Rx 2

detection in an anechoic chamber with SDRs and compensated for phase coherence with several internal and external reference clocks [41]. They also programmed the FPGA within the SDR to minimize data rate requirements. Using GNURadio, Karlsruhe Institute of Technology (KIT), Germany built a 4x4 OFDM MIMO radar with SDRs and used Python coding to measure and compensate for phase coherence across several synchronized SDRs [42]. They also managed to achieve 200 MSps with two 10 GB Ethernet cards by overclocking a MSI motherboard of an Intel Xeon E5 server-type processor and used a RAMDisk as the first line of storage for the SDR samples. In conclusion, if a SDR is to be used to build a laboratory MIMO radar, consideration and extensive work must be done to ensure phase coherence between RF channels and that the data rates can be achieved for a desired sample rate.

4.3 Antenna and Array Design

Moving away from SDRs and towards a network analyzer to construct a laboratory MIMO radar introduced specific antenna requirements. The N5244A PNA-X uses stepped-frequency continuous wave waveforms on transmission, which is inherent to the device; therefore, a radar built with a PNA-X would be restricted to this type of waveform. As a result, a PNA-X radar is required to meet the required radar range resolution and maximum unambiguous detection ranges using (2.8) and (2.9), respectively. To meet these range and resolution requirements, a large operational bandwidth is needed; therefore, the antennas being used by the radar system must operate with as wide of an operational bandwidth as possible.

Antennas such as horn and dipole antennas were considered, but it was determined very quickly that the physical spacing between elements could not achieve half wavelength spacing or the radiation patterns were not desirable. Therefore, microstrip patch antennas were examined due to their compact size and the ability to fabricate an entire ULA on a single board. Unfortunately, microstrip patch antennas are inherently narrowband, with BW of around 1% of the operational frequency [43]. At X-band, this equates to a bandwidth of approximately 100 MHz resulting in a range resolution of 1.5 m. While a 1.5 m range resolution is useable, there are design methods to widen the bandwidth of a microstrip patch antenna and to improve the resolution further.

Applying wideband microstrip patch design principles [44,45] and antenna theory [46], a U-shaped broadband microstrip patch antenna was designed in Advanced Design System (ADS) software. The ADS schematic outlining the dimensions of the antenna is shown in Figure 4.10. The substrate used to fabricate the antenna is Taconic TLY-3 with a thickness of 1.57 mm and a relative dielectric permittivity, ε_r = 2.33 [47]. The antenna was designed to operate at a center frequency of 8.9 GHz with as wide of a bandwidth as possible. A X-band frequency was selected over S-band as a 1 % operational bandwidth is much greater at higher frequencies. Figure 4.11 demonstrates the useable bandwidth of the antenna with a plot of S_{11} showing an operational bandwidth of over 350 MHz at –10 dB or around 4 % of the center frequency. Using (2.8), a 350 MHz bandwidth equates to a range resolution of 43cm. Figure 4.12 depicts the current distribution of the antenna during an ADS simulation at 8.9 GHz whereas Figure 4.13 demonstrates the E-plane radiation pattern of the antenna showing an antenna gain of over 8 dB at boresight.

The U-shaped microstrip patch antenna was designed small enough so that the antennas could be spaced at half wavelength intervals of the center operating frequency to form a ULA. Based on the S_{11} results of Figure 4.11, the lowest point of the graph at 8.925 GHz was selected as the center operating frequency so the spacing of the antennas was set at 16.8 mm to form a ULA. Although the PNA-X network analyzer only has 4 ports, an 8-element ULA was fabricated for flexibility and possible future expansion. Figure 4.14 is a picture of the fabricated ULA.

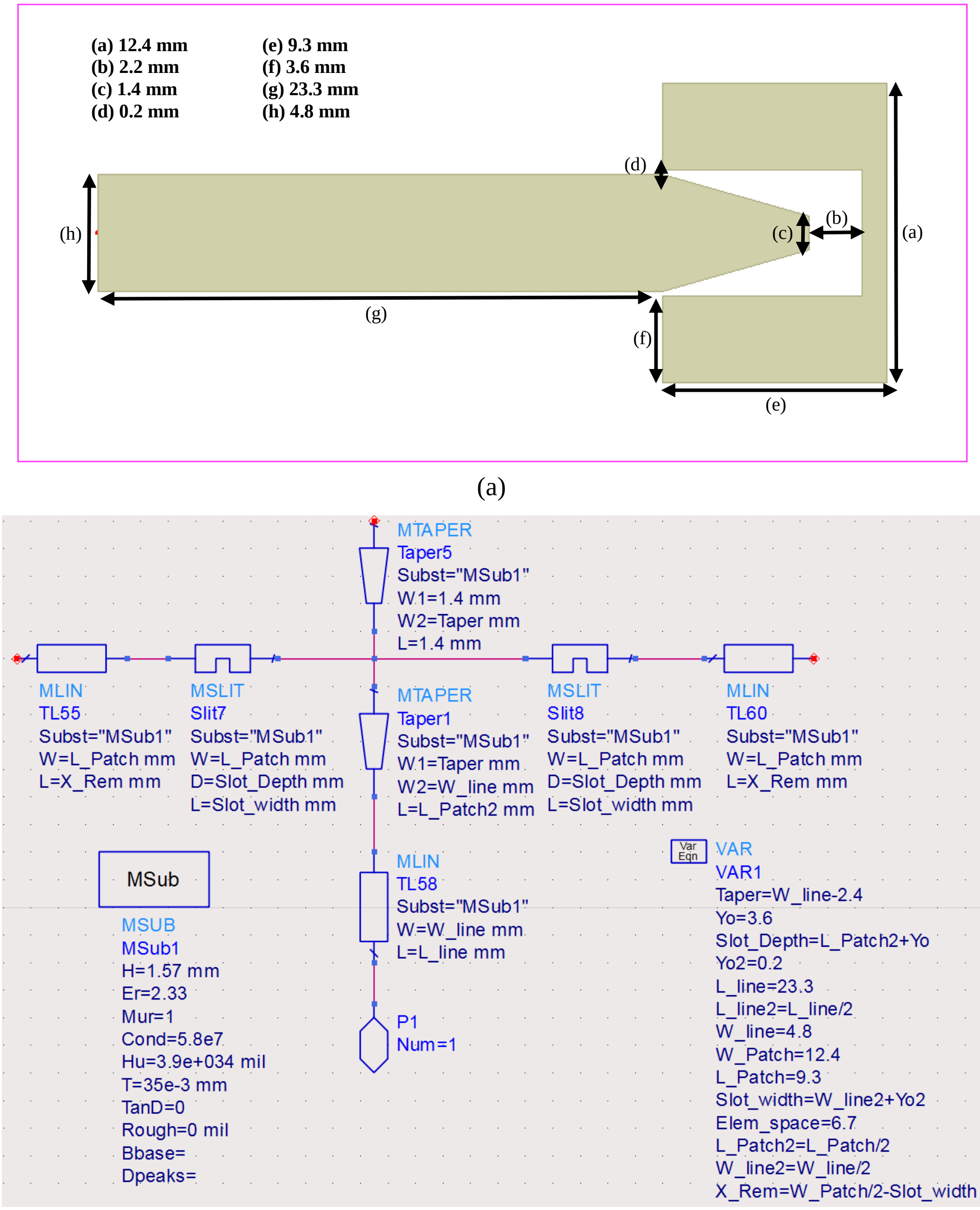

(a)

MTAPER
Taper5
Subst="MSub1"
W1=1.4 mm
W2=Taper mm
L=1.4 mm

MLIN
TL55
Subst="MSub1"
W=L_Patch mm
L=X_Rem mm

MSLIT
Slit7
Subst="MSub1"
W=L_Patch mm
D=Slot_Depth mm
L=Slot_width mm

MTAPER
Taper1
Subst="MSub1"
W1=Taper mm
W2=W_line mm
L=L_Patch2 mm

MSLIT
Slit8
Subst="MSub1"
W=L_Patch mm
D=Slot_Depth mm
L=Slot_width mm

MLIN
TL60
Subst="MSub1"
W=L_Patch mm
L=X_Rem mm

MSub

MSUB
MSub1
H=1.57 mm
Er=2.33
Mur=1
Cond=5.8e7
Hu=3.9e+034 mil
T=35e-3 mm
TanD=0
Rough=0 mil
Bbase=
Dpeaks=

MLIN
TL58
Subst="MSub1"
W=W_line mm
L=L_line mm

P1
Num=1

Var
Eqn

VAR
VAR1
Taper=W_line-2.4
Yo=3.6
Slot_Depth=L_Patch2+Yo
Yo2=0.2
L_line=23.3
L_line2=L_line/2
W_line=4.8
W_Patch=12.4
L_Patch=9.3
Slot_width=W_line2+Yo2
Elem_space=6.7
L_Patch2=L_Patch/2
W_line2=W_line/2
X_Rem=W_Patch/2-Slot_width

(b)

Figure 4.10 Broadband U-shaped microstrip patch antenna. (a) Dimensions of U-shaped microstrip patch antenna. (b) Detailed ADS schematic for microstrip patch antenna design

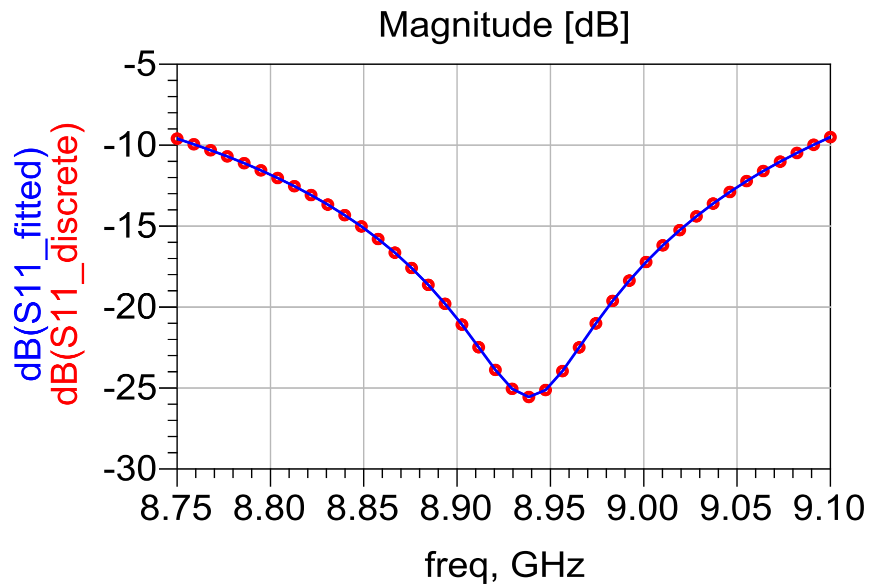

Figure 4.11 Simulated ADS S_{11} return for the U-shaped microstrip patch antenna

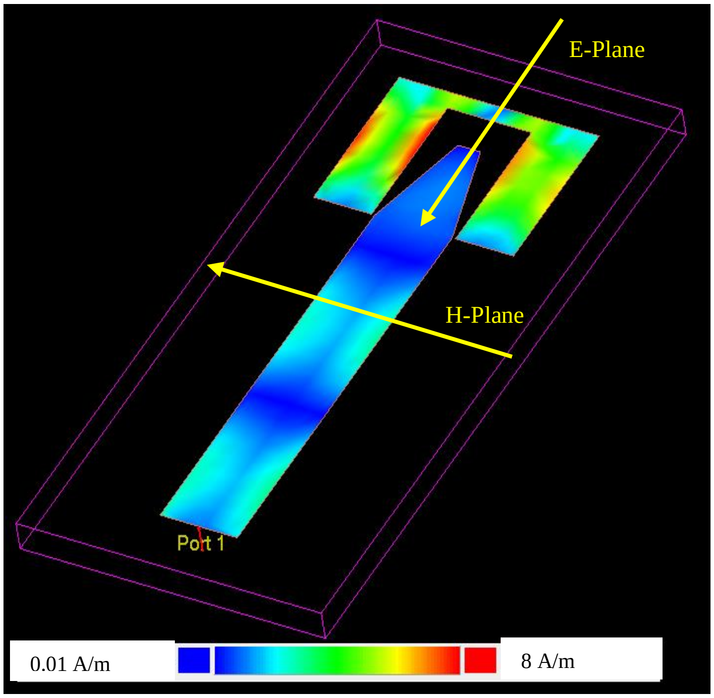

Figure 4.12 Current distribution of the U-shaped microstrip patch antenna

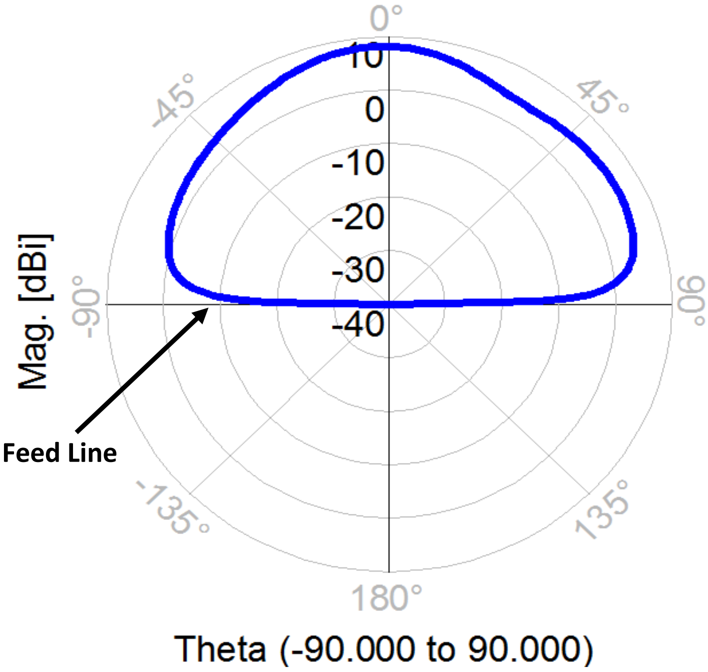

Figure 4.13 E-plane gain cut of ADS simulated radiation pattern

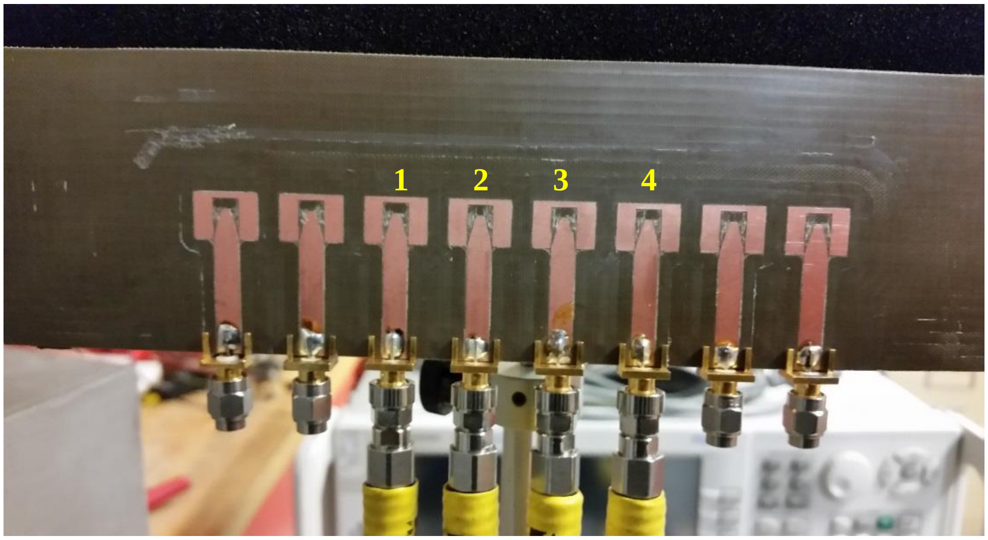

Figure 4.14 8-element ULA built with wideband microstrip patch antennas

Several experiments were conducted to verify the performance of the ULA against the ADS simulation results. The first test verified the operational bandwidth of the ULA. Four of the eight microstrip patch antennas were connected to a N5244A PNA-X network analyzer where S_{11}, S_{22}, S_{33}, and S_{44} were measured and compared. The results are depicted in Figure 4.15 where it can be observed that each antenna has a different bandwidth response. However, even for the worst measurement, S_{44}, the –10 dB bandwidth is close to 500 MHz or approximately 5.5 % of the operating frequency. It is also important to highlight that the lowest point of the S-parameter response shifted to approximately 8.79 GHz compared to 8.925 GHz from the ADS simulation. The shift in center frequency, increase in bandwidth and differences in S-parameter responses is likely due to the accuracy of the machine that fabricated the ULA and the mutual coupling between antennas that was not accounted for in the ADS simulation. When simulating the antennas in ADS, it was found that a 0.1 mm change to a dimension had significant impact on the antenna bandwidth and radiation pattern.

Figure 4.15 S-parameter response of 4 microstrip patch antennas

The simulated three dimensional ADS radiation pattern data for the U-shaped microstrip patch antenna was imported into MATLAB through a series of text files and was manipulated into a matrix of data so that it could be used with the *phased.CustomAntennaElement* function from the Phased Array toolbox. This was an important step as the patterns for the constructed antenna were used for the simulations conducted in Chapter 3. Furthermore, having the ADS radiation pattern data in MATLAB allowed for a direct verification and comparison of the simulated radiation pattern from ADS with measurements taken from the anechoic chamber.

The second test placed the ULA into the anechoic chamber at one end while a horn antenna radiated the ULA from the other end to measure the antenna pattern. Only one of the microstrip patch antennas of the ULA was connected to measurement equipment while the other 7 elements were terminated with 50 Ω matching loads. The ULA was mounted on a turret which rotated so that full E and H plane measurements could be taken. Prior to measuring the microstrip patch antenna, a calibration was conducted with a Model 3160 horn antenna at a frequency of 8.8 GHz. At 8.8 GHz, the horn antenna should have a gain of approximately 15 dB [48]. An uncalibrated power level of $S_{21} = -23$ dB was measured on the network analyzer, therefore a calibration factor of 38 dB was added to all S_{21}measurements for the microstrip patch antenna. Figure 4.16 depicts the Model 3160 horn antenna on the motorized platform during calibration.

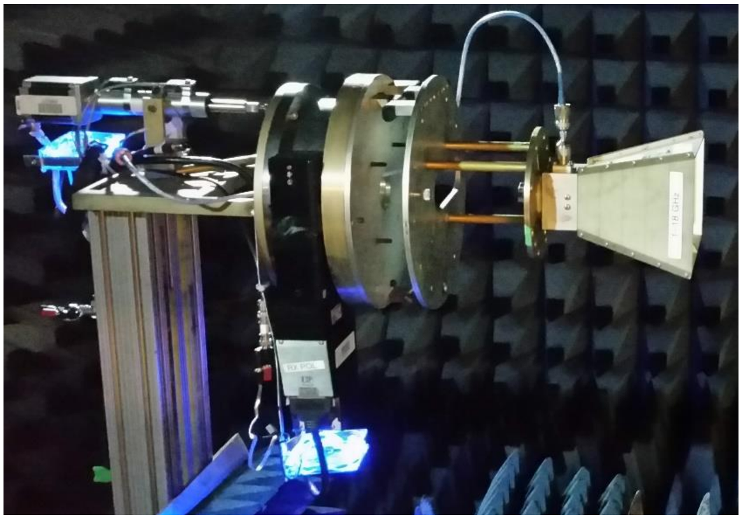

Figure 4.16 3160 Series Horn antenna used for calibration on the turret assembly

The 3160 horn was replaced by the ULA and measurements were taken by rotating the turret in 2° increments. The anechoic chamber at RMC uses a MATLAB function to control the turret and to record the data. The measurement test was conducted at 8.8 GHz and the data was saved in a MATLAB workspace for comparison. Figures 4.17 and 4.18 compare the E and H plane measurements from the chamber with the simulated ADS data of a single antenna. While the measured E plane of the antenna differs dramatically from the ADS simulation, it was determined that the antenna was still useable as experimental measurements would primarily be conducted on the H plane using an azimuth radar scan. The significant difference in the antenna pattern and gain could be attributed to the manufacturing accuracy of the machine, the mutual coupling between the closely spaced elements not accounted for in simulation, or from the absorber pad that was placed behind the ULA during measurements. Further antenna testing and analysis would be required to determine conclusively the source of the differences. As the main requirement of producing a broadband microstrip patch antenna was met, further antenna testing was not completed as the antenna met the minimum requirements of achieving less than a 1 m range resolution for a stepped-frequency continuous wave waveform MIMO radar.

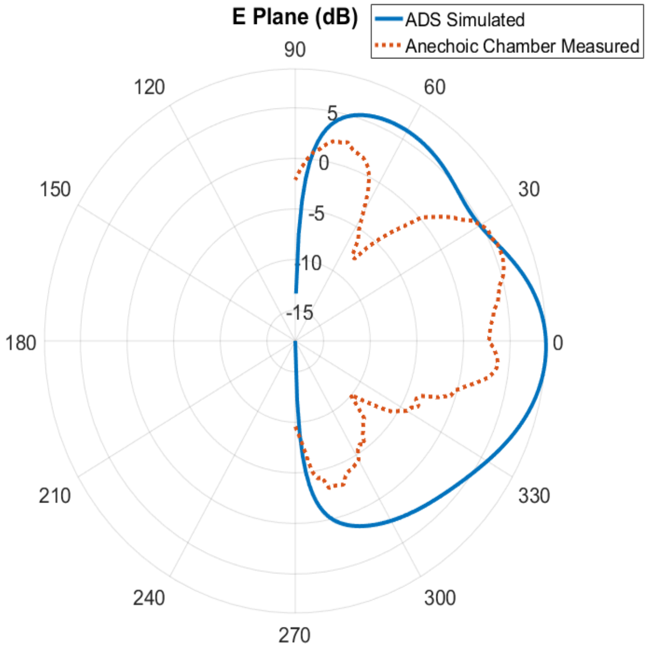

Figure 4.17 E-Plane simulated and measured antenna pattern comparison

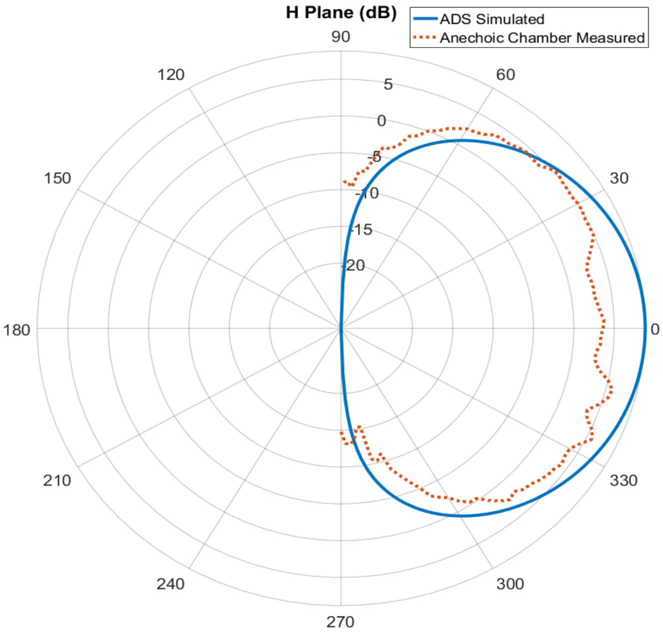

Figure 4.18 H-plane simulated and measured antenna pattern comparison

4.4 PNA-X MIMO Radar Implementation

Keysight's N5244A 4-port PNA-X network analyzer [49] is capable of transmitting and receiving stepped-frequency continuous wave signals from 10 MHz to 43.5 GHz with a dynamic range of 124 dB and an output power of 13 dBm. Using the N4692A electronic calibration kit [50] with the N5244A provides coherent phase measurements within $\pm 0.34^{o}$ and ±0.06 dBm in magnitude for operating frequencies under 10 GHz.

When implementing a MIMO radar with the PNA-X, unlike a SDR, the waveforms are restricted to TDM stepped-frequency continuous wave. However, the PNA-X provides a reliable self-contained phase coherent RF front-end across four RF channels, which is a critical requirement that could not be achieved with the USRP X310 and CBX-120 daughterboards. Figure 4.19 is a high-level schematic of the RF components contained within the N5244A PNA-X. The configuration used for the MIMO radar does not deviate from Figure 4.19 in that all jumper connections remained in place and S-parameter measurements were used to collect radar data. The S-parameters are defined by the ratios of A, B, C, and D with R1, R2, R3, and R4. For instance, S_{11} is defined as A/R1 whereas S_{23} is defined as B/R3. R1 to R4 are reference receivers that measure the signals as they leave the analyzer and receivers A to D measure the radar return signals.

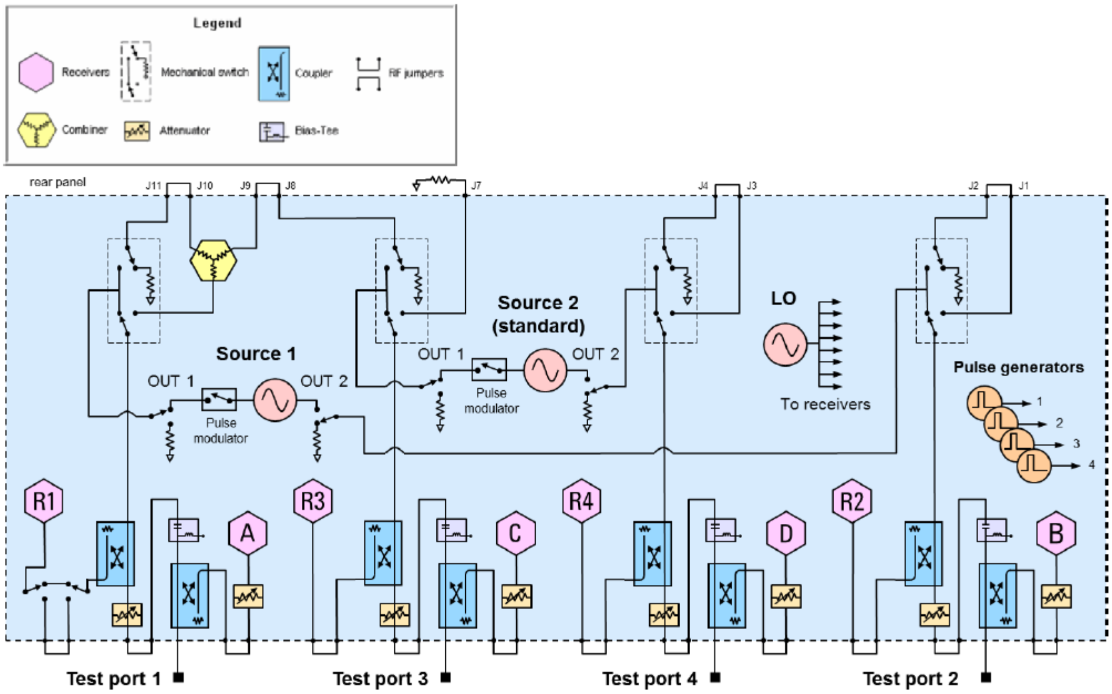

Figure 4.19 4-port N5244A PNA-X network analyzer schematic [41]

When transmitting on each of its four ports, the PNA-X cycles between them using TDM based on the frequency bandwidth, number of frequency data points, and the IF bandwidth of the system. In other words, TDM is inherent to the PNA-X so orthogonality is achieved for the transmitting waveforms. Therefore, the PNA-X can be used to create a MIMO radar if the received S-parameters can be mapped to virtual elements in a similar fashion to the simulated MIMO radar described in Section 3.4. Using the specifications of the microstrip patch ULA from the previous antenna section, a Simulink model was developed to manipulate the S-parameter data from the PNA-X to extract the relevant phase and amplitude information and associate it to an element in a virtual array. Figure 4.20 represents a high-level signal flow diagram for the PNA-X MIMO radar that will be explained in detail over the next several paragraphs.

The PNA-X connects its four test ports to the four center elements of the microstrip patch ULA using 3-foot cables. The four elements of the ULA not being used are terminated with 50 Ω matching loads. The PNA-X and the ULA are

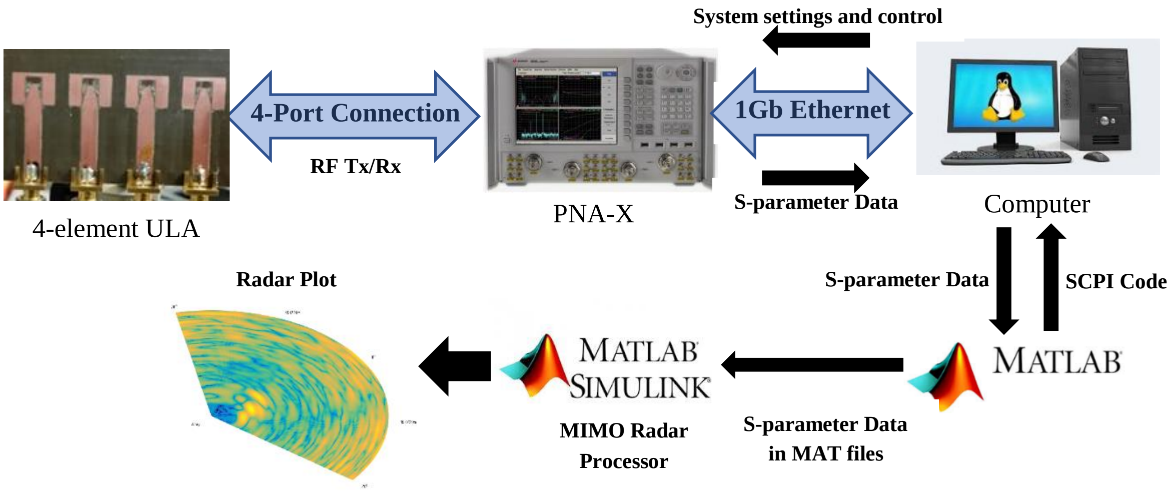

Figure 4.20 System Overview of PNA-X MIMO radar

mounted on a moveable cart for easy transportation. Figure 4.21 is a photograph depicting the test setup. The PNA-X is connected to a Linux computer running MATLAB 2016b through a 1 GB Ethernet cable to form an IP network. The PNA-X is controlled locally from its front panel or remotely from the computer through several MATLAB functions using Standards Commands for Programmable Instruments (SCPI) code [51]. The SCPI MATLAB function adjusts the settings on the PNA-X such as frequency, IF bandwidth, power settings, number of samples, etc. The function will also set which S-parameters to extract and the number of times to extract S-parameter data from the PNA-X. The SCPI MATLAB function will save the S-parameter data, which can be viewed as I and Q data, in a MAT file format so that the data can be used as radar returns with a Simulink model. Prior to running the SCPI MATLAB function, an electronic calibration using the N4692A is either recalled from memory or conducted at the end of the four cables to balance the four channels. Unlike the data rate issues experienced with the SDR, no underruns or overruns are experienced when S-parameter data is sent to the Linux computer.

The S-parameters are saved as a three-dimensional matrix MAT file in MATLAB. The first dimension is defined by the number of frequency steps taken over a total specified bandwidth. The total bandwidth will define the range resolution of the radar and was set to 450 MHz to respect the operational bandwidth of the microstrip ULA for all experiments. Using (2.8), this corresponds to a range resolution of 33 cm. The number of frequency points taken varied for each experiment and will define the maximum unambiguous range defined by (2.9). The

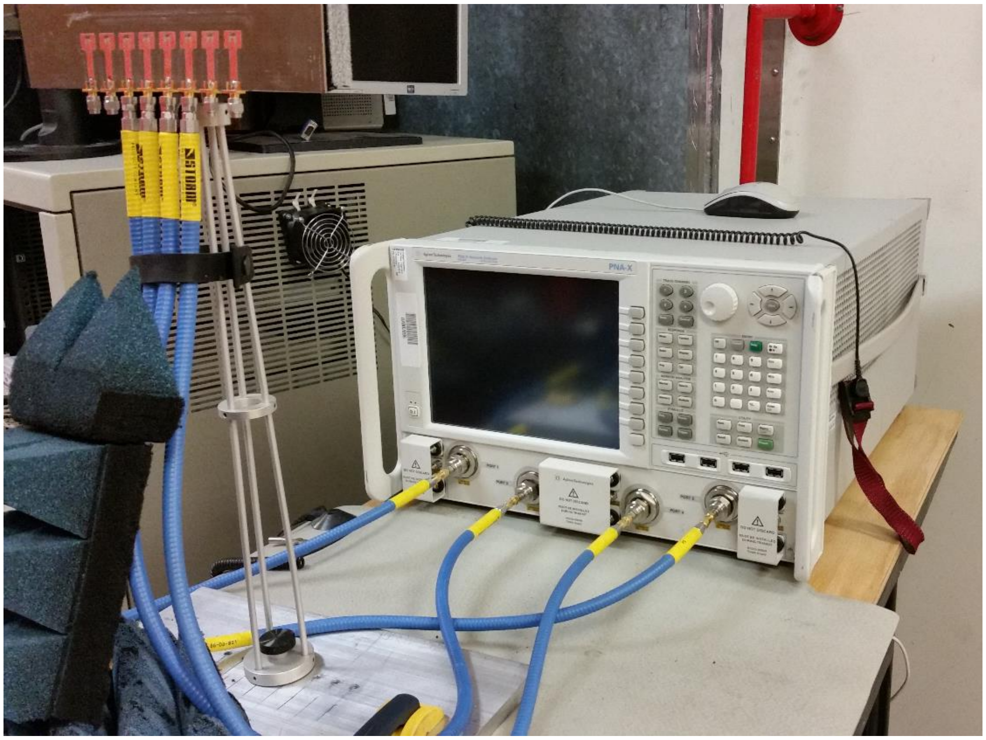

Figure 4.21 PNA-X setup and mounting arrangement

second dimension of the matrix is defined by the number of S-parameters that are extracted. If all 16 S-parameters are extracted, which is the default setting, then the matrix dimension will be 33 which corresponds to the received amplitude and phase for each S-parameter as well as a column for the current operating frequency. The last dimension of the matrix is defined by the number of sweeps extracted, or more specifically how many times the PNA-X will sweep through the specified S-parameters. A single sweep represents the time it takes for the PNA-X to sweep across all of the S-parameters specified in the second dimension. To summarize, the MAT files are saved in a matrix formatted as shown in Figure 4.22.

Given the format of the received data, a Simulink model was built to manipulate the S-parameters into a virtual array and to perform IFFT processing so that range and angle information from targets could be extracted. The high-level Simulink model used to process the radar returns is shown in Figure 4.23. Two measurements are always required when using the PNA-X as a MIMO radar: one with targets and another of the background. The background measurement acts similar to a clutter map in that it measures the environment, but instead of it being

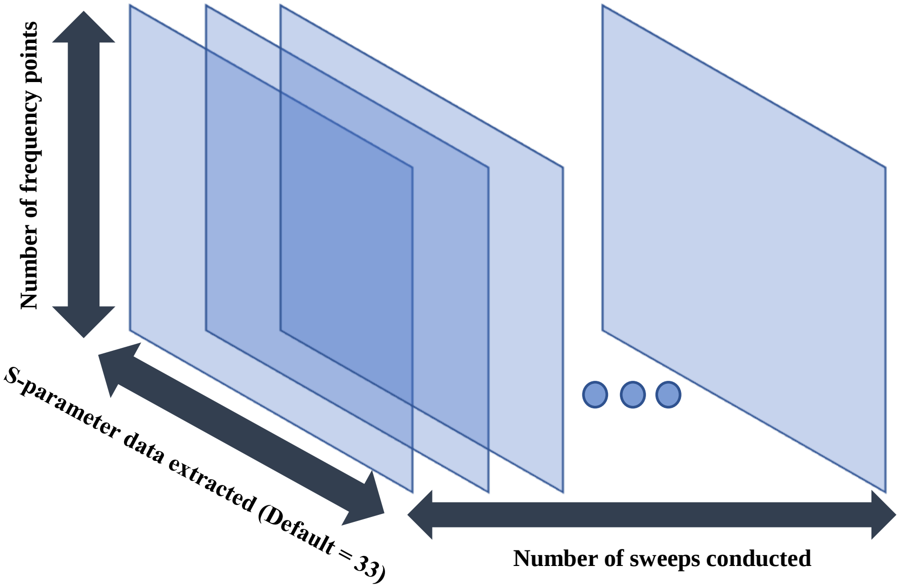

Figure 4.22 PNA-X S-parameter MAT file matrix

used to establish a threshold for a detector, it is subtracted against the radar returns with the targets of interest. This step is necessary to account for the reflections from the antennas shown in Figure 4.15 so the receive channels from S_{11}, S_{22}, S_{33}, and S_{44} can be used as part of the virtual array. If this background measurement is not conducted, another calibration method would be required to account for antenna reflections.

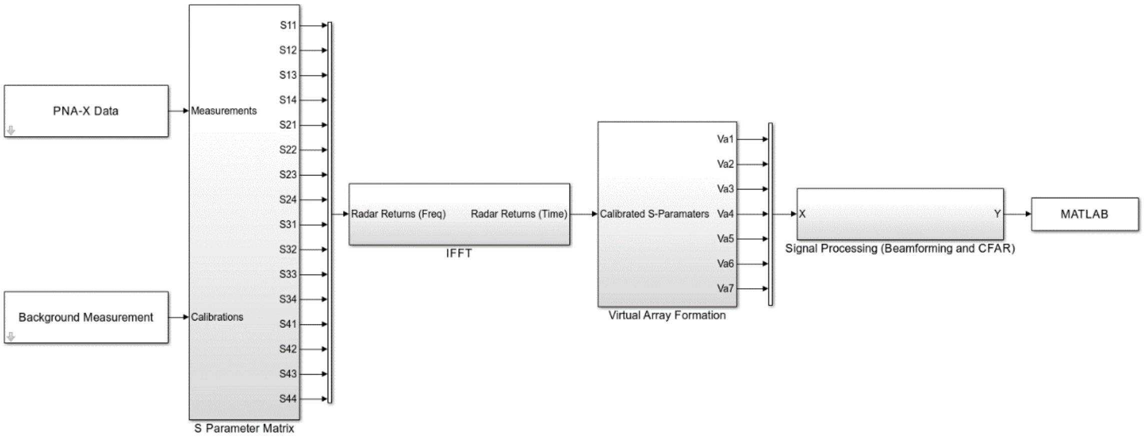

Figure 4.23 Simulink overview of the PNA-X MIMO radar

The matrices of the PNA-X Data and Background Measurement from Figure 4.23 are measured with the same settings to ensure that they have the same matrix dimensions. These two matrices are the input to the Simulink model which processes the data one sweep at a time, or more specifically, one rectangle of information from Figure 4.22 at a time. The data from both matrices are sent to the S-parameters block which subtracts the background measurement against the data with targets and converts the received data from amplitude and phase to values of I and Q. The I and Q data are then sent to an IFFT block where the received data is converted from the frequency domain to the time domain. An IFFT is conducted on each S-parameter and then buffered over a specified coherent integration interval. As the data from the PNA-X is stored based on equal steps of frequency, the IFFT input is merely one column of data from the S-parameter matrix. Figure 4.24 illustrates how the I and Q data is extracted for the IFFT and then integrated. The number of frequency points taken over the sweep bandwidth will define the maximum range of the radar whereas the number of points taken in the IFFT will define the sample rate of the data in the time domain. Windowing options such as Hamming are implemented as part of the IFFT block, but were generally not used because they decrease the range resolution of the radar.

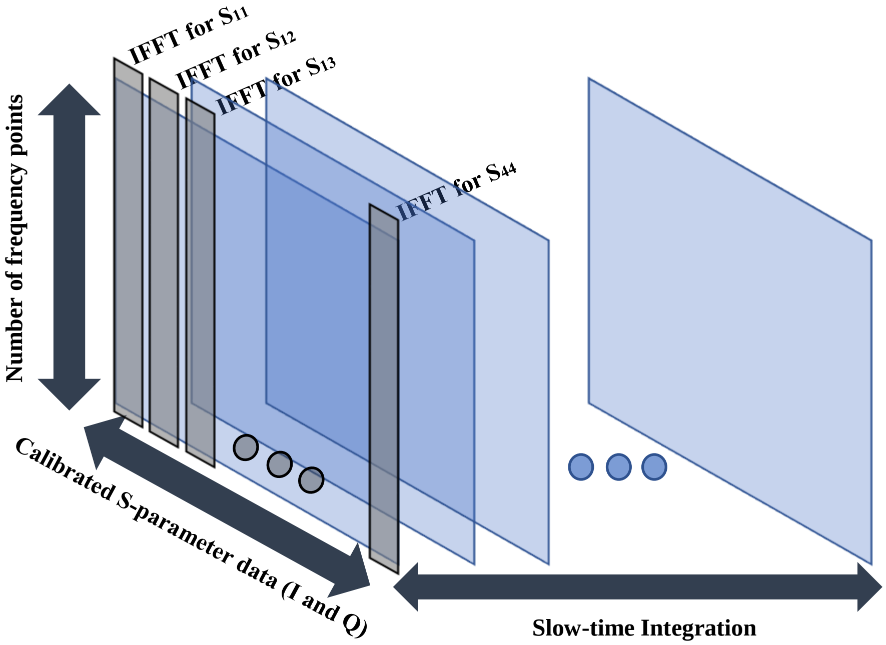

Figure 4.24 Manipulation of S-parameters to perform an IFFT and coherent integration

After the S-parameter radar returns are converted to the time domain, the data is sent to the virtual array block for coherent integration and to create a virtual array. The virtual array block maps S-parameter data to specific virtual elements in a similar fashion to what was described in the MIMO radar simulation of Section 3.3.2. As TDM waveforms and a ULA are being used once again, the virtual elements will have overlapping weights when implementing (2.9). Using a ULA with half wavelength antenna spacing, the virtual elements will be defined in accordance with Table 4.1 and the resultant theoretical two-way array pattern for the PNA-X radar is shown in Figure 4.25.

Table 4.1 Virtual Array logic for S-parameters of PNA-X MIMO radar

Transmitting Element	**S-Parameters**							**Rx Elements**
Test Port 1	S11	S21	S31	S41				**Rx 1**
Test Port 2		S12	S22	S32	S42			**Rx 2**
Test Port 3			S13	S23	S33	S43		**Rx 3**
Test Port 4				S14	S24	S34	S44	**Rx 4**
Virtual Array Weights	**1**	**2**	**3**	**4**	**3**	**2**	**1**	

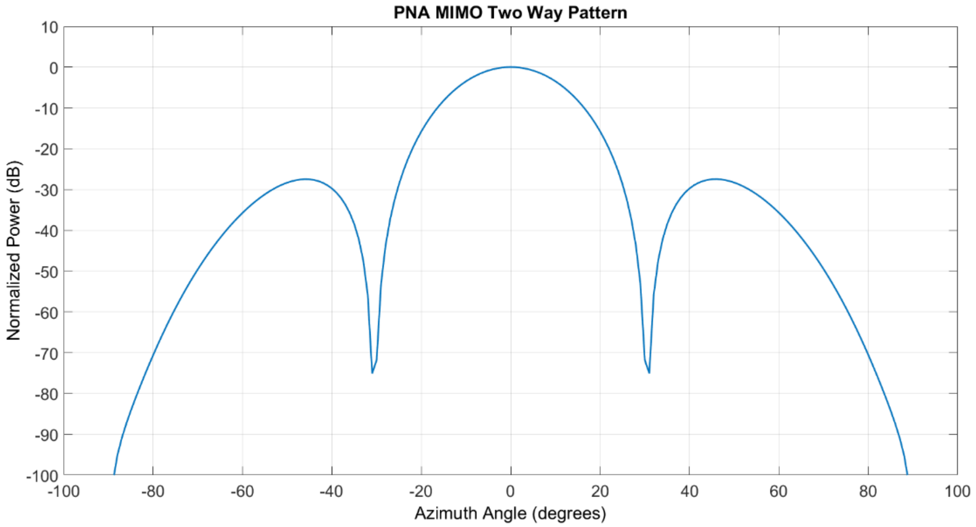

Figure 4.25 Theoretical PNA-X MIMO radar two-way array pattern

The theoretical –4 dB beamwidth of the PNA-X MIMO radar with virtual element weighting of [1 2 3 4 3 2 1] is approximately 22°. Furthermore, the sidelobes are almost –30 dB down from the main beam, making this a useable antenna pattern in a laboratory environment to detect targets at different azimuths. Other processing techniques similar to those used in the MIMO radar simulation are conducted within the signal processing block such as STC and CFAR cell-averaging threshold detection. The processed radar returns along with the CFAR threshold from the Simulink model are saved as workspaces in MATLAB for plotting and analysis.

4.5 Experimental Results

4.5.1 PNA-X Signal Processing Demonstration

Before discussing in-depth experimental results in the next several sub-sections, it is important to highlight how some of the processing techniques of the PNA-X MIMO will impact the radar return. One of the advantages of using Simulink is that an end-user can place a scope or spectrum analyser block anywhere within the Simulink model. As the data from the PNA-X is saved as a MAT file within MATLAB and processed in Simulink afterwards, the radar data can be recalled and analyzed at any time without being connected to the PNA-X. This provides flexibility and allows analysis of the radar returns from various perspectives by applying different processing techniques without having to retake measurements.

To demonstrate specific processing techniques and the radar picture, a single 8 inch diameter aluminum sphere was placed 3.8 m away from the ULA within RMC's anechoic chamber. The PNA-X was set to a center operating frequency of 8.78 GHz with a total sweep bandwidth of 450 MHz, providing a 33 cm range resolution. The IF bandwidth of the PNA-X was set at 100 kHz while a total of 64 frequency samples were taken across the 450 MHz frequency band providing an unambiguous range of just over 21 m. The PNA-X and ULA setups in the anechoic chamber are depicted in Figure 4.26 and the target can be viewed in Figure 4.27.

Figure 4.28 demonstrates the magnitude of S_{23} after an IFFT, which represents a single transmit/receive path for the radar without additional processing to improve the SNR. As it can be observed, there is no distinguishable target at 3.8 m. However, as Figure 4.29 demonstrates, after 10 coherent integrations, the 8 inch sphere is easily detected over the noise floor. The radar returns near the radar are higher than desirable in Figure 4.29 so STC is used to attenuate nearby returns. Figure 4.30 demonstrates the use of STC. Lastly, Figure 4.31 depicts the radar plot for the entire environment using 10 coherent integrations and Figure 4.32 shows the three-dimensional radar return plotted against the threshold detector of the cell-averaging CFAR detector. As it can be observed in Figure 4.32, the 8 inch sphere is detected and exceeds the CFAR threshold.

Figure 4.26 PNA-X and ULA setup in RMC’s anechoic chamber

Figure 4.27 Metallic 8 inch sphere target located 3.8 m away from the ULA

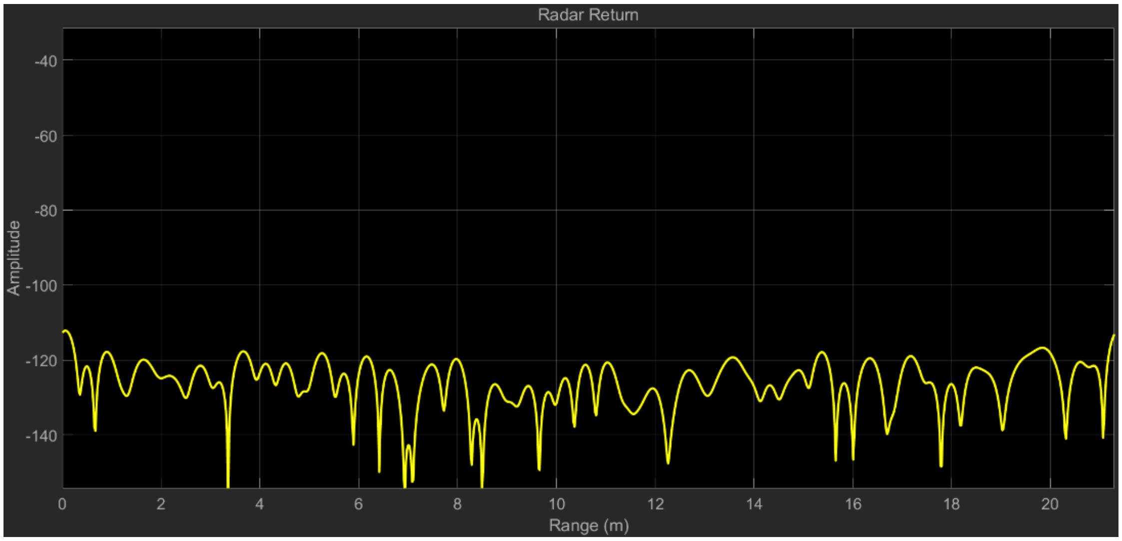

Figure 4.28 Return of S_{23} after an IFFT of a sphere located at 3.8 m

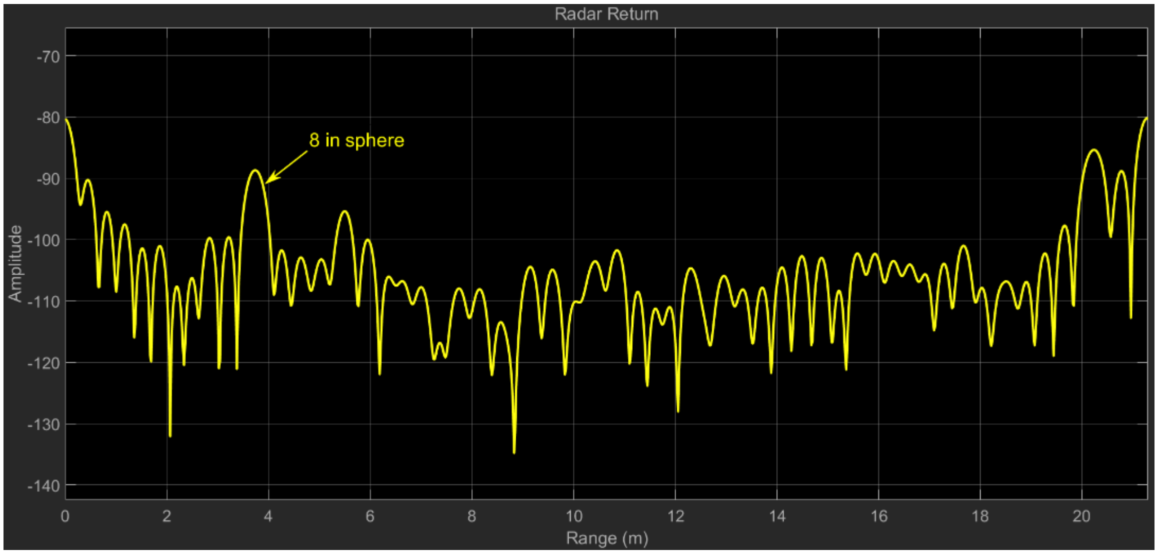

Figure 4.29 Radar return of the first virtual element after 10 coherent integrations

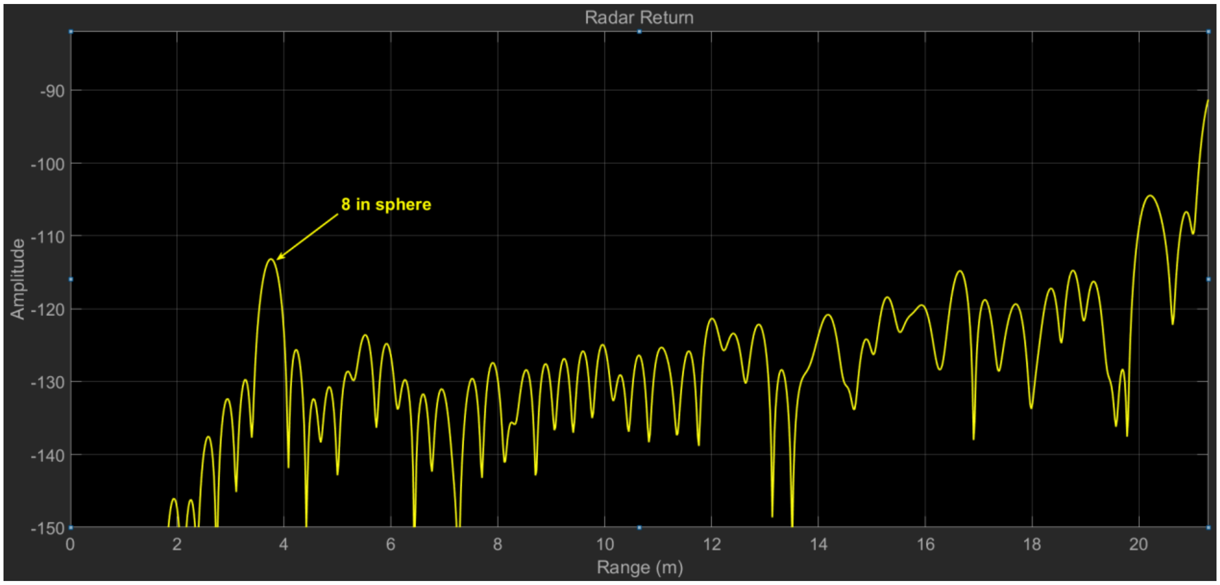

Figure 4.30 A processed radar return with STC

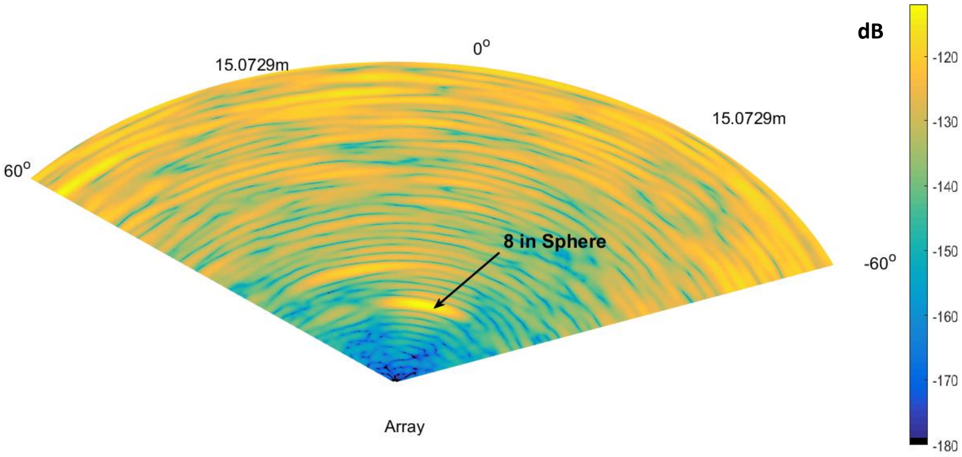

Figure 4.31 PNA-X MIMO radar plot with a single target

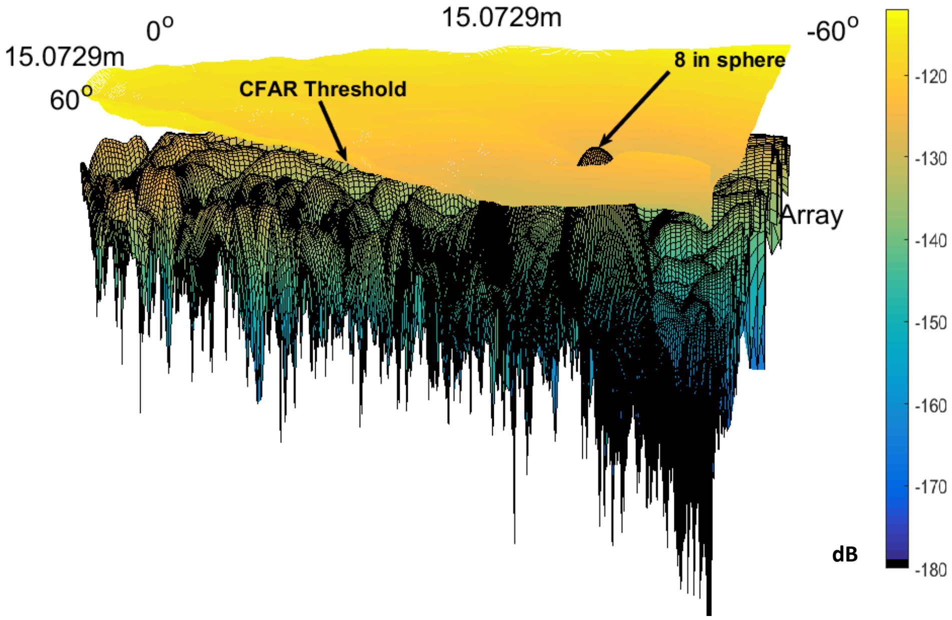

Figure 4.32 Three-dimensional PNA-X MIMO radar plot with a threshold detector

4.5.2 Single Target Beam Pattern Validation

One significant advantage of a MIMO radar over that of a phased array radar is that it can adjust the number of RF channels to process, effectively changing its beam pattern. While using all channels provides greater diversity, the MIMO radar is not limited to only one beam pattern. The MIMO radar can store a set of radar returns in its memory where the data can be manipulated to create different beam patterns. Furthermore, it allows for a combination of beamforming techniques, which could be useful in a low SNR scenario or hostile EM environments when jammers are present. For instance, a phase-shift beamformer can be used in parallel with MUSIC, ESPRIT or MVDR beamforming techniques. The limiting factor in performing these beamforming techniques in parallel is processing capability. If the assumption is made that there are sufficient signal processing computers then these techniques could be calculated at the same time and compared against each other for confidence checks. There are many possibilities to explore and an analysis of beamforming techniques is beyond the scope of this thesis. Having said that, this sub-section will demonstrate how the PNA-X can change its two-way beam pattern with the same set of data without having to take additional measurements.

To demonstrate different MIMO beam patterns with a phase-shift beamformer, the spatial convolution of the antenna elements that form the virtual array must change. Specifically, certain transmit/receive channels must be ignored to change the theoretical pattern shown in Figure 4.25. This can be done by either not transmitting or receiving on antenna elements, or simply ignoring specific S-parameter data when conducting beamforming. A aluminum 3 inch diameter sphere was placed in the anechoic chamber at a range of 3.6 m and –6º in azimuth. Once again, the PNA-X was set to a center operating frequency of 8.78 GHz with a total sweep bandwidth of 450 MHz, providing a 33 cm range resolution. The IF bandwidth of the PNA-X was set at 100 kHz while a total of 64 frequency samples were taken across the 450 MHz frequency band providing an unambiguous range of just over 21 m. A total of 10 integrations was performed on the radar returns.

The first experiment used all transmit and receive channels resulting in a seven-element virtual array with weighting: [1 2 3 4 3 2 1]. The results are shown in Figure 4.33 where it can be observed that the experimental data closely resembles the theoretical beam pattern. The second experiment used the same radar data from the first experiment, but ignored all data from the middle two transmitting elements. This effectively created a spatial convolution to form the virtual array of [1 0 0 1] on transmission with [1 1 1 1] on reception. The resultant virtual array weighting used by the phase-shift beamformer is [1 1 1 2 1 1 1]. Figure 4.34 illustrates the results of the second experiment where once again it can be observed that the experimental results closely align with the theoretical two-way pattern.

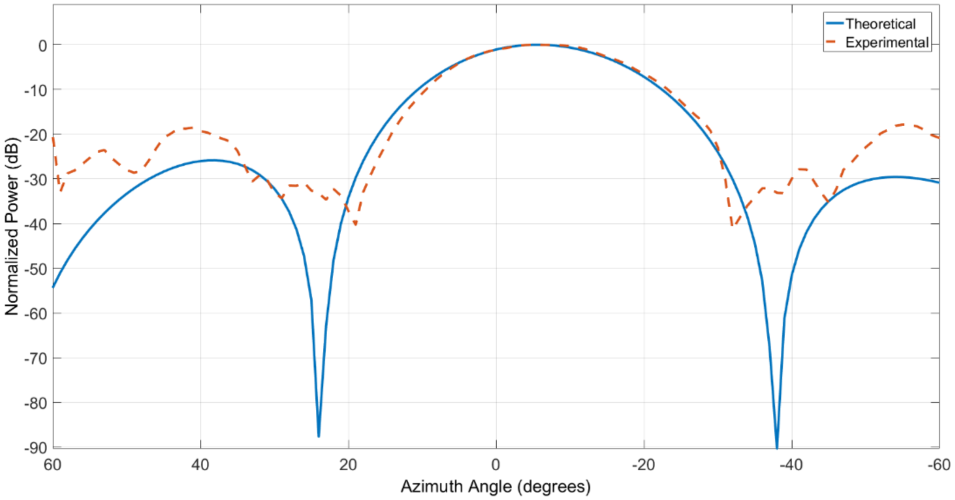

Figure 4.33 PNA-X beam pattern verification for a virtual array: [1 2 3 4 3 2 1]

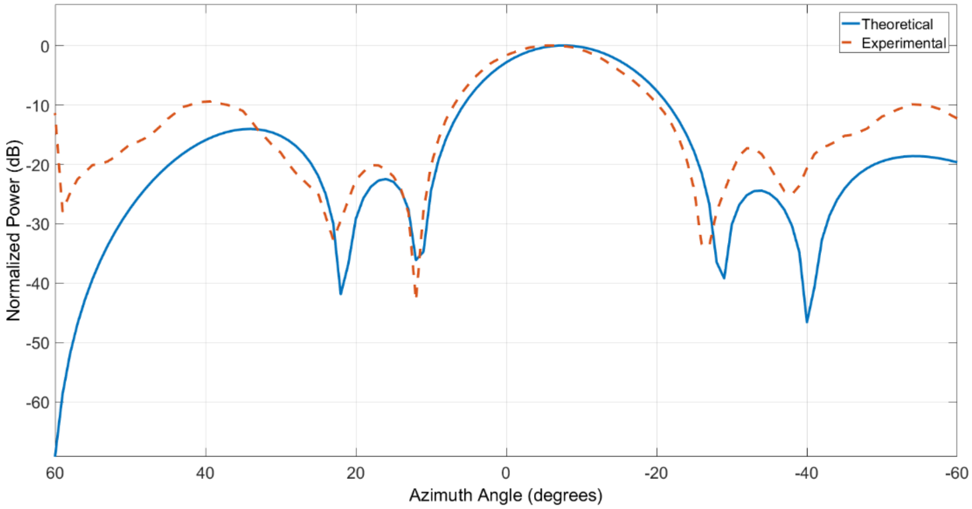

Figure 4.34 PNA-X beam pattern verification for a virtual array: [1 1 1 2 1 1 1]

The results from the last two examples show that a MIMO radar has options to perform beamforming on reception and that it is not restricted to a defined pattern for a sampling period. This introduces a set of advantageous that cannot be implemented in a phased array which performs beamforming on transmission. For instance, the pattern in Figure 4.33 has lower sidelobes, but a wider beamwidth than the pattern in Figure 4.34. The beamforming techniques of MIMO are only limited to the signal processing capacity of the radar platform.

4.5.3 Range Resolution

The next two sub-sections will demonstrate the resolution of the PNA-X MIMO radar system in range and angle and prove that it can distinguish between two closely spaced targets. Experimental results will be compared with theoretical returns for a stepped-frequency continuous wave waveform. No papers or references could be found where an experimental MIMO radar platform was used to demonstrate and verify the radar's resolution capabilities against theory.

Section 2.2.2 highlighted some of the important features of stepped-frequency continuous wave waveforms, specifically (2.7), which defines the range resolution of the radar. As the aim of the experiment is to confirm the range resolution of the radar, two identical targets were used to ensure the same values of RCS to not introduce another variable. The targets used were two cylindrical metallic objects with the equivalent dimensions of a standard 355 ml soda can. The cylinders were mounted on two foam mounts at slightly different elevations so that there was a direct LOS path to both targets from the ULA.

The settings for the MIMO radar remained unchanged from the previous experiment so the theoretical range resolution is 33 cm. Two experiments were conducted with the targets spaced 34 cm and 40 cm apart. The first target was placed at a range of 3.9 m from the ULA at -4° in azimuth and was used as the reference. The second target was placed the appropriate distance behind the first target and approximately 20 cm higher in elevation. The experimental radar returns were compared to theoretical values using [16]:

$$Signal(n) = A_{1n}\, e^{-\frac{i(2\pi(2R_1)}{\lambda_n}} + A_{2n}\, e^{-\frac{i(2\pi(2R_2)}{\lambda_n}} \qquad (4.1)$$

where $n = 1$ to N where $N = 64$, the total number of frequency steps used in the experiment. *Signal*(*n*) is the total theoretical radar return of the two targets for the n^{th} frequency. A_{1n} and A_{2n} are the amplitudes of the return signals where they were both set to one for plotting purposes. R_1 and R_2 are the ranges to the two targets where $R_1 = 3.9$ m. The ranges are multiplied by two to account for two-way travel distance. λ_n is the wavelength for the n^{th} operating frequency. The 64 returns from *Signal*(*n*) undergo an IFFT, which is used as the theoretical reference for comparison against the experimental data.

The first experiment conducted had the targets separated by 40 cm. Figure 4.35 compares the normalized experimental output of the MIMO radar system with the normalized expected theoretical return. As it can be observed, the experimental data closely aligns with theoretical values. More importantly, there is a –4 dB null between the two radar targets meaning that they are distinguishable from one another. One unexpected result was that the target further away had a 2 dB higher return than the closer target. Referring to Figure 4.17, this is likely due to the second target being at a higher elevation as the E-plane element pattern of the microstrip patch antenna has a larger gain at higher elevations. The resultant two-dimensional and three-dimensional radar plots of this experiment are illustrated in Figures 4.36 and 4.37, respectively. Although the target returns blend together, there is still enough of a distinction between them for a trained radar operator to distinguish them as two targets.

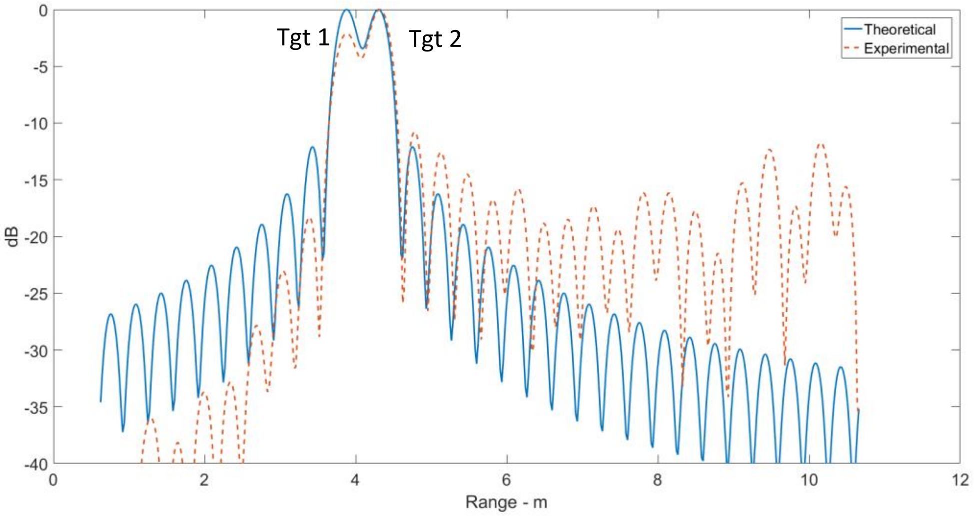

Figure 4.35 Range resolution verification, target separation 40 cm

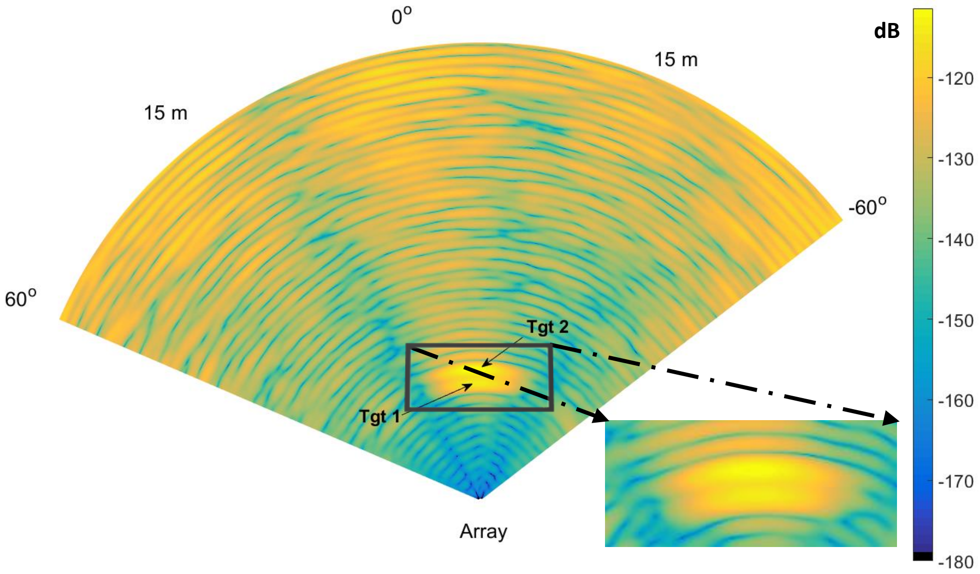

Figure 4.36 PNA-X MIMO radar plot with two targets separated by 40 cm

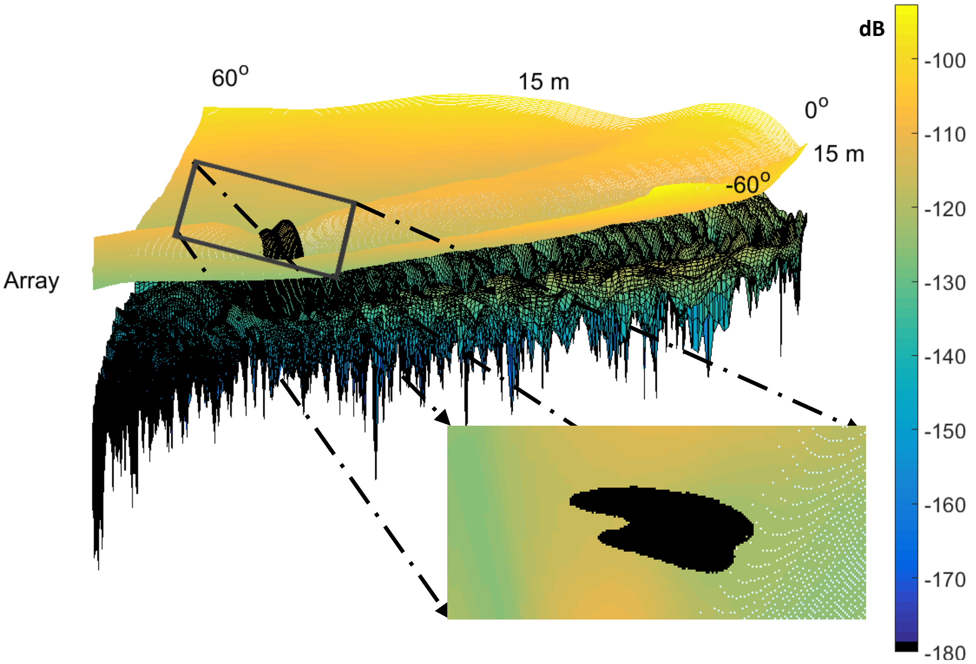

Figure 4.37 Three-dimensional PNA-X MIMO radar plot with two targets separated by 40 cm

The second experiment narrowed the separation between the two targets to approximately 34 cm. The expectation with the targets being so close to the range resolution of the radar was that they would be very difficult to distinguish from one another. The comparison between the experimental and theoretical results is illustrated in Figure 4.38 where, once again, the experimental results align with the expected theory. There is less than a 1 dB null between the returns of the two targets meaning that a tracking algorithm or a radar operator would likely consider the returns from the two targets as one return instead of two. Once again, the experimental return from the first target has approximately 2 dB less return when compared with the second target, further supporting the likely cause for this increase in gain to be from the element pattern of the microstrip patch antennas. This experiment has shown that a MIMO radar follows theoretical range resolutions and that it is not hindered by its processing to distinguish between two targets.

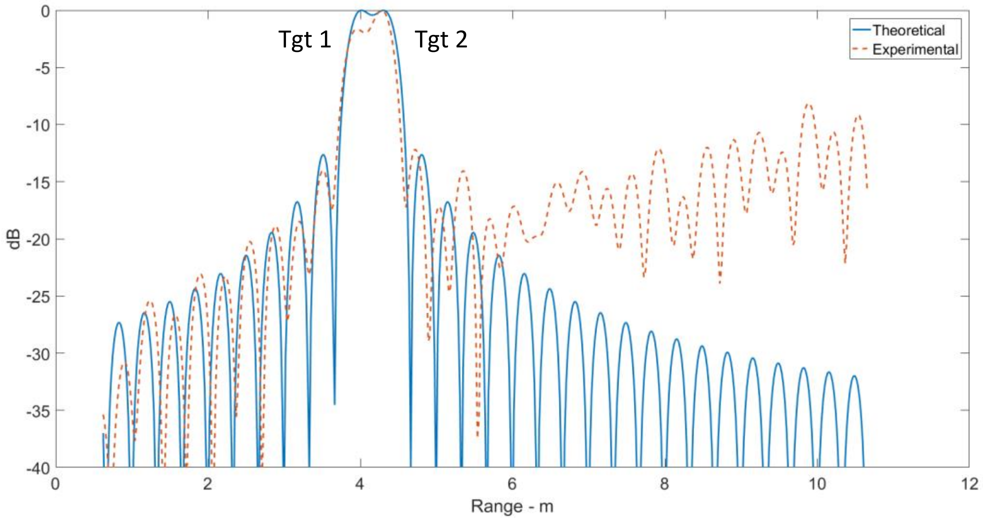

Figure 4.38 PNA-X MIMO radar plot with two targets separated by 34 cm

4.5.4 Angular Resolution

Whereas the range resolution of the radar is defined by the waveform used on transmission, angular resolution is defined by the beamforming technique employed on reception of the MIMO radar. This sub-section will verify the experimental angular resolution of the PNA-X MIMO radar using a phase-shift beamformer and compare it against theory.

The same two cylindrical metallic targets were placed at a range of 4 m and then separated by various distances to demonstrate the angular resolution of the PNA-X MIMO radar. All settings for the PNA-X remained the same as the range resolution tests. The two-way beam pattern of the experiments use all transmit and receive channels and follows the pattern shown in Figure 4.25. Using all channels results in a 4 dB beamwidth at boresight of approximately 22^o. The first experiment separated the targets by 1.2 m, placing them at a relative azimuth of 3^o and –16^o. The experimental angular pattern is compared against the expected theoretical results in Figure 4.39.

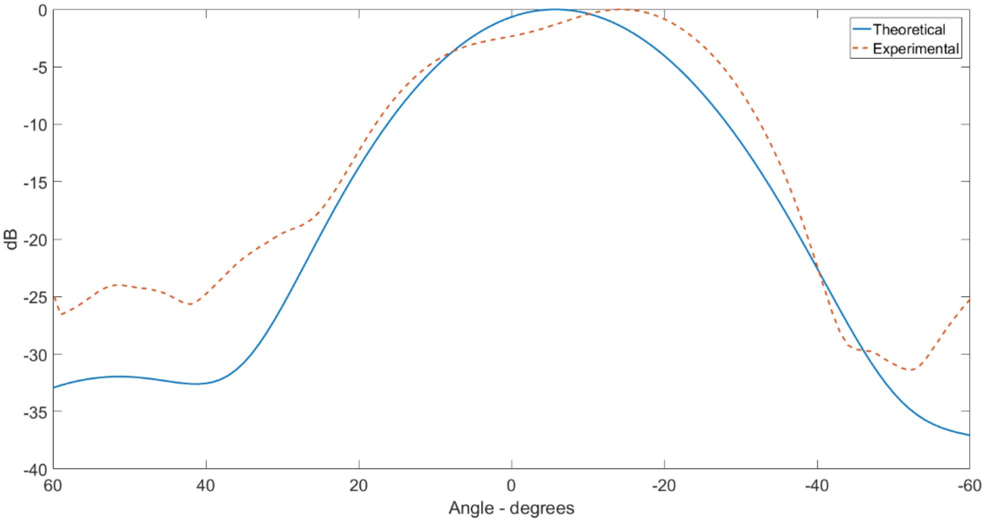

Figure 4.39 Experimental received pattern of two targets at 4 m separated by 19°

As it can be observed in Figure 4.39, the results of the experiment agree with the theoretical received pattern. The two targets are not distinguishable from one another using phase shift beamforming when they are at the same range and only separated by 19° in azimuth. Although not covered in this thesis, it is important to highlight that high-resolution beamforming techniques were able to distinguish the targets and provide an angle of arrival. The ESPRIT DOA, Root MUSIC DOA, and ULA MVDR spectrum blocks from MATLAB's Phased Array toolbox could distinguish between the targets. So, while a pattern that follows a phased array radar is not able to distinguish between two closely spaced targets in azimuth, a MIMO radar has additional processing techniques available that can be used to distinguish between the two targets. Figure 4.40 demonstrates the MVDR spectrum block providing the angle of arrival of the two closely spaced targets.

The second experiment separated the two targets at a range of 4 m by 2.34 m in azimuth resulting in a separation of 36°. The results are shown in Figure 4.41 where the two targets are distinguishable from one another. The results closely align with theory and it is interesting to note the differences in the received signal strength for the two identical targets. Referring to Figure 4.18, the H-plane pattern of the microstrip patch antenna is not uniform, and likely varies slightly for each antenna in the fabricated ULA. Not having the same element pattern at all azimuth angles will lead to differences in transmitted and received signal strengths.

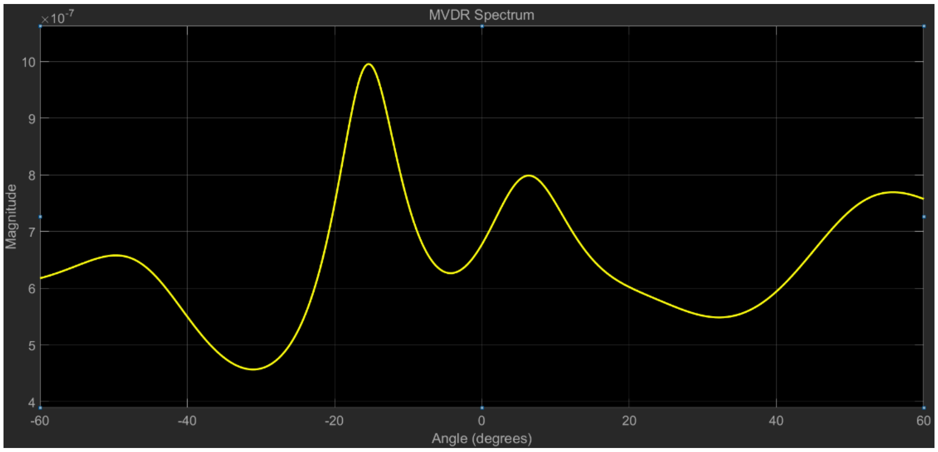

Figure 4.40 MVDR spectrum of two targets at 4 m separated by 19°

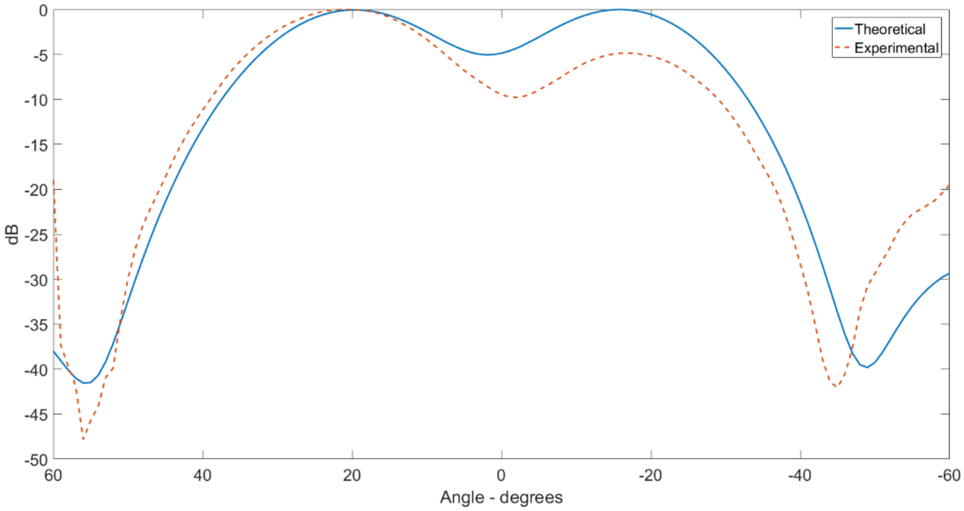

Figure 4.41 Experimental received pattern of two targets at 4 m separated by 36°

4.5.5 Multiple Target Detection

In Chapter 3, it was demonstrated through simulation that a MIMO radar can detect multiple targets within a single CPI without significant loss in SNR or error in angle when compared to the phased array radar simulation. This sub-section aims to verify that the PNA-X MIMO radar can detect and distinguish between three static targets in a controlled environment. The radar settings remain unchanged from previous experiments. Three aluminum spheres with 6 inch, 8 inch, and 10 inch diameters are used as the targets. The targets are arranged in the anechoic chamber as illustrated in Figure 4.42 with the PNA-X MIMO radar out of the picture to the right.

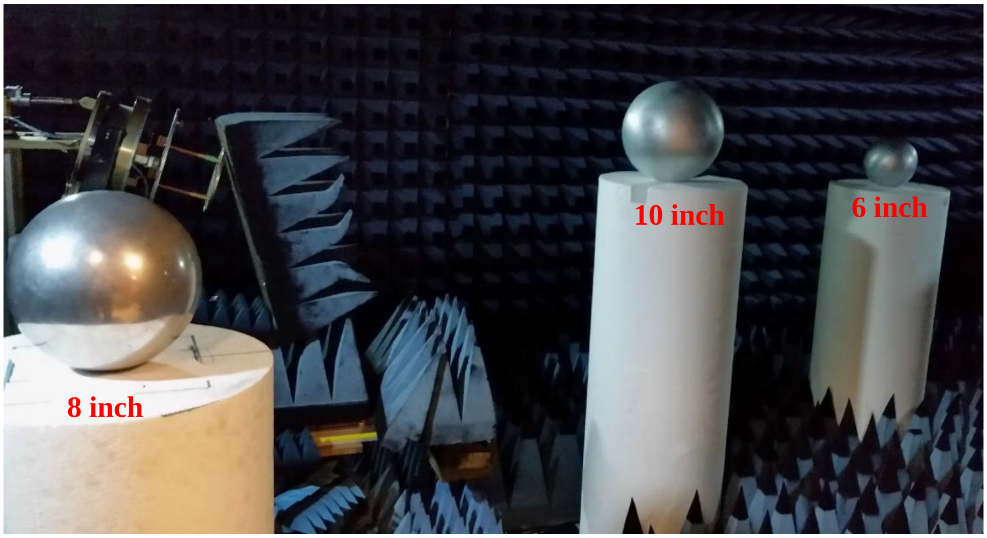

Figure 4.42 Arrangement of three sphere targets in the anechoic chamber

Using a slow-time coherent integration factor of ten, the PNA-X MIMO radar surveys the entire 120^{o} search area and detects the three targets above its cell-averaging CFAR threshold. The resultant three-dimensional radar picture with threshold is shown in Figure 4.43 accompanied with a top-down perspective of the location of the three targets.

The three targets are detected, demonstrating that the experimental MIMO radar system can distinguish multiple targets over a large search area with only a small number of radar returns. While these targets are static and in the controlled environment of an anechoic chamber, this experiment does show the benefit of a MIMO radar being able to detect multiple targets in an area without having to electronically scan. As demonstrated in Chapter 3 in simulation, so long as the MIMO radar platform can handle the increased processing requirements, a MIMO radar will survey an area faster, thus decreasing the time it takes to detect a target, which in turn increases the time for a naval warship to react to a threat.

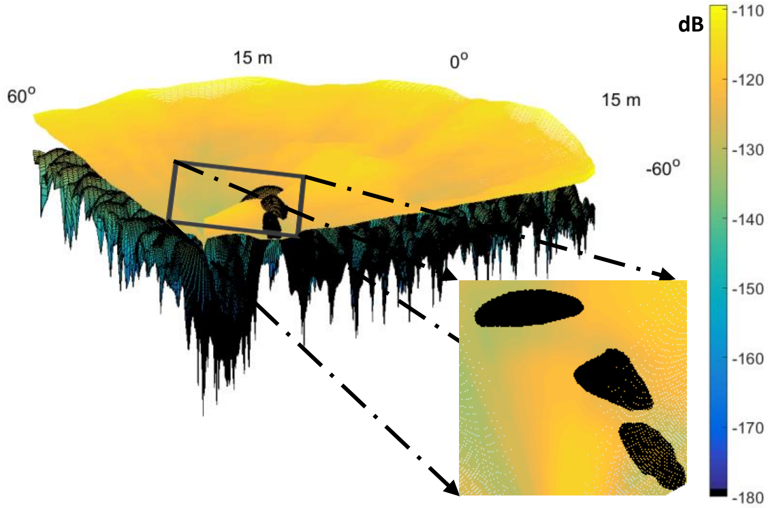

Figure 4.43 PNA-X MIMO radar detection of three targets

4.6 Summary

Although the SDR solution for an experimental MIMO radar offered more flexibility in terms of waveform type, the available equipment at RMC could not support phase coherent operation between two CBX-120 daughterboards within a USRP X310. Furthermore, the connection between thee X310 with a high-end Linux computer could not meet data rate requirements over a 10 Gb Ethernet connection, which in turn limited the bandwidth and range resolution of the radar.

The PNA-X solution offers a self-contained and reliable phase coherent RF front-end. However, unlike a SDR, the transmitting waveform is limited to TDM stepped-frequency continuous wave. It was concluded that the PNA-X can be used reliably to perform experiments as a MIMO radar with MATLAB and Simulink to investigate research questions outside of the study of orthogonal waveforms. Through experimentation, it was demonstrated that a MIMO radar can manipulate radar returns in multiple ways on reception to apply different beamforming techniques after a single CPI. Further empirical results showed the ability of the MIMO radar to distinguish between two closely spaced targets in range and angle and how different beamforming techniques can be used to improve the resolution and detection capabilities of a MIMO radar.

5 Conclusion

5.1 Summary

As discussed in Chapter 2, a MIMO radar performs beamforming on reception using orthogonal waveforms to detect a target's location. Doing so allows a MIMO radar to search an entire area of interest after only a few orthogonal transmissions, but at a cost of additional processing. To maintain the same SNR as that of a phased array radar, a MIMO radar must perform additional coherent integrations over a CPI, which can lead to ambiguities if the target is moving. Traditional radar processing techniques commonly found in phased array radars such as STC and cell-averaging CFAR techniques can be applied to a MIMO radar; however, a MIMO radar can apply STAP techniques directly such as MUSIC or ESPRIT.

Chapter 3 demonstrated that MATLAB and SIMULINK can be used to create a reliable and flexible simulated test environment for radar systems. This chapter described the requirements and design for the simulated phased array and MIMO radar systems while highlighting similarities and differences between them. An overview of the signal processing techniques to improve the SNR was also provided. A comparison and validation of the two radar systems was performed over a series of simulated scenarios.

Chapter 4 described the new PNA-X TDM MIMO radar system and discussed issues that prevented an experimental implementation of a MIMO radar using SDRs. The PNA-X MIMO radar performed measurements in the anechoic chamber to validate its design and compare it against MIMO radar theory. Angular and range resolutions were validated and multiple targets were able to be detected and distinguished from one another.

5.2 Conclusions

After conducting the research of this thesis, it is apparent that there are two critical design considerations for a colocated MIMO radar. The first design consideration being the transmitting orthogonal waveform and its risk of cross-correlation when mapping received orthogonal waveforms to virtual array elements and the second one being the application or type of target that a MIMO radar is trying to detect for a given SNR environment. Other areas of MIMO radar research such as exploring different methods to determine the angle of arrival through various beamforming techniques is useful, but cannot be performed unless the received signals are orthogonal and distinguishable, a virtual array can be formed, and there is enough SNR to detect a target.

Most research papers and documents read over the course of this thesis focused very little on the type of target being detected and more on general MIMO theory or on a new signal processing method. Designing a radar should be defined by requirements, which starts with the type of target the radar is trying to detect. An undetected target's movement and location is unknown to an operational radar; however, a radar should employ settings and be designed with features to maximize the SNR and its potential in detecting that target. Orthogonal waveforms should be selected based on the type of target being detected for a given environment and how a target might impact the orthogonality of the waveform. Maintaining orthogonality between waveforms is critical for creating the virtual array as any cross-correlation between received signals could lead to a signal being mapped to an incorrect virtual element. Once the receive signals are properly mapped to virtual elements of a virtual array, then a MIMO radar can use any number of its countless methods to process the radar returns where it is only limited by the processing capacity of the radar platform.

The target requirement for this thesis was to detect a boat travelling at a maximum radial speed of 15 m/s on the surface of the ocean to a maximum range of the radar horizon. The simulated and experimental radar systems were designed to meet this scenario to support the aim of this thesis in determining that a MIMO radar is superior to a phased array in detecting moving boats on the ocean. TDM was selected as the method to achieve orthogonality to eliminate any possibility of cross-correlation between signals so the research focused primarily on the target and how its interaction affected the two radar systems.

It was demonstrated that a MIMO radar has the same two-way beam pattern as a phased array radar when using the same number of elements in a ULA over a longer CPI. When detecting a moving target, a longer CPI is disadvantageous for a MIMO radar as Doppler will induce errors and inefficiencies in coherent integration. For the scenarios presented, it was shown that a MIMO radar will maintain less than 1.5^{o} error and less than a 4 dB loss in gain so long as the total Doppler phase shift over the CPI is less than π radians. Compensating for a target's Doppler effects remains an active research area for MIMO radar. It was also shown analytically that a MIMO radar should operate at lower frequencies, such as L-band, to minimize the impact of Doppler from targets.

Although a longer CPI for MIMO is a disadvantage, in that time a MIMO radar can search an entire area whereas a phased array is limited to its scan rate to search. Furthermore, it was shown that the MIMO radar's refresh rate of the radar picture is faster than a CPI as it can maintain a history of radar returns in memory and recall them. The refresh rate of a radar picture for a MIMO radar can be as fast as every orthogonal pulse, or in the case of TDM, every M^{th} pulse, where M is the number of transmitting elements.

However, maintaining the radar picture at a faster refresh rate requires additional processing. With both the MIMO and phased array radar system using the same receive signal processing, it was demonstrated for the given scenario that the MIMO radar will require to perform at least 13.3 times more calculations than the phased array radar. If the MIMO radar platform can handle the increased processing requirements, a MIMO radar will survey an area faster, thus decreasing the time it takes to detect a target, which in turn increases the time for a naval warship to react to a threat.

In conclusion, a MIMO radar can search a large area and perform detection faster than a phased array. As a MIMO radar performs beamforming on reception, it has additional processing techniques available to it such as MUSIC or ESPRIT that is not available for a SISO phased array providing it greater flexibility in techniques to use for target detection and localization. For a small search area or for tracking, a phased array radar is superior to a MIMO radar due to its increased transmission gain and lower CPI. Each radar has its own merits and should be used in conjunction with one another to leverage the advantages of both radar systems with the same antenna structure onboard a naval ship. A MIMO radar should be used to search an area and detect targets whereas a phased array radar should be used for target tracking and weapon deployment.

5.3 Contributions

The most important contributions of this work are:

a) The design and implementation of a versatile end-to-end phased array and MIMO radar simulation using Simulink.

b) Scenario-based comparison of a phased array and MIMO radar under simulated conditions.
c) Validation and demonstration of MIMO beamforming.
d) An assessment on Doppler effects created by slow moving targets on a MIMO radar highlighting the importance that the type of target being detected is the most important design consideration for a MIMO radar.
e) The design and implementation of a portable 4x4 TDM MIMO radar system using a PNA-X and MATLAB.
f) Empirical detection and distinction of multiple targets by the PNA-X MIMO radar.

As a result of this work, RMCC now has a functional TDM MIMO radar system that is capable of accurately detecting multiple targets simultaneously with up to four antenna elements. The results of the measurements conducted demonstrate that a MIMO radar is suitable for detecting ocean surface targets.

5.4 Future Work

There are many ongoing research areas for MIMO radar. A modification to the simulations to allow for different forms of orthogonal waveforms should be implemented. This would include adjusting the receiver matched filters and how the virtual array is formed to allow the study of how different waveforms will perform against scenario-based simulation.

The PNA-X experimental platform should be tested against moving targets and other environments other than an anechoic chamber. Furthermore, STAP techniques should be implemented to allow for different beamforming and detection analysis. Measurements with moving targets should be taken and methods to compensate for the Doppler shift induced by the target should also be explored.

Lastly, the SDR option for an experimental MIMO radar warrants further investigation. The flexibility of choosing waveforms for transmission will allow other areas of MIMO to be researched experimentally.

References

[1] J.-M. Colin, “Phased array radars in France: present and future,” in *Phased Array Systems and Technology, 1996., IEEE International Symposium on*, 1996, pp. 458–462.

[2] J. Li and P. Stoica, *MIMO Radar Signal Processing*. Hoboken, NJ: Wiley-IEEE Press, 2008.

[3] P. Sévigny, “MIMO Radar: Literature survey of papers between 2003 and September 2008,” DRDC, Ottawa, ON, TM 2008-333, Mar. 2009.

[4] E. Brookner, “MIMO radars demystified; and their conventional equivalents,” in *2016 IEEE International Symposium on Phased Array Systems and Technology (PAST)*, 2016, pp. 1–10.

[5] P. W. Moo and Z. Ding, “Tracking Performance of MIMO Radar for Accelerating Targets,” *IEEE Trans. Signal Process.*, vol. 61, no. 21, pp. 5205–5216, Nov. 2013.

[6] I. Bekkerman and J. Tabrikian, “Target Detection and Localization Using MIMO Radars and Sonars,” *IEEE Trans. Signal Process.*, vol. 54, no. 10, pp. 3873–3883, Oct. 2006.

[7] H. Sun, F. Brigui, and M. Lesturgie, “Analysis and comparison of MIMO radar waveforms,” in *2014 International Radar Conference*, 2014, pp. 1–6.

[8] N. Levanon and E. Mozeson, *Radar Signals*. John Wiley & Sons, 2004.

[9] M. A. Richards, J. A. Scheer, and W. Holm, *Principles of Modern Radar: Basic Principles*, 1 edition. Raleigh, NC: SciTech Publishing, 2010.

[10] N. C. Currie, *Radar Reflectivity Measurement: Techniques & Applications*. Artech House, 1989.

[11] C. Gentile, “Application of Radar Technology to Deflection Measurement and Dynamic Testing of Bridges,” 2010.

[12] P. W. Moo, T. Laneve, and P. Sévigny, “Experimental validation of coherent multiple-input multiple-output radar antenna patterns,” *IET Radar Sonar Navig.*, Aug. 2015.

[13] K. Luo, “MIMO Radar: Target Localisation,” PHD thesis dissertation, Imperial College London, March 2013.

[14] Y. Qu, G. Liao, S.-Q. Zhu, X.-Y. Liu, and H. Jiang, “Performance analysis of beamforming for MIMO radar,” *Prog. Electromagn. Res.*, vol. 84, pp. 123–134, 2008.

[15] F. Daum and J. Huang, “MIMO Radar Snake Oil or Good Idea?”, Aerospace and Electronic Systems, IEEE Transactions on, pp. 1–12, May 2009.

[16] M. Skolnik, *Radar Handbook, Third Edition*, 3 edition. New York: McGraw-Hill Education, 2008.

[17] P. W. Moo, “MIMO radar Search strategies for High Velocity Targets,” DRDC, Ottawa, ON, TM 2009-288, Mar. 2010.

[18] G. San Antonio, D. R. Fuhrmann, and F. C. Robey, “MIMO Radar Ambiguity Functions,” *IEEE J. Sel. Top. Signal Process.*, vol. 1, no. 1, pp. 167–177, Jun. 2007.

[19] W. Roberts, P. Stoica, J. Li, T. Yardibi, and F. A. Sadjadi, “Iterative Adaptive Approaches to MIMO Radar Imaging,” *IEEE J. Sel. Top. Signal Process.*, vol. 4, no. 1, pp. 5–20, Feb. 2010.

[20] Chun-Yang Chen and P. P. Vaidyanathan, “MIMO Radar Ambiguity Properties and Optimization Using Frequency-Hopping Waveforms,” *IEEE Trans. Signal Process.*, vol. 56, no. 12, pp. 5926–5936, Dec. 2008.

[21] J. Li and P. Stoica, “MIMO Radar with Colocated Antennas,” *IEEE Signal Process. Mag.*, vol. 24, no. 5, pp. 106–114, Sep. 2007.

[22] L. Stankovic, “MIMO Radar: Literature survey of papers published between September 2008 and December 2012,” University of Montenegro prepared for DRDC, Ottawa, ON, CR 2013-018, Feb. 2013.

[23] X. Zhang, L. Xu, L. Xu, and D. Xu, “Direction of Departure (DOD) and Direction of Arrival (DOA) Estimation in MIMO Radar with Reduced-Dimension MUSIC,” *IEEE Commun. Lett.*, vol. 14, no. 12, pp. 1161–1163, Dec. 2010.

[24] A. Hassanien and S. A. Vorobyov, “Transmit Energy Focusing for DOA Estimation in MIMO Radar With Colocated Antennas,” *IEEE Trans. Signal Process.*, vol. 59, no. 6, pp. 2669–2682, Jun. 2011.

[25] X. Zhang and D. Xu, “Angle estimation in MIMO radar using reduced-dimension capon,” *Electron. Lett.*, vol. 46, no. 12, pp. 860–861, Jun. 2010.

[26] S. M. Kay, *Fundamentals of Statistical Signal Processing, Volume II: Detection Theory*, 1 edition. Englewood Cliffs, N.J: Prentice Hall, 1998.

[27] R. Roy and T. Kailath, “ESPRIT-estimation of signal parameters via rotational invariance techniques,” *IEEE Trans. Acoust. Speech Signal Process.*, vol. 37, no. 7, pp. 984–995, Jul. 1989.

[28] T. S. Dhope, “Application of MUSIC, ESPRIT and ROOT MUSIC in DOA Estimation,” *Fac. Electr. Eng. Comput. Univ. Zagreb Croat.*, 2010.

[29] “Products and Services - MATLAB & Simulink.” [Online]. Available: https://www.mathworks.com/products.html?s_tid=gn_ps. [Accessed: 22-Feb-2017].

[30] R. M. O'Donnell, “Radar Systems Engineering Lecture 7 Part 1 Radar Cross Section,” MIT Lincoln Laboratory, 2009. [Online]. Available: http://ece.wpi.edu/radarcourse/. [Accessed: 24-Feb-2017].

[31] C. Wolff, “Radar Basics - Fluctuation Loss.” [Online]. Available: http://www.radartutorial.eu/01.basics/Fluctuation%20Loss.en.html. [Accessed: 24-Feb-2017].

[32] V. Gregers-Hansen and R. Mital, “An Improved Empirical Model for Radar Sea Clutter Reflectivity,” Naval Research Lab, Washington, DC, NRL/MR/5310--12-9346, 2012.

[33] E. and C. C. C. Government of Canada, “Environment and Climate Change Canada - Weather and Meteorology - Met 101: National Marine Weather Guide,” 02-Apr-2014. [Online]. Available: http://ec.gc.ca/meteo-weather/default.asp?lang=En&n=279AC7ED-1. [Accessed: 31-Jan-2017].

[34] T. Kilpatrick and I. D. Longstaff, “MIMO radar - some practical considerations,” in *2015 IEEE Radar Conference (RadarCon)*, 2015, pp. 0566–0571.

[35] M. Akcakaya and A. Nehorai, “MIMO radar detection and adaptive design in compound-Gaussian clutter,” in *2010 IEEE Radar Conference*, 2010, pp. 236–241.

[36] C. Y. Chong, F. Pascal, J. P. Ovarlez, and M. Lesturgie, “MIMO Radar Detection in Non-Gaussian and Heterogeneous Clutter,” *IEEE J. Sel. Top. Signal Process.*, vol. 4, no. 1, pp. 115–126, Feb. 2010.

[37] “Ettus Research - The leader in Software Defined Radio (SDR).” [Online]. Available: https://www.ettus.com/. [Accessed: 05-Mar-2017].

[38] “GNU Radio.” [Online]. Available: http://gnuradio.org/. [Accessed: 05-Mar-2017].

[39] “LabVIEW System Design Software - National Instruments.” [Online]. Available: http://www.ni.com/labview/. [Accessed: 05-Mar-2017].

[40] V.N. Fernandes, “Implementation of a Radar System using MATLAB and the USRP,” MSc thesis dissertation, California State University, May 2012.

[41] M. T. Frankford, “Exploration of MIMO radar techniques with a software-defined radar,” The Ohio State University, 2011.

[42] Y. L. Sit, B. Nuss, S. Basak, M. Orzol, W. Wiesbeck, and T. Zwick, “Real-time 2D+velocity localization measurement of a simultaneous-transmit OFDM MIMO Radar using Software Defined Radios,” in *2016 European Radar Conference (EuRAD)*, 2016, pp. 21–24.

[43] Z. N. Chen and M. Y. W. Chia, *Broadband Planar Antennas: Design and Applications*, 1 edition. Chichester, England ; Hoboken, NJ: Wiley, 2006.

[44] R. Chair, C. L. Mak, K.-F. Lee, K.-M. Luk, and A. A. Kishk, “Miniature Wide-Band Half U-Slot and Half E-Shaped Patch Antennas,” *IEEE Trans. Antennas Propag.*, vol. 53, no. 8, pp. 2645–2652, Aug. 2005.

[45] A. K. Shackelford, K.-F. Lee, and K. M. Luk, “Design of small-size wide-bandwidth microstrip-patch antennas,” *IEEE Antennas Propag. Mag.*, vol. 45, no. 1, pp. 75–83, Feb. 2003.

[46] C. A. Balanis, *Antenna Theory: Analysis and Design*, 3 edition. Wiley-Interscience, 2012.

[47] “Taconic :: TLY | Family of low loss laminates.” [Online]. Available: https://www.4taconic.com/page/tly-87.html. [Accessed: 09-Mar-2017].

[48] "Manuals | ETS-Lindgren." [Online]. Available: http://www.ets-lindgren.com/manual. [Accessed: 10-Mar-2017].

[49] "N5244A PNA-X Microwave Network Analyzer, 43.5 GHz | Keysight (formerly Agilent's Electronic Measurement)." [Online]. Available: http://www.keysight.com/en/pdx-x201767-pn-N5244A/pna-x-microwave-network-analyzer-435-ghz?cc=CA&lc=eng. [Accessed: 12-Mar-2017].

[50] "Microwave Calibration Kits (Maximum Frequency 13.5 to 110 GHz) | Keysight (formerly Agilent's Electronic Measurement)." [Online]. Available: http://www.keysight.com/en/pc-1000002627%3Aepsg%3Apgr/microwave-mechanical-calibration-kits-ecal-modules-up-to-110-ghz?cc=CA&lc=eng. [Accessed: 12-Mar-2017].

[51] "PNA Network Analyzers Help." [Online]. Available: http://na.support.keysight.com/pna/help/latest/help.htm. [Accessed: 12-Mar-2017].